Resonant All-Dielectric Optical Metamaterials

by

Yuanmu Yang

Dissertation

Submitted to the Faculty of the

Graduate School of Vanderbilt University

in partial fulfillment of the requirements

for the degree of

DOCTOR OF PHILOSOPHY

in

Interdisciplinary Materials Science

August, 2015

Nashville, Tennessee

Approved:

Jason G. Valentine, Ph.D.

Richard F. Haglund Jr., Ph.D.

Deyu Li, Ph.D.

To my beloved mom and dad.

Acknowledgements

My journey towards the Ph.D. degree has probably been the most rewarding part of my life, with the help from many people.

First and foremost, I would like to thank my adviser, Prof. Jason Valentine for his unwavering support. Prof. Valentine offered me an opportunity to come to the United States and join his lab fresh from undergrad. Since then, I was extremely fortunate to work with the best, learned through him to be a critical thinker, nurtured by him to grow to be a truly independent researcher. Working in a newly-started lab, I was lucky to have Prof. Valentine guiding me hand by hand running experiments in the beginning days, which developed not only my skill, but also the attitude as an experimentalist. During these years at Vanderbilt, Prof. Valentine has always kept his door open to me for discussion. He is always the best listener, and always offers the most insightful and constructive suggestions for improvement, showing me the "big picture". The sparklings in the discussions eventually became the origins of many of the projects written in this dissertation. Prof. Valentine is also extremely generous and supportive sending me to numerous conferences and introducing me to his colleagues, which helped me interact with the large optics community and built me the connections with future co-workers. His mentorship and support is the single most important reason to my success in the last several years, and he will always stand out as my role model in my future endeavor as a researcher.

I would also like to thank Prof. Sharon Weiss, Prof. Richard Haglund, Prof. Deyu Li and Prof. Yaqiong Xu for serving on my dissertation committee, for providing me

opportunities for research rotations, and for valuable suggestions on my future career options.

I want to especially thank all the Valentine group members, both past and present. Their continuous help, discussion, and friendship have helped make my experience as a graduate student not only productive but also fun. Despite of learning from each other, I truly enjoyed all the happy hours and Bushwackers with these guys. Special thanks to Parikshit Moitra for guiding me on everything ranging from nanofabrication to numerical simulation. Special thanks to Wenyi Wang, who motivates me to go to the lab during nights and weekends, and provides me all the faith and encouragement.

My dissertation research cannot be made possible without the help and support in nanofabrication. Special thanks to Ivan Kravchenko, Daryl Briggs, Scott Retterer, Dale Hensley, Kevin Lester, and Bernadeta Srijianto at CNMS, and Tony Hmelo, Bo Choi, and Ben Schmidt at VINSE. The work in the cleanroom can be struggling, but your training and assistance have made everything much easier.

Many of the friends made my life in Nashville so cheerful. Special thanks to Jialei Song, who has been such an awesome roommate. Special thanks to Jing Wu, Doug Waters and Jackie Waters, who helped me settle down in the first year when I had nothing to embrace.

Special thanks to my undergraduate adviser Prof. Jiaguang Han, who introduced me to the world of "metamaterial" when I barely knew anything about research, and continued to guide me through later days.

Finally, I wish to express my deepest gratitude to my family for their unconditional love, support and encouragement. It feels really good that I know you are

always standing behind my back no matter what happens. To my mom, sending me off to the United States for years is not easy. Thanks for letting me chase what I am passionate about and what is best for my career. To my dad, sometimes I become impatient explaining my research to you, but I wish that in the end, you feel proud seeing your son going so far.

Table of Contents

List of Figures

beam axes are tilted with respect to one another. (i-k) Interference pattern of a vortex beam and a Gaussian beam which have collinear propagation. In (c-k) a linear polarizer is placed in front of the camera to filter out co-polarized light. (l-m) Interference pattern of the vortex beam and the Gaussian beam in the absence of the linear polarizer. 47

List of Abbreviations

CCD	Charge-coupled Device
CNMS	Center for Nanophase Material Sciences
EBL	Electron Beam Lithography
EIT	Electromagnetically Induced Transparency
ENZ	Epsilon Near Zero
FDTD	Finite Difference Time Domain
FEFD	Finite Element Frequency Domain
FOM	Figure of Merit
FTIR	Fourier Transform Infrared Spectroscopy
FWHM	Full Width at Half Maximum
HCG	High Contrast Grating
IFC	Iso-frequency Contour
LPCVD	Low Pressure Chemical Vapor Deposition
MBE	Molecular Beam Epitaxy
MEMS	Microelectromechanical
MOCVD	Metal-Organic Chemical Vapor Deposition
OPA	Optical Parametric Amplifier
OPO	Optical Parametric Oscillator
PCR	Polarization Conversion Rate
PDMS	Poly(dimethylsiloxane)
PMMA	Poly(methyl methacrylate)

PMT	Photo Multiplier Tube
QD	Quantum Dot
Q-factor	Quality Factor
QW	Quantum Well
QWIP	Quantum Well Infrared Photodetector
RIE	Reactive-ion Etch
RIU	Refractive Index Unit
SEM	Scanning Electron Microscopy
SCS	Scattering Cross-Section
SNR	Signal to Noise Ratio
SRR	Split-ring Resonator
TE	Transverse Electric
THG	Third Harmonic Generation
TM	Transverse Magnetic
TPA	Two Photon Absorption
VINSE	Vanderbilt Institute of Nanoscale Science and Engineering
ZIM	Zero Index Metamaterial

List of Publications

Portion of this dissertation have been drawn from the following publications and manuscripts:

1. **<u>Y. Yang</u>**, Abdelaziz Boulesbaa, I. Kravchenko, D. Briggs, Alexander Pretzky, David Geohegan and J. Valentine, "Nonlinear Fano-resonant Dielectric Metasurface", submitted to *Nature Communications*.
2. **<u>Y. Yang</u>**, I. Kravchenko, D. Briggs and J. Valentine, "All-dielectric metasurface analogue of electromagnetically induced transparency", ***Nature Communications, 5,*** 5753 (2014)
3. **<u>Y. Yang</u>**, W. Wang, P. Moitra, I. Kravchenko, D. Briggs and J. Valentine, "Dielectric meta-reflectarray for broadband polarization conversion and optical vortex generation", ***Nano Letters*** 14, 1394 (2014)
4. P. Moitra[†], **<u>Y. Yang</u>**[†], Z. Anderson, I. Kravchenko, D. Briggs and J. Valentine, "Realization of an all-dielectric zero-index optical metamaterial", ***Nature Photonics*** 7, 791 (2013) ([†]: equal contribution)

Chapter 1 Introduction

1.1 What is an Optical Metamaterial?

Engineering material properties at will has long been a dream for scientists. However, natural materials are composed of individual atoms tightly arranged with separation on the order of angstroms; therefore, tailoring material properties through designing and synthesizing materials composed of "artificial" atoms can be an extremely challenging task due to the current technological constraints.

However, the task to engineer, specifically, the optical properties of materials at will can be much easier to accomplish through metamaterials. An optical metamaterial is a composite formed from so-called "meta-atoms". In order to have the composite of "meta-atoms" be treated as a homogeneous effective material for light, the unit cell size needs to be smaller than the wavelength of light (typically on the order of microns), while it can be much larger than that of the real atoms. Fortunately, the advances in nanotechnology have now enabled us to create the optical version of "meta-atoms" through either top-down or bottom-up fabrication techniques.

Metamaterials free us from the constraints of naturally occurring materials and allow for full control over light flow through the design of artificial "meta-atoms". Careful design of each unit cell can enable a wide variety of new material properties. During the rapid development of metamaterial research in the last decade, many previously science-fiction-like material properties and devices have been realized, including but not limited to negative refractive index[1]–[3], sub-diffraction-limit superlenses[4]–[6] and invisibility cloaks[7]–[10].

1.2 Engineering Optical Properties of Materials

The most common way that we can define and understand the optical properties of an material is based on their constitutive properties: electric permittivity, ε, and magnetic permeability, μ. These properties describe how the material interacts with light. Permittivity is a measure of how the applied electric field interacts with the medium and permeability measures the response of a material to an applied magnetic field. To develop a better understanding of this, we can derive the wave equation for light propagation through a homogeneous medium from the Maxwell's equations,

$$
\begin{aligned}
\nabla \cdot \mathbf{B} &= 0, \\
\nabla \times \mathbf{E} &= -\frac{\partial \mathbf{B}}{\partial t}, \\
\nabla \cdot \mathbf{D} &= \rho, \\
\nabla \times \mathbf{H} &= \mathbf{j} + \frac{\partial \mathbf{D}}{\partial t},
\end{aligned}
\tag{1.1}
$$

where $\mathbf{E}$ is the electric field, $\mathbf{H}$ is the magnetic field, $\mathbf{B}$ is the magnetic flux density, $\mathbf{D}$ is the electric flux density, ρ is the charge density, and $\mathbf{j}$ is the current density.

Combining equations (1.1) with the constitutive relations,

$$
\begin{aligned}
\mathbf{D} &= \varepsilon \mathbf{E} = \varepsilon_r \varepsilon_0 \mathbf{E} \\
\mathbf{B} &= \mu \mathbf{H} = \mu_r \mu_0 \mathbf{H}
\end{aligned}
\tag{1.2}
$$

we can arrive at the wave equations,

$$
\begin{aligned}
\nabla^2 \mathbf{E} &= \mu \varepsilon \frac{\partial^2 \mathbf{E}}{\partial t^2} \\
\nabla^2 \mathbf{B} &= \mu \varepsilon \frac{\partial^2 \mathbf{B}}{\partial t^2}
\end{aligned}
\tag{1.3}
$$

where $\varepsilon_0 = 8.85 \times 10^{-12}$ F/m is the permittivity of vacuum, and $\mu_0 = 1.26 \times 10^{-6}$ H/m is the vacuum permeability; ε_r and μ_r are the relative permittivity and permeability, respectively; and the refractive index of an material is then defined as $n = \pm\sqrt{\varepsilon_r \mu_r}$. The

wave equations govern how electromagnetic wave interacts with matter, and can be applied to form the complete description of light transmission, reflection, refraction, scattering and absorption. In Fig. 1.1, we group materials based on the sign of their ε and μ. The signs of these properties determine many of the unusual responses that can be engineered. Most natural materials have positive ε and μ and thus fall into quadrant I of this graph. Materials with negative ε but positive μ fall into quadrant II and include metals, heavily doped semiconductors, or ferroelectric materials that can have negative values of ε below the plasma frequency. The third quadrant is where we find negative index materials, with both negative ε and negative μ. The last quadrant of this material landscape is where ε is positive, but μ is negative. There are also very few natural materials in this regime, although some ferrite materials exhibit these properties at microwave frequencies. It should also be noted that there is a special region lying in the center of the graph, where ε and μ both approach zero. At such a region, the refractive index of the material approaches zero, while the impedance of the material $Z = \sqrt{\mu/\varepsilon}$ can be matched to the free space.

Much of the exciting research in metamaterials and plasmonics is tied to the fact that we can engineer both the electric and magnetic "arms" of light, ignoring the constraints on ε and μ imposed by naturally occurring materials.
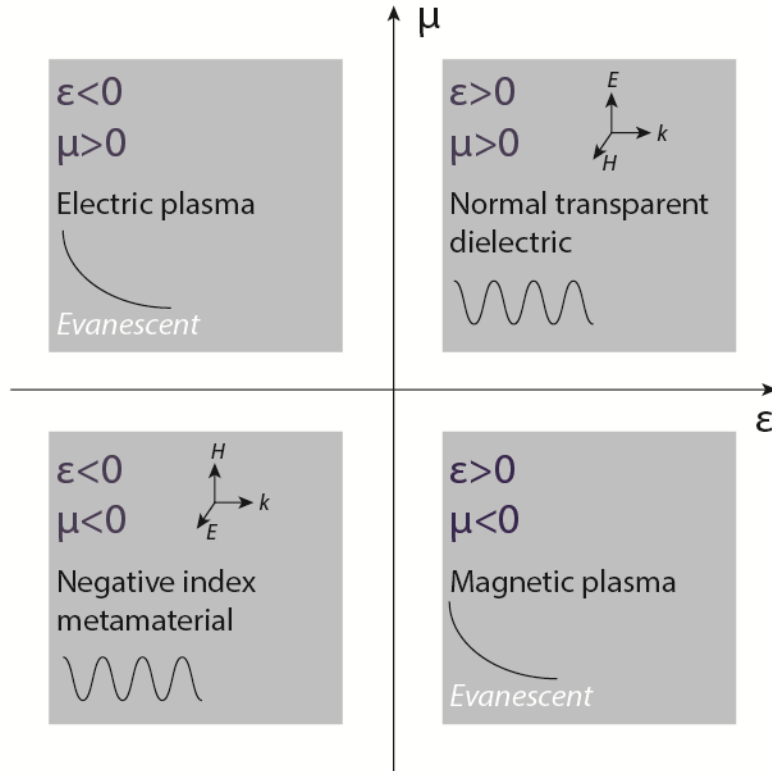
Figure 1.1. Available optical properties of materials characterized by the electric permittivity (ε) and magnetic permeability (μ).

1.3 Components of Conventional Metamaterials

The original idea of a negative index material, one of the most commonly mentioned metamaterials, was first outlined by Veselago in 1968[11]. This type of material has been referred to conceptually as a left-handed material as one of the effects of negative n is a reversal of the direction of propagation of the incident wave, thus breaking the right-hand rule of elementary physics. However, the first experimental realization of an actual left-handed material arrived almost 30 years after the original proposal [13].

To construct a metamaterial with a negative, or any other arbitrary refractive index, it is necessary to engineer the response of the material to both the electric and magnetic "arm" of the impinging light. To create a material with negative electric

permittivity is in fact quite straightforward. Many naturally occurring materials such as metal and highly-doped semiconductors possess a negative permittivity at frequencies below their plasma frequency. With unbound quasi-free electrons the dielectric function can be described using the Drude model,

$$\varepsilon(\omega) = 1 - \frac{\omega_p^2}{\omega(\omega - i\gamma)} \qquad (1.4)$$

where $\omega_p = n_e e^2 / \varepsilon_0 m_e$ is the plasma frequency of the metal or semiconductor, and γ is the damping coefficient. However, using only naturally occurring materials it is difficult to acquire the artificial permittivity at the desired operating frequency since the electron density and therefore the plasma frequency of metal can hardly be modified.
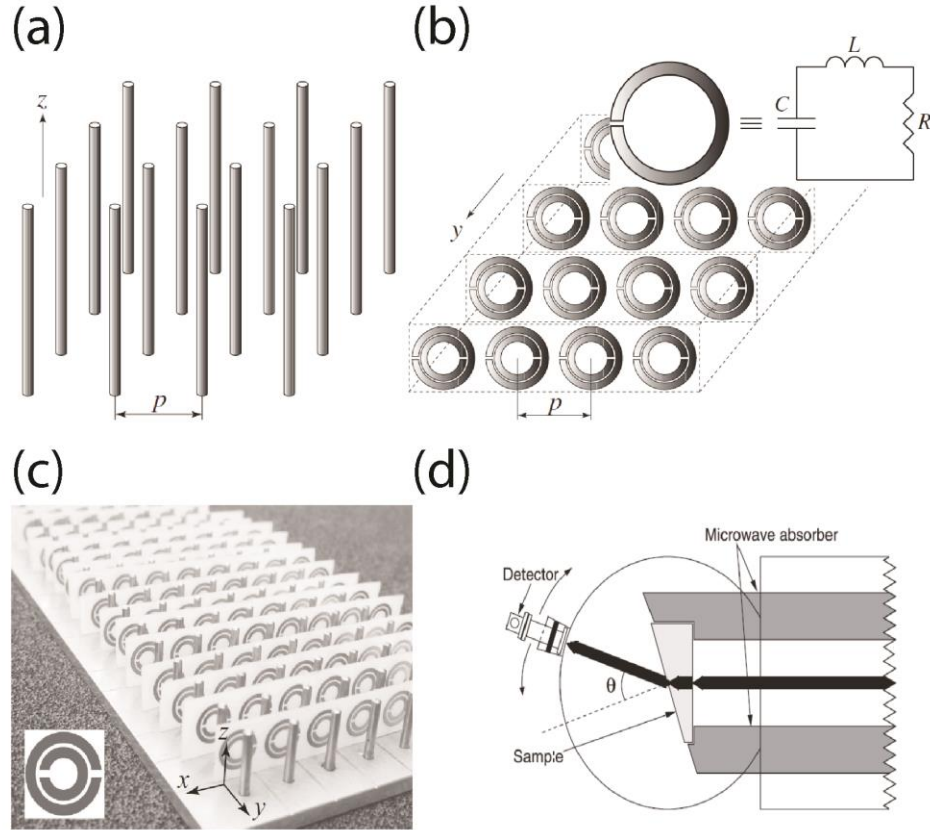
Figure 1.2. (a) Metal wire structure exhibiting negative ε [12]. (b) Split-ring resonator (SRR) structure exhibiting negative μ, introduced by Pendry *et al*. The inset shows the equivalent circuit model for the SRR[13]. (c) First experimental negative index structures, constituted of metal wires and SRRs, introduced by Smith *et al*[14]. (d) Experimental set-up for the measurement of left-handedness of the metamaterial structure shown in panel (c) at 5 GHz [1].

To achieve a designer permittivity, the effective medium approach can be taken. In other words, one can manufacture a "diluted metal" by embedding the metal in a dielectric background medium. For example, metallic wires with a permittivity ε_m can be embedded in a host dielectric medium of permittivity ε_i, as is schematically shown in Fig. 1.2(a). According to the effective medium theory, for a metallic wire grid, the effective permittivity of the composite material along the wire axis can be described simply as,

$$\varepsilon_{eff} = f\varepsilon_m + (1-f)\varepsilon_i \tag{1.5}$$

where f is the filling fraction of the metal. Therefore, by simply tuning the filling fraction of the metal, one can achieve a large tunability of the permittivity of the composite material.

Creating a material with negative magnetic permeability can be much more complicated, as in the optical frequencies there is no magnetic response ($\mu = 1$) in naturally-occurring materials. In fact, the creation of artificial magnetism was the biggest impediment of the realization of negative refractive index after Veselago's theoretical proposal. In 1999, Sir John Pendry proposed one approach to realize the high frequency magnetism using the so-called "split-ring resonator (SRR)"[15], as is shown in Fig. 1.2(b). The response of the SRR can be described using equivalent circuit theory where the SRR is treated as a LC circuit with a natural resonant frequency of $\omega_0 = \sqrt{1/LC}$, where L is the effective inductance and C is the effective capacitance of the structure. When the frequency of the incident wave equals the resonant frequency ω_0, the incident wave can drive a circulating current through the resonator, inducing a strong magnetic dipole moment, leading to the following expression for μ_{eff},

$$\mu_{eff}(\omega) = 1 - \frac{F\omega^2}{\omega^2 - \omega_0^2 + i\Gamma\omega} \tag{1.6}$$

where F is the area filling fraction of the SRR, and Γ is the damping term.
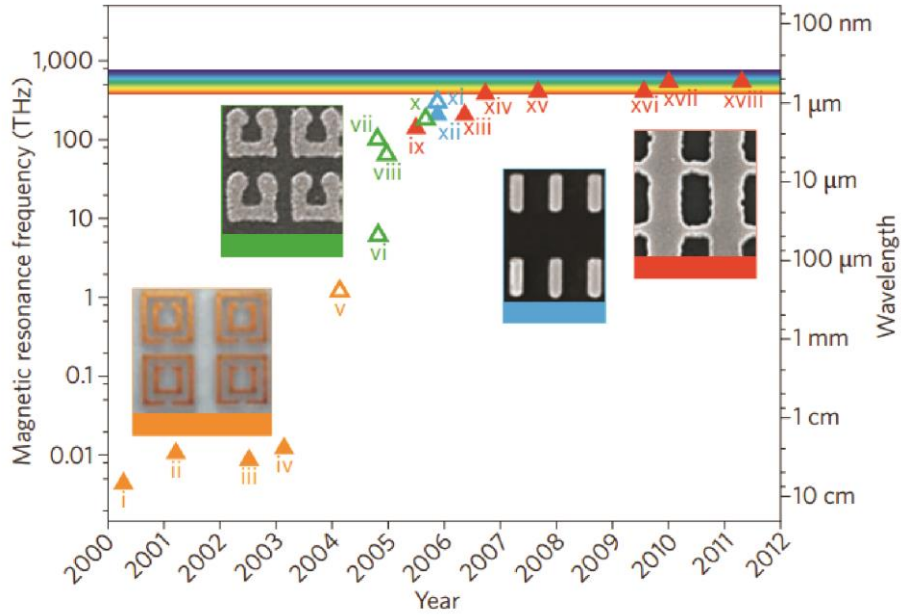
Figure 1.3. Development of magnetic metamaterials as a function of operation frequency and time. Orange: double SRRs[14]; green: U-shaped SRRs[16]; blue: metallic cut-wire pairs[17]; red: double fishnet structures[3]. The four insets show optical or electron micrographs of the five kinds of structure. Figure adapted from ref. [18].

Through proper engineering, negative permittivity and permeability can be overlapped at the same operating frequency, leading to an effective negative refractive index. In 2000, Smith, for the first time, experimentally demonstrated a material possessing negative refractive index at microwave frequency by combining metallic wires and SRRs[14]. The device photograph and a prism-based measurement set-up is shown in Fig. 1.2(c)-(d). Following that, there has been a constant drive to shrink down the unit cell size of the metamaterial and therefore to move its operating band to terahertz and higher frequencies. To date, negative or zero index metamaterials up to visible frequencies have been reported, as is summarized in Fig. 1.3. However, there are still significant issues associated with the current-generation of optical metamaterial devices. One particular problem is the large ohmic loss from metals at high frequencies.

8

Overcoming this problem will be one focus of this thesis and will be discussed in detail later.

1.4 Metamaterials beyond Engineered Refractive Index

Although metamaterial research was initially focused on the possibility of realizing negative refractive index, the scope of research has gone far beyond this point. For example, transformation optics has opened a new avenue for us to route light around an object, leading to an effective invisibility cloak[8]–[10], [19], [20]; chiral metamaterials have enabled us to manipulate different polarization states of light[21], [22]. Here I elaborate a few research directions most relevant to this thesis:

1.4.1   Spatially-varying 2D Metasurfaces for Phase Control

After more than a decade of research into metamaterials a low-cost and easy-to-implement technique for fabricating three-dimensional (3D) optical metamaterials still has not been found, though moderate improvement have been made. Techniques such as two-photon lithography, projection membrane lithography, and molecular self-assembly suffer from low speed, high complexity, and low tunability. Gradually, researchers have begun to realize that ultrathin 2D meta-surfaces with designer properties can also be extremely versatile in controlling light-matter interactions but with a much easier fabrication requirement.

For example, conventional optical components such as lenses and waveplates shape the wavefront of light by relying on the gradual phase accumulation along distances much greater than the wavelength of light. However, recent developments in

ultrathin metasurfaces show that the dependence on propagation can be broken by introducing an abrupt change of optical properties at an interface. The metasurface is made of arrays of scatters such that control over the optical properties can be achieved by engineering the interaction between light and the scatterers. A spatially-varying array of antennas can be used to mold the intensity and/orphase, and therefore optical wavefronts can be designed at will. Fig. 1.4 lists several of examples showing how 2D plasmonic metasurfaces can be applied to realize anomalous refraction, polarization conversion, holograms, and enhanced the photonic spin-hall effect[23]- [22].
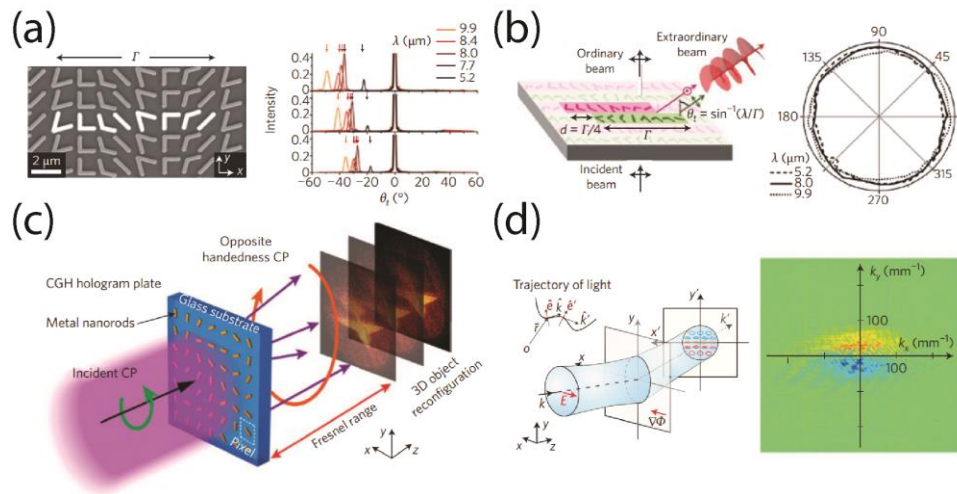
Figure 1.4. (a) Left: scanning electron microscopy image of a metasurface that generates a linear phase gradient via an array of V-shaped gold meta-atoms. The phase gradient mimics the effects of a blazed phase grating. Right: measured far-field intensity profiles[23]. (b) Left: schematic showing a metasurface quarter-wave plate. The unit cell consists of two subunits (pink and green) offset by $d = \Gamma/4$[24]. (c) Schematic demonstrating how a phase-graded metasurface can generate holograms. Each meta-atom acts as a phase modifying pixel that, on illumination with circularly polarized light, generates the required local phase profile for holographic reconstruction in the transmitted beam of opposite helicity[25]. (d) Left: on propagation through an appropriate metasurface, the rapid phase retardation generates a strong spin–orbit interaction leading to an accumulation of circularly polarized components in the transverse directions of the beam. Right: observation of the PSHE via measurement of the helicity of the anomalously refracted beam from a linearly phase-graded metasurface formed from V-shaped elements[26]. Figure adapted from ref. [27].

10

1.4.2 Metasurfaces with Designer Dispersion Profiles
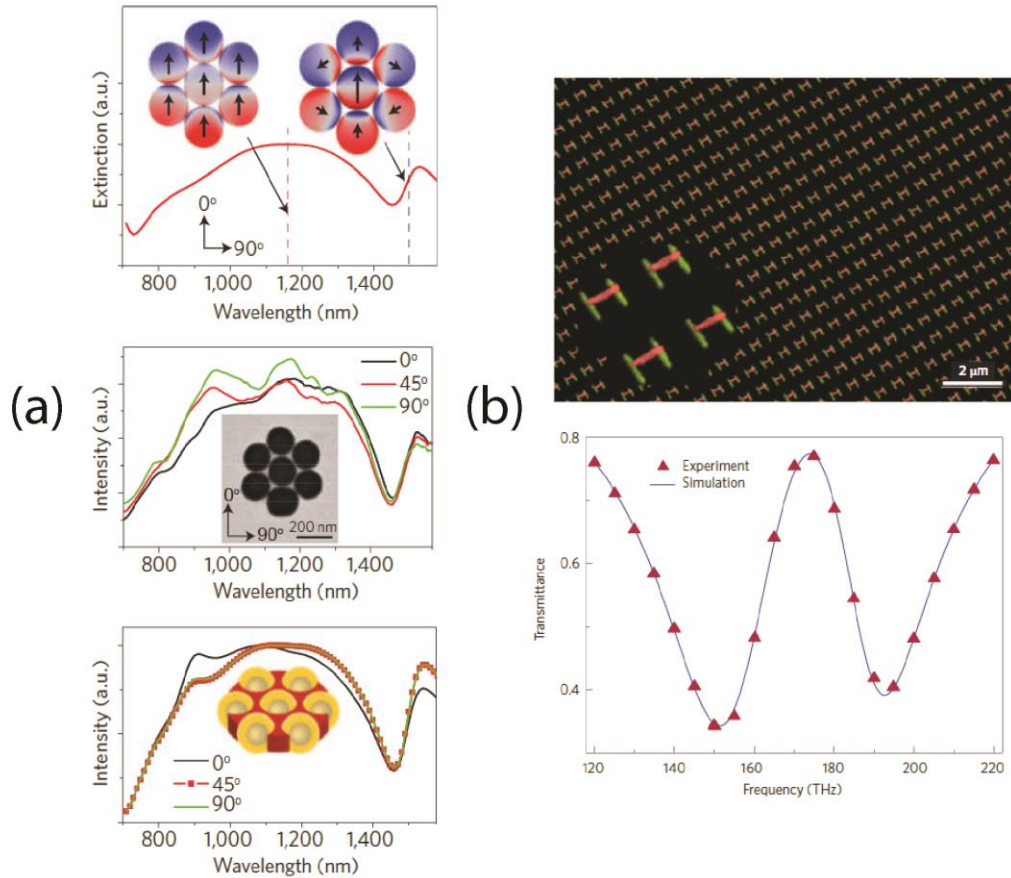
Figure 1.5. (a) Upper panel: calculated dipole amplitudes of the bonding and antibonding collective dipolar plasmon modes in a gold nanoshell heptamer. Measured (Middle panel) and calculated (Lower panel) scattering spectra of a gold nanoshell heptamer[28]. (b) Upper panel: scanning electron microscope image of the stacked plasmonic EIT analogue structure. The red color represents the gold bar in the top layer and the green color represents the gold wire pair in the bottom layer. Inset: enlarged view. Lower panel: experimental transmittance spectrum of the sample. The fitting curve was calculated from a Fano-type EIT model simulation[29]. Figure adapted from ref. [30].

Another major direction in metasurface research is to create planar structures with spectrally sharp, high-quality (-Q) resonances. The creation of the high-Q resonance

(typically deemed as Fano resonance) relies on the destructive interference of a "bright" and a "dark" mode resonator. If these two resonators are brought in close proximity in both the spatial and frequency domains, they can couple. This coupling leads to a resonance in the system, resulting from the interference between the two pathways. Due to the greatly reduced radiative loss of the excited dark resonant mode, the Fano resonance can be extremely sharp, resulting in complete transmission, analogous to electromagnetically induced transparency (EIT) from the sample across a very narrow bandwidth. Such resonances can be utilized to realize modulators with large modulation depth when active components such as "phase-change" materials or graphene are placed in close in vicinity. In addition, such a high-Q metasurface is well suited for ultra-sensitive detection of substances attached to it. For instance, an atomically-thin graphene layer can induce a multifold change in the transmission of a metasurface.

1.4.3   Nonlinear Metamaterials

Previous studies of metamaterials typically focus on the linear properties of the medium upon low intensity irradiation. However, with high intensity laser illumination, the responses of metamaterials may not necessarily scale linearly. The nonlinear optical response of a material can be described by,

$$\mathbf{D} = \varepsilon_0 \mathbf{E} + \varepsilon_0 \left(\chi^{(1)} \mathbf{E} + \chi^{(2)} \mathbf{E}^2 + \chi^{(3)} \mathbf{E}^3 ... \right) \tag{1.7}$$

where $\chi^{(n)}$ is the n-th order nonlinear susceptibility.

Nonlinearity is the key for a variety of interesting and useful effects such as parametric frequency up-/down- conversion, power amplification, and power-dependent light transmission. Due to the great flexibility in terms of tuning the optical near-field and

therefore the effective nonlinear susceptibility, metamaterials have been proposed to greatly boost the efficiency of harmonic generation[32] for phase mismatch-free four wave mixing and even all-optical light modulation[34].
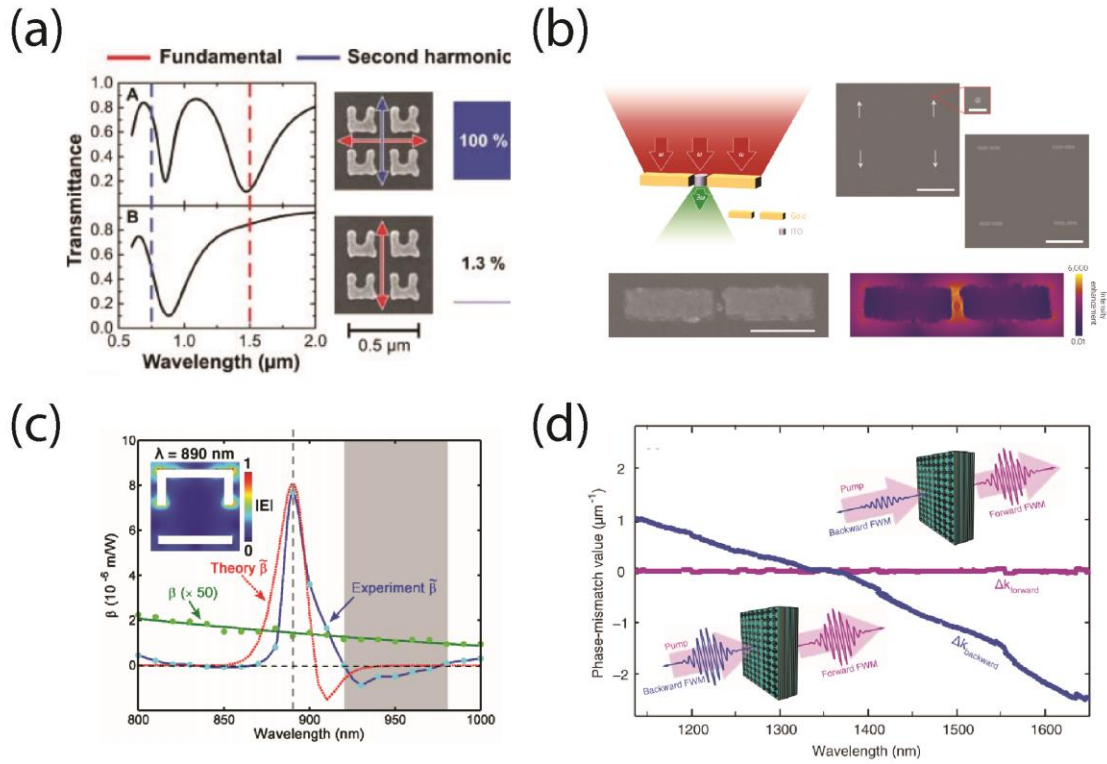
Figure 1.6. (a) Second harmonic generation from an array of SRRs exhibiting magnetic resonances[31]. (b) Third harmonic generation from a plasmonic bowtie antenna coupled to an ITO nano-crystal[32]. (c) Schematic demonstrating all-optical modulation from a plasmonic metasurface[33]. (d) Schematic showing phase mismatch-free four wave mixing[34].

1.5 Plasmonic Metamaterial Challenges

To date, most proposed metamaterial designs are based on subwavelength metallic (plasmonic) resonators. For example, the first experimental realization of a negative index metamaterial was based on the use of copper split-ring resonators at

microwave frequencies[35]. Other variations such as plasmonic fishnet structures have also been proposed to simplify the realization and reduce loss at optical frequencies[9], [36]. However, plasmonic metamaterials suffer from several key problems. First, metal suffers from conduction loss at high frequencies, and such loss can be greatly amplified when resonances are present. Although loss compensation methods such as incorporating gain materials have been proposed, they tend to greatly complicate the device layout[37]. Secondly, metallic resonators normally do not possess an isotropic optical response. Several authors have suggested methods to construct isotropic metamaterials by combining metallic SRRs and wires. However it is difficult to fabricate bulk arrays with complex geometries that are submicron or nanoscale in size. Thirdly, the magnetic response of metals tends to saturate at high frequencies due to the permittivity approaching zero[38]. This limits the realization of plasmonic metamaterial to visible and ultra-violet frequencies.

1.6 Resonant Dielectric Metamaterials

The above-mentioned problems associated with plasmonic metamaterials give us a reason to consider alternative routes such as switching the metamaterial constituents to dielectrics, where the intrinsic material loss can be much less. Unlike the resonance in metal structures which is due to the conduction current on the surface, Mie resonances in dielectric particles result in magnetic and electric dipole like fields via displacement current. In the case of spheres or cubes, the lowest resonance frequency corresponds to a magnetic dipole and the second resonance corresponds to an electric dipole (Fig. 1.7). If an array of these particles is assembled into unit cells, these resonances can be used to

tailor the effective permeability (μ) and permittivity (ε) of the composite.
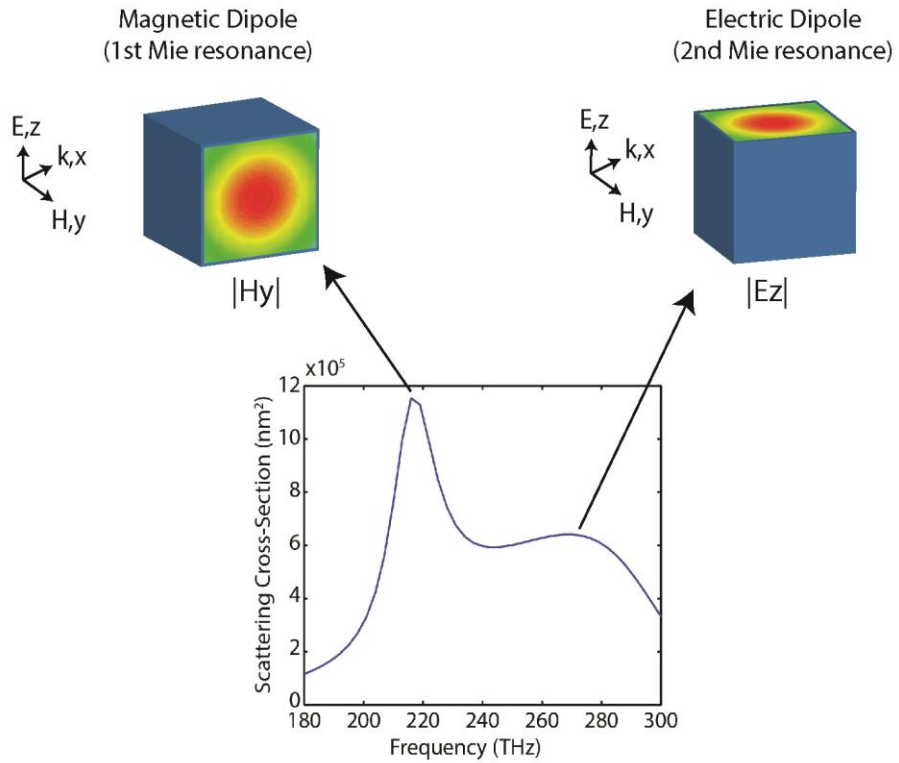
Figure 1.7. Illustration of Mie resonances in dielectric cubes. The curve shows the scattering cross-section (SCS) of a Si nano-cube with a length of 500 nm. The two peaks in the SCS plot correspond to a magnetic and electric dipole resonance, respectively.
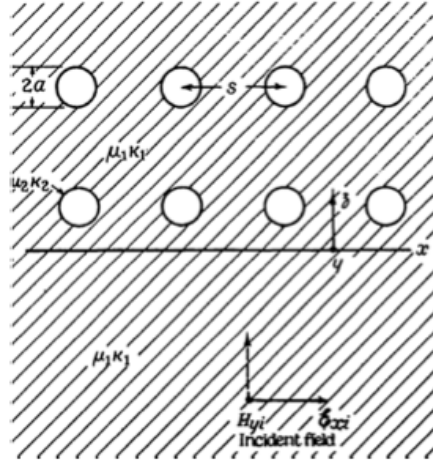
Figure 1.8. Schematic showing an array of dielectric spheres with permittivity ε_2 embedded in a host medium with permittivity ε_1 [39].

The first theoretical prediction of negative effective permeability (μ) and permittivity (ε) in dielectric materials was provided by Lewin back in 1946. In his paper "The Electrical Constants of a Material Loaded with Spherical Particles" [39], he investigated the optical response of a dielectric sphere array with a permittivity of ε_2 embedded in a dielectric host medium with a permittivity of ε_1. By rigorously applying the Mie scattering theory and combining it with Clausius-Mossotti effective medium theory, he predicted the condition for $\varepsilon_{eff} < 0$ to be,

$$\frac{3v_f}{\dfrac{F(\theta)+2b_e}{F(\theta)-b_e}-v_f} < -1 \tag{1.7}$$

where,

$$F(\theta) = \frac{2(\sin\theta - \theta\cos\theta)}{(\theta^2 - 1)\sin\theta + \theta\cos\theta},$$

$$\theta = k_0 a \sqrt{\varepsilon_{r2}' \mu_{r2}'}, \tag{1.8}$$

$$b_e = \frac{\varepsilon_1}{\varepsilon_2},$$

and v_f is the filling fraction of the dielectric spheres. A similar condition holds for

$\mu_{eff} < 0$.
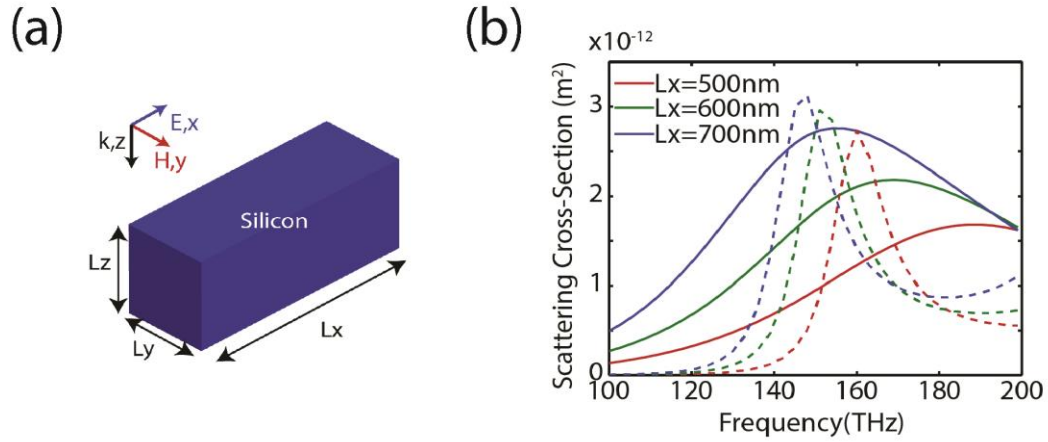
Figure 1.9. (a) Schematic of a silicon nano-rectangle antenna with length L_x, width L_y and height L_z. (b) The scattering cross-sections of the silicon nano-antenna as a function of the antenna length Lx. The solid lines represent electric dipole resonance, and the dashed line represent the magnetic dipole resonance.

Mie resonances occur in any dielectric particle and their ordering and spectral location can be controlled by the size or shape of the resonator. The advantage of dielectrics over their metallic counterparts is that they allow the frequency of operation to be scaled to arbitrary wavelengths and they experience reduced optical absorption, provided a transparent dielectric is used as the resonator. Furthermore, in the case of spheres or cubes, isotropic optical properties are possible while still employing simple

17

unit cell geometries, opening the door to scalable 3D metamaterials.

Experimental demonstrations and designs of dielectric metamaterials have primarily been limited to the microwave frequency range where constituent materials with permittivity in excess of $\varepsilon = 100$ are available, allowing deep sub-wavelength unit cells[40]. In the limit of low constituent permittivity, the unit cell's resonance position becomes comparable to the excitation wavelength, invalidating homogenization. Dielectric metamaterials have been shown to exhibit many of the same properties as metallic metamaterials including high frequency magnetism and a negative refractive index[41]–[44]. It is important to note that to achieve the more complicated negative index response it is necessary to overlap both an electric and magnetic resonance. Despite these proposals, experimental realizations of dielectric based metamaterials at optical frequencies have been slow to materialize. At the inception of the research outlined in this thesis, the highest frequency of operation which has been experimentally demonstrated is 40 THz which was achieved using high index tellurium cubes as the unit cell. However, in this demonstration a single resonator was used in the unit cell, resulting in no overlap in the electric and magnetic response[45]. Researchers have also begun to examine the magnetic response and Fano resonances present in dielectric particles at optical frequencies[46], though no metamaterials have been formed from them until the inception of this thesis.

1.7 Organization of the Thesis

In this thesis, I present my efforts to realize resonant dielectric metamaterials at optical frequencies. Such developments will hopefully lead to novel compact optical

devices with superior performance and ultimately practical applications. In particular, I will present *how artificially-designed dielectric nano-structures can be applied for efficiently controlling light emission, propagation, bio-sensing, and enhancing nonlinear light-matter interaction with greatly improved performance over plasmonic devices.*

Chapter 2 describes the first experimental realization of a low-loss 3D zero-index metamaterial (ZIM) with all-dielectric components at optical frequencies. A composite engineered structure exhibiting an effective refractive index of zero is designed and fabricated based on low-loss silicon (Si) material. Due to the isotropic nature of the ZIM, I demonstrate the ability to control the spontaneous emission of light by embedding quantum dot emitters within the ZIM and observing directional and enhanced light emission.

In **Chapter 3**, I transition the focus from bulk 3D dielectric metamaterials to ultrathin 2D dielectric metasurfaces. I show that engineered dielectric nano-antennas exhibiting Mie resonances can be used in place of plasmonic antennas to drastically modify the phase of light while maintaining near-unity efficiency. I experimentally demonstrate highly efficient broadband linear polarization conversion and optical vortex generation with a silicon-based meta-reflectarray.

Chapter 4 is a study of the possibility of using dielectric nanoantenna arrays to mimic electromagnetically induced transparency (EIT) and to realize Fano-type resonances with ultrahigh quality factors. This is realized by forming a periodic array of coupled electric and magnetic dipole antennas and the associated minimized non-radiative decay of light. Combining the sharp resonance with strong field confinement in its surrounding medium, I show that such a device can be an ideal platform for bio-

sensing.

In **Chapter 5**, I further investigate the nonlinear light-matter interaction in the Fano-resonant dielectric metasurface. The metasurface results in strong near-field enhancement within the volume of the silicon resonator while minimizing two photon absorption, leading to greatly enhanced efficiency and saturation power for third harmonic generation. The enhanced nonlinearity, combined with a sharp linear transmittance spectrum, results in transmission modulation via the Kerr effect with a large modulation depth.

In **Chapter 6**, I will discuss one possible way to integrate the concept of Mie resonances with active material systems such as quantum wells. By overlapping the electric and magnetic resonances, these hybrid structures can achieve near-unity light absorption in the quantum wells, leading to greatly enhanced quantum efficiency of a quantum well-based infrared photodetector.

Finally, **Chapter 7** summarizes the highlights of this work and its long term implications. In the end, I would like to give my perspective on the future of metamaterials.

Chapter 2 3D Dielectric Metamaterials — Zero Refractive Index

2.1 Introduction
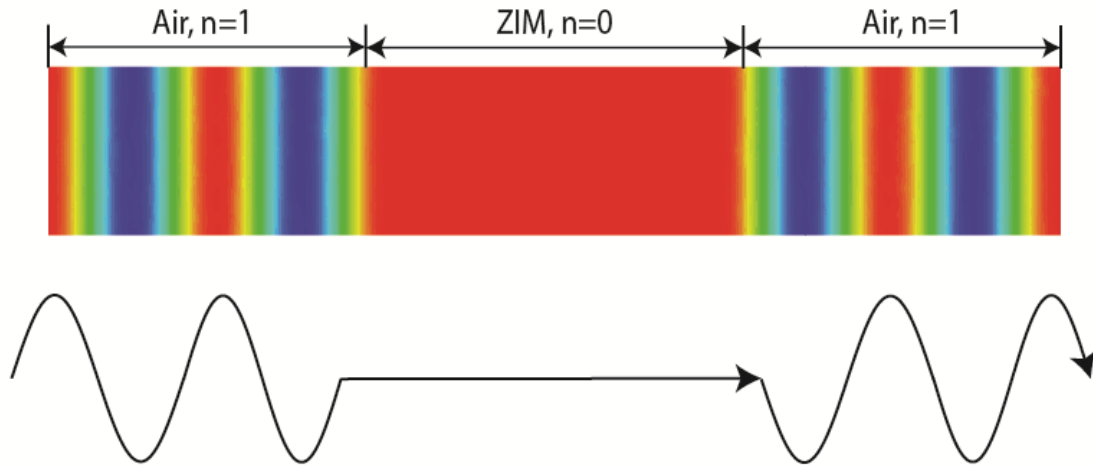
Figure 2.1. Schematic of light propagation in the air and ZIM, respectively.

Over the past decade, one of the key goals of metamaterial research has been to realize materials with arbitrary effective refractive index such that we can tailor the propagation of light at will. Recently, metamaterials with refractive index equal to zero have drawn particular interest. Waves traveling inside such a medium do not experience any spatial phase change and the phase velocity approaches infinity, as is illustrated in Fig. 2.1. These properties can be used for realizing directional emission[47]–[49], tunneling waveguides[50], large-area single-mode devices[51] and electromagnetic cloaks[52]. In the past, most work aimed at achieving zero-index has been focused on epsilon-near-zero metamaterials (ENZs) which can be realized using diluted metals or metal waveguides operating below cut-off. These studies have included experimental

demonstrations in the microwave[47], [53], mid-IR[54], and visible[55] regimes. ENZ metamaterials have a permittivity that is near-zero and a permeability of unity, resulting in a near-zero refractive index; however, since the permeability remains finite, the relative optical impedance is inevitably mismatched from free-space, resulting to large reflections from the interface. Impedance matched zero-index metamaterials (ZIMs) in which both the permittivity and permeability are set to zero eliminate these strong reflections and have recently been demonstrated at optical frequencies using metal based fishnet structures. However, fishnet metamaterials do not possess isotropic optical properties and the use of metals inevitably introduces ohmic loss that will limit the thickness of the material.

As is discussed in detail in Chapter 1, resonant all-dielectric metamaterials offer one potential solution to these issues due to the absence of Ohmic loss, and their simple unit-cell geometries[57]. However, while magnetic modes in high-index particles have recently been characterized experimentally at optical frequencies[58], [59], implementations of dielectric metamaterials have been limited to the microwave[42], [43], [57] and mid-infrared[44] regimes up to the inception of this work.

In this chapter, I detail the first experimental demonstration of an all-dielectric ZIM operating at infrared frequencies. The design of the metamaterial is based on a recent proposal reported by Chan et. al.[60] in which it was shown that a metamaterial made of purely dielectric high-index rods can exhibit a Dirac cone at the point in the band structure, a feature that is similar to the electronic band structure in graphene[61]. At the Dirac point, the metamaterial exhibits zero effective permittivity and permeability, resulting in an impedance-matched ZIM. Experiments at microwave frequencies have

22

demonstrated some of the unique properties arising from an effective index of zero, such as cloaking and lensing. However, a demonstration at optical frequencies has yet to be provided. Here, we implement a ZIM at optical frequencies using vertically stacked silicon rods, allowing access from free space. We demonstrate that the optical ZIM serves as an angular optical filter while also enhancing the directivity of spontaneous emission from quantum dot light sources embedded inside the structure. The experimental results, together with numerical calculations, serve as direct evidence of impedance-matched near-zero index within the metamaterial.

2.2 Photonic Dirac Cone and Zero Index Design

The design of the ZIM consists of a stack of square cross-section Si rods embedded in SiO2 with w=t= 260 nm and a= 600 nm, is shown in Fig. 2.2(a). The band structure is computed for TM polarization with the electric field oriented along the rod axis and the Dirac cone like dispersion can be observed at the center of Brillouin zone where two transverse bands with linear dispersion intersect a flat quasi-longitudinal band, resulting in triple degeneracy, as is shown in Fig. 2.2(b). We utilized field-averaging of the Bloch modes[62] to retrieve the metamaterial's effective bulk optical properties (Fig. 2.2c) and simultaneous zero-permittivity and permeability are obtained at the triple degeneracy frequency of 211 THz (λ_0=1422 nm). This response is directly attributable to a linear combination of electric monopole and magnetic dipole Mie resonances within the Si rods (inset of Fig. 2.2c), allowing the effective constitutive parameters to be accurately extracted using effective medium theory[63]. This was confirmed by the excellent agreement between the extracted propagation vector, acquired using field averaging, and

23

the computed band structure around the triple degeneracy point. Furthermore, the impedance of the structure is also accurately represented using the effective constitutive parameters, further supporting the assignment of an effective permittivity and permeability for the structure. A relatively broadband impedance matched low-index region is present around the zero-index point and over the frequency range from 215 THz to 225 THz there exists only one propagating band, TM4, which allows us to define an effective index of refraction for the structure for off-normal angles of incidence. The isofrequency contours (IFCs) over this frequency range are shown in Fig. 2.2(d) and it can be observed that they maintain a nearly circular shape indicating that the material maintains a relatively isotropic low-index response for TM-polarized light over this bandwidth. This all-angle response is critical for preserving the unique physics associated with low- or zero-index materials such as directionally selective transmission and emission from within the material. It should be noted that in a perfectly homogeneous zero-index metamaterial, the flat longitudinal band is not accessible with TM-polarized light.
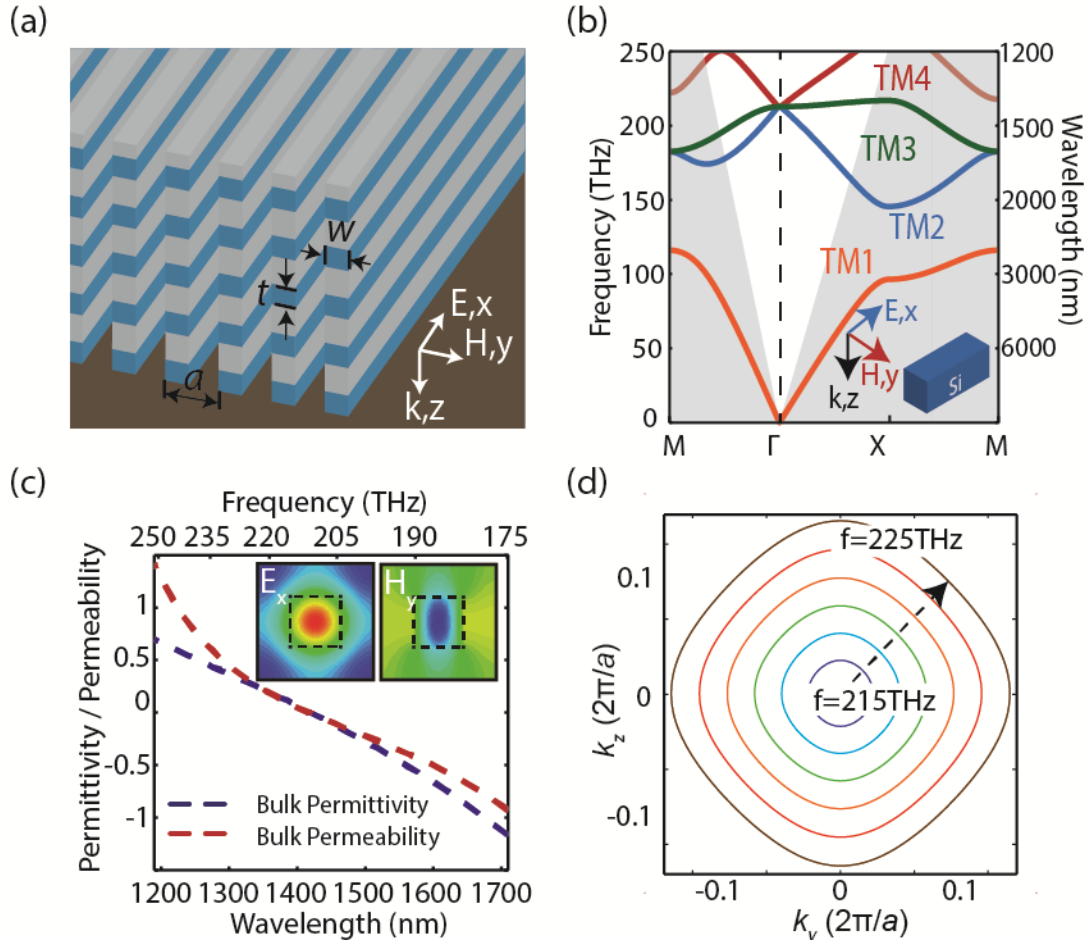
Figure 2.2. (a) Diagram of the ZIM structure with a unit cell period of a = 600 nm and w = t = 260 nm. (b) Band diagram of uniform bulk ZIM (infinitely thick) for TM polarization. Dirac cone dispersion is observed at the Γ point with triple degeneracy at 211 THz. The shaded area denotes regions outside the free-space light line. (c) Retrieved effective permittivity and permeability of the bulk ZIM acquired using field-averaging. The inset shows the electric and magnetic fields within a single unit cell at the zero-index frequency indicating a strong electric monopole and magnetic dipole response. (d) IFC of the TM4 band. The contours are nearly circular (i.e., isotropic) for a broad frequency range and increase in size away from the zero-index frequency indicating a progressively larger refractive index.

2.3 Fabrication and Optical Characterization

The fabricated ZIM consists of 200 μm long Si rods which support electric and magnetic resonances and the rods are separated by a low index material, silicon dioxide (SiO2) (Fig. 2.3). One of the consequences of a low or zero-index is that light will not be

guided using a conventional slab waveguide and thus the material must be fabricated for free-space access when metal or other reflective cladding layers cannot be utilized. To realize a free-space accessible material, fabrication began with a multilayer stack of 11 alternating layers of α-Si (ε=13.7, 260 nm thick) and SiO2 (ε=2.25, 340 nm thick) followed by a patterning and reactive-ion etching (RIE) (details in the Supporting Material). In the final step, poly(methyl methacrylate) (PMMA) (ε=2.23) was spin-coated onto the sample to fill the air gaps. Figure 2.3(e) shows a cross-section of the fabricated structure before final PMMA spin-coating and Figure 2.3(f) depicts a sample after spin-coating. A total of 5 functional layers (Si / SiO2 pairs) results in a metamaterial with a thickness of 3 μm, about twice the free-space wavelength at the zero-index point.
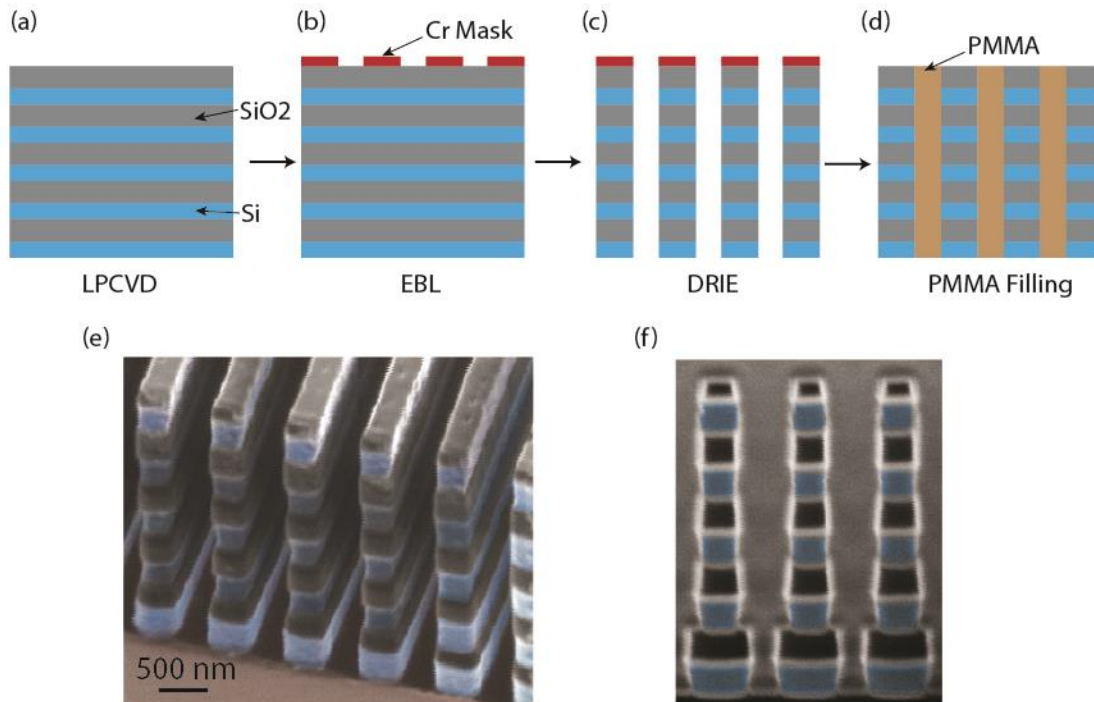
Figure 2.3. (a)-(d) Schematic of the detailed fabrication steps. (e)-(f) SEM image of the fabricated sample (e) before and (f) after PMMA filling.

The detailed fabrication steps of the ZIM are outlined in Fig. 2.3(a)-(d). We developed a unique low pressure chemical vapor deposition (LPCVD) process to deposit 11 alternating layers of α-Si (260 nm) and SiO2 (340 nm) during a single process run on a 4 inch quartz wafer. The LPCVD tool used was a horizontal tube furnace. A quartz caged boat was used to contain the wafer to improve cross wafer uniformity. Deposition temperature was 550°C and process pressure was 300mTorr and both were held constant throughout the deposition of both films. Process gases were introduced into the tube furnace via mass flow controllers. The α-Si layer was deposited by flowing 50sccm's of 100% SiH_4. The SiO_2 layer was deposited by flowing 85sccm's of SiH4 and 120sccm's of O_2. A brief N_2 purge was introduced between layers. This alternating process was repeated until the desired number of layers was deposited.

A hard metal etch mask was patterned using electron beam lithography (Raith and/or Jeol) and deposition of 50 nm chromium (Cr) followed by lift-off. To avoid surface charging detrimental effects, electron beam sensitive resist (ZEP520A and/or PMMA) was coated with a 10 nm Cr charge dissipation layer to be chemically removed prior to the exposed resist development. A fluorine based reactive ion etching (RIE) recipe was developed in an Oxford Plasma Lab tool to etch the multilayer sample by alternating the recipe for the Si and SiO_2 layers. The final structure has a 10:1 aspect ratio with respect to the total height and gap width between the rods. The base etch recipe involved 100 W RF power, 2000 W ICP power with C_4F_8 and O_2 gas flows for the SiO_2 layers and 80 W RF, 1200 W ICP with C_4F_8, SF_6, O_2 and Ar gas flows for the α-Si layers. The oxide had a positive slope as we etched down to subsequent layers underneath. Starting with the base recipe for the upper layers, the subsequent SiO_2 layers were etched

more aggressively with increasing depth. This was accomplished by changing the ratio of C_4F_8 and O_2 gas-flow which provided less passivation to the side walls during etching. The base Si etch recipe resulted in straight side walls until we reached the bottom most layer. The bottom most oxide and Si layers were etched with the most aggressive recipes and the top layers were protected by additional passivation steps. The metamaterial's internal structure was characterized by imaging the edge profile after milling cross-sections inside the array using focused ion beam milling (FIB). During all imaging, a thin layer of Cr was deposited on the sample to provide a conducting surface.

We made sure that PMMA, which was spin-coated on the sample after the RIE process, filled in the gaps completely in order to provide a background with the same permittivity as the SiO_2 spacer layers. The sample with a drop casted PMMA film was placed in an evacuated desiccator to remove air bubbles and this process was followed by spinning and soft baking (120 degrees for 2 minutes) twice and reflowing at 300° C for 2 minutes to reach the desired thickness. The final structure was cross-sectioned with FIB milling at multiple locations to confirm the complete filling.

In order to gauge the agreement with the simulated material properties, transmittance of the fabricated ZIM was acquired by illuminating the sample with normal-incident white light with the electric field oriented along the Si rod axis (Fig. 2.4). The simulated and measured transmittance show excellent agreement in spectral shape, though the experimentally obtained curve has a lower amplitude that is likely due to non-uniformity in rod width at the edges of the sample as well as surface roughness. The measured spectrum shows a peak transmission of 80% at 1405 nm, the spectral position corresponding to the impedance-matched low-index point. A dip in transmission also

occurs at 1460 nm, corresponding to the metallic region of the sample.
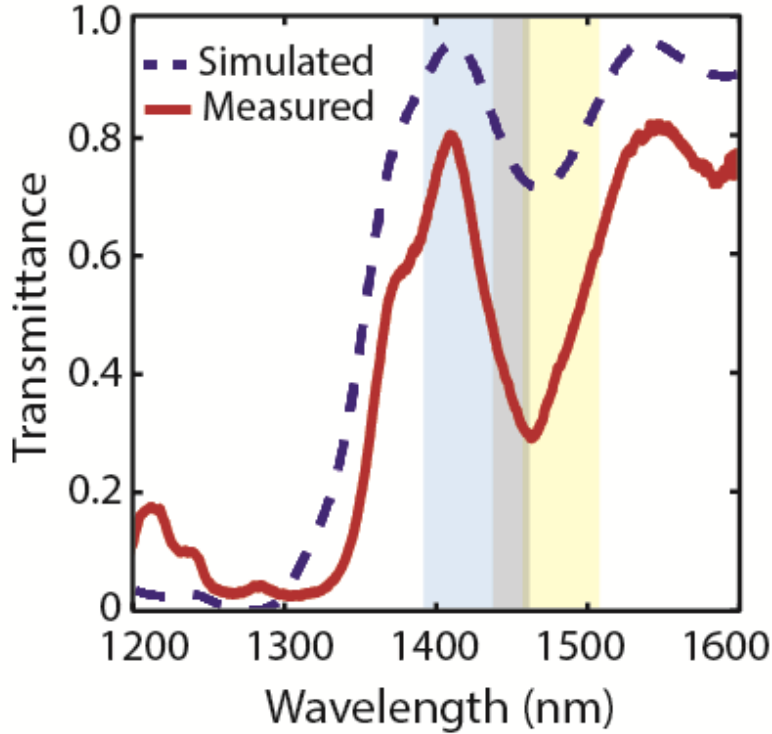
Figure 2.4. Experimental (red) and theoretical transmittance (dotted blue) curves of the ZIM (200 x 200 μm2 total pattern area). Regions corresponding positive index, metallic properties, and negative index are denoted with blue, grey, and yellow shading, respectively.

While these bulk parameters are used as a design guide, the fabricated metamaterial has both a finite thickness as well as non-uniform rod sizes and will thus deviate somewhat from the bulk parameters. To better understand the optical response of the fabricated metamaterial, full-wave finite-difference time-domain (FDTD) simulations were performed and S-parameter retrieval[64], [65] was used to compute the effective optical properties (Fig. 2.5a,b). Due to the non-uniform rod size, the impedance matched point in fabricated structure is shifted to 1400 nm corresponding to $n_{eff} = \mu_{eff} = \varepsilon_{eff} = 0.12$.

It can also be observed that a metallic region is opened from 1430 nm to 1460 nm in which the permittivity is negative while the permeability remains positive. The metamaterial exhibits a negative index region beginning at 1460 nm though this region cannot be assigned with optical properties for arbitrary angles of incidence due to presence of the quasi-longitudinal band which is accessible at large incident angles.
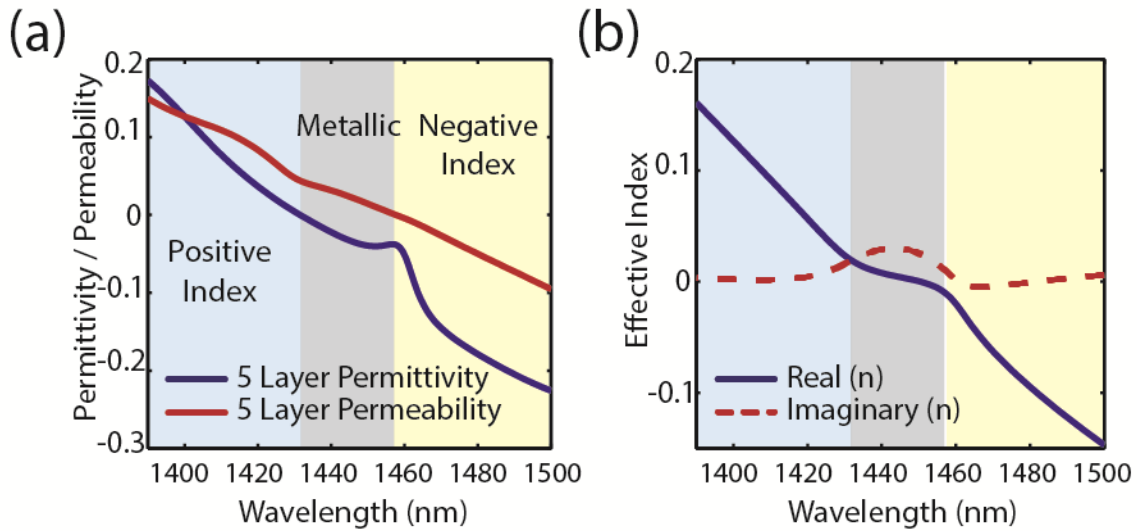
Figure 2.5. (a) Effective permittivity and permeability of the fabricated ZIM obtained using S-parameter retrieval. Regions corresponding positive index, metallic properties, and negative index are denoted with blue, grey, and yellow shading, respectively. (b) Effective refractive index of the fabricated structured obtained using S-parameter retrieval.

One of the most fascinating properties of isotropic low-index materials is that light incident from free-space is only transmitted over a narrow range of incidence angles. This effect is a direct consequence of phase matching at the interface which requires that the wavevector along the interface be conserved. As illustrated with the IFCs depicted in Fig. 2.6(a), in a low-index metamaterial, the wavevector is restricted to extremely small values causing light incident at high angles ($k_{y,0} > |k_{ZIM}|$) to be

reflected while near-normal incident light is transmitted ($k_{y,0} < |k_{ZIM}|$). This effect is evident when examining the simulated transmittance with regard to wavelength and angle of incidence (Fig. 2.6b) for the fabricated ZIM. The material exhibits near-zero transmission at off-normal incident angle within the positive index band centered at 1400 nm, with improving angular confinement in transmission as we approach the zero-index point. The presence of the quasi-longitudinal band within the negative index region ($\lambda_0 \sim 1475$ nm) is also apparent, allowing transmission at large incident angles.

To experimentally verify that the fabricated ZIM preserves these features, light transmitted through the sample was imaged in the Fourier plane. Illumination was provided by a femtosecond synchronously pumped optical parametric oscillator (Coherent, MIRA OPO) that was focused with a large numerical aperture objective (NA=0.85), providing incident angles up to 58.2°. The acquired Fourier images (Figs. 2.6. c-g) show confinement of light along the y-axis of the material which is in the direction of in-plane periodicity. Within the low index region between 1400 nm and 1475 nm, tighter confinement of k_y is observed with progressive lowering of the refractive index, in agreement with the simulated data. Confinement is absent in the *x*-direction due to the fact that the electric field is no longer directly along the rod axis for these incident angles. The directional filtering of transmission demonstrates that a nearly isotropic low-index for TM-polarized light is indeed preserved within the fabricated metamaterial.
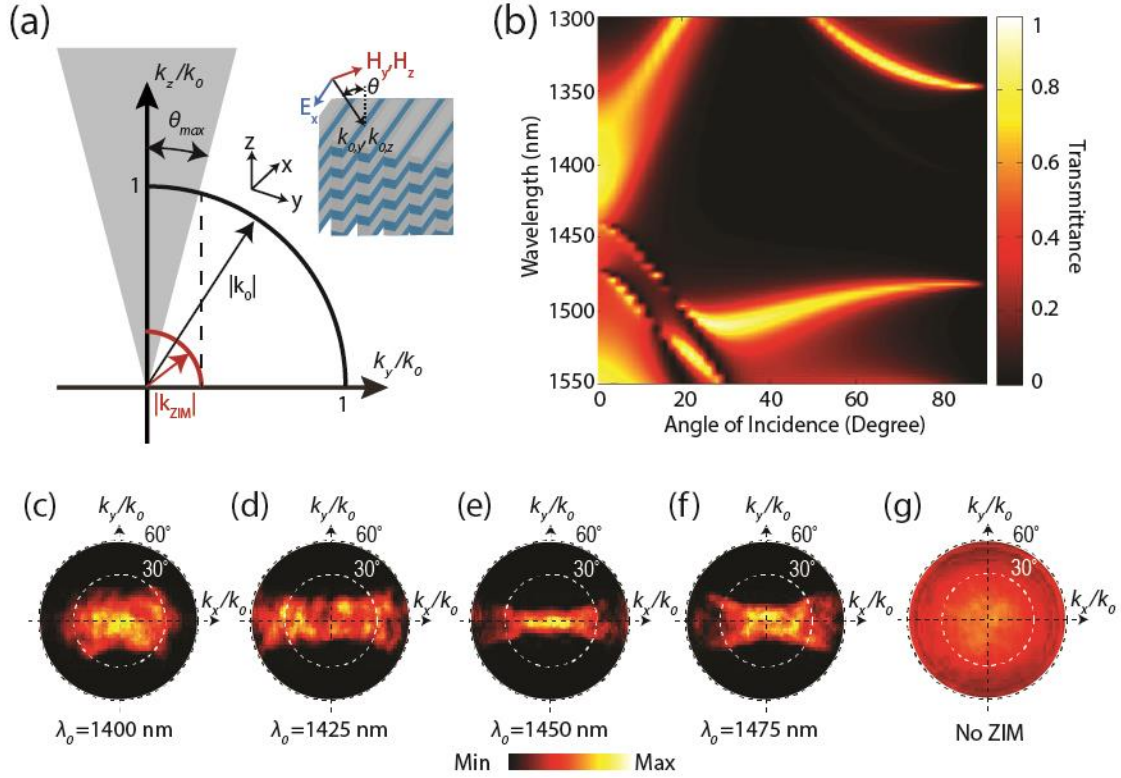
Figure 2.6. (a) IFCs of air and a low-index metamaterial illustrating angularly selective transmission due to conservation of the wave vector parallel to the surface. (b) Simulated angle and wavelength-dependent transmittance of the fabricated structure. (c)-(f) Fourier-plane images of a beam passing through the fabricated ZIM structure within the low index band. Angularly selective transmission can be observed in the *y*-direction due to the low effective index. Along the *x*-direction, angular selectivity is not preserved due to the one-dimensional nature of Si rods. (g) Fourier-plane image of the illumination beam demonstrating uniform intensity over the angular range measured.

2.4 Directive Quantum Dot Emission

An additional consequence of the near-zero spatial phase change is that incoherent isotropic emitters placed within the ZIM will tend to emit coherently in the direction normal to the air/ZIM interface[47]–[49]. To demonstrate this effect, we placed lead sulfide (PbS) semiconductor quantum dots (QDs) within the ZIM to act as the emitter. The QDs had a luminescence peak centered at 1420 nm and a full width at half maximum of 172 nm. The QDs were sandwiched between two PMMA layers within the

32

ZIM, and were excited with a tightly focused 1064 nm laser beam. The Fourier-plane images (Fig. 2.7c-d) from both an unstructured PMMA/QD film and QDs placed within the metamaterial show good angular confinement in the y-direction and an over two-fold increase in intensity emitted normal to the interface from the ZIM compared to the unstructured case. The increase in emission normal to the interface is a result of the uniform phase distribution within the ZIM, leading to constructive interference from emitters throughout the material[55], further supporting the realization of a near-zero refractive index. The constructive interference of multiple emitters is in competition with the reduced optical density of states associated with the low-index response. For instance, if the number of emitters is reduced to one, the emitted power in air will be greater than the ZIM in all directions. However, as expected for constructive interference within the material, the far-field intensity of waves propagating normal to the interface is proportional to the number of emitters squared. We also note that although the luminescence peak of the QDs matches the low-index band of fabricated ZIM structure quite closely, parts of the emission fall beyond the low-index band, resulting in slightly lower angular confinement compared with the transmission data.
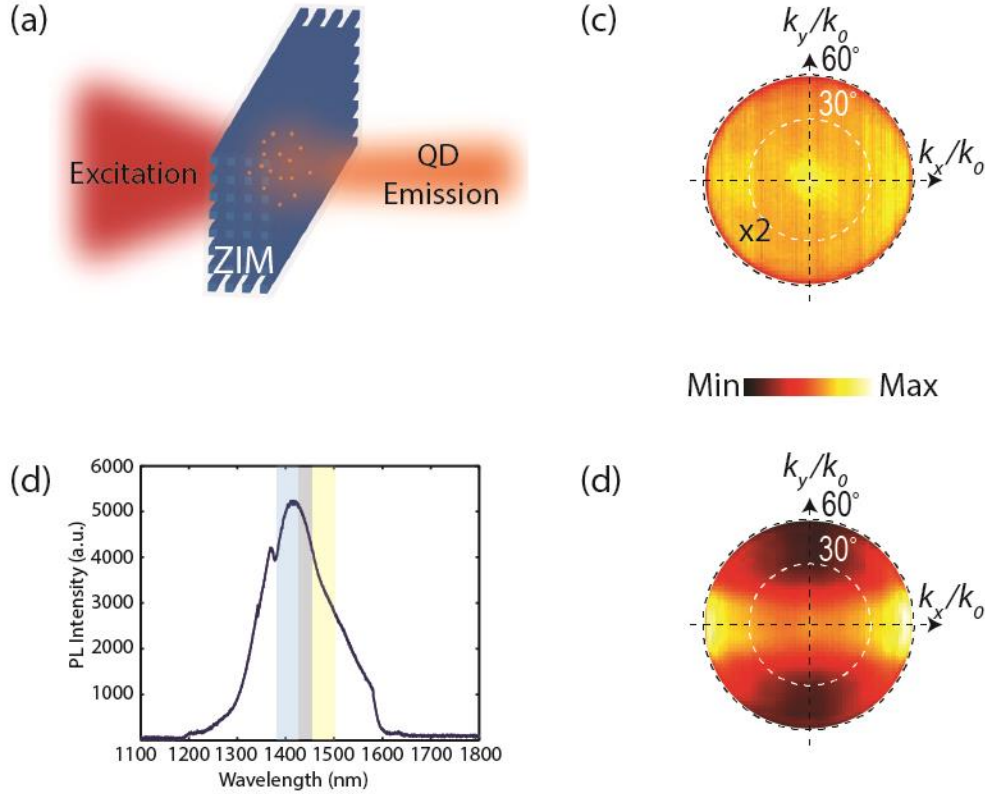
Figure 2.7. (a) Schematic of laser-pumped QD emission from within the ZIM structure. (b) Photoluminescence (PL) spectrum of PbS quantum dots (Evident Technology) used in the main text. The emission peak appears at 1425 nm, with a full-width at half-maximum of 172 nm. The blue-, gray- and yellow-shaded region corresponds to positive index, metallic properties, and negative index as acquired from S-parameter retrieval. The dip of measured luminescence spectrum at around 1380 nm is due to the water absorption line. **(c)** 2D Fourier-plane images of quantum dot emission on the substrate, intensity is scaled by two times. (d) 2D Fourier-plane images of QD emission within the ZIM.

2.5 Conclusion

To summarize Chapter 2, we have experimentally demonstrated the first all-dielectric zero-index metamaterial at optical frequencies, which exhibits a nearly isotropic low-index response for a particular polarization, resulting in angular selectivity of transmission and spontaneous emission. The realization of impedance-matched ZIMs at optical frequencies opens new avenues towards the development of angularly selective

optical filters, directional light sources and large-area single-mode photonic devices. Furthermore, the advent of all-dielectric optical metamaterials provides a new route to developing novel optical metamaterials with both low absorption loss and isotropic optical properties.

Chapter 3 2D Dielectric Metasurface — Meta-Reflectarray

3.1 Introduction

      While bulk 3D metamaterials are preferred for applications such as enhancing light emission and invisibility cloaking, there are other circumstances where efficient light manipulation over a small distance (for example, with an ultrathin 2D meta-surface) can be beneficial. Achieving full control over light propagation is an ever present issue in modern day optics. In order to realize such control it is necessary to create devices that allow 0 to 2π phase modulation and / or devices that allow control over the amplitude of light. In conventional optical elements such as birefringent waveplates and lenses, a significant propagation distance is needed to acquire disparate phase accumulation for different polarizations or spatial regions of the beam, thus requiring thick materials that are difficult to integrate into compact platforms[66]. One solution to this issue is the use of reflect and transmit-arrays, originally developed at radio frequencies, that allow one to control the amplitude and phase of light using a single, or several, layers of ultra-thin antennae[67], [68]. By changing the geometry of the antenna as a function of position, these arrays allow spatial control over the phase of light. Recently, similar materials, deemed metasurfaces, have been developed at optical frequencies[23]. Metasurfaces typically utilize asymmetric electric dipole resonances to allow 0 to 2π phase control for the cross-polarized scattered light. As in transmitarrays, varying the geometry of the resonator as a function of position allows arbitrary control of the phase front of light using a subwavelength-thin film and has led to demonstrations including anomalous refraction[23], [69]–[72], quarter and half waveplates[24], [73], lensing[74]–[76], and

manipulation of orbital angular momentum[77], [78].

One of the drawbacks of plasmonic metasurfaces is that they typically suffer from low efficiency due to weak coupling between the incident and cross-polarized fields. Methods to increase efficiency include the use of overlapped electric and magnetic resonances[79] as well as the use of thicker metasurface sheets[80], though both of these proposals require materials with increased complexity. One can also employ antennae working away from their resonance positions to realize quarter-waveplates with polarization conversion efficiencies of close to 50% over large bandwidths[81]. In another approach it was shown that an array of metallic antennae, in combination with a reflective ground plane, can achieve efficiencies of up to 80% for anomalous reflection[71], [76], [82] and linear polarization conversion[73] by introducing multiple reflections within the film. While this design avoids complexity, the use of metallic antennae still limits metasurfaces from achieving unity efficiency at optical wavelengths due to the Ohmic losses in metal[71].

D*ielectric metasurfaces* composed of a periodic or spatially-varying resonant dielectric antenna array may again offer an alternative by greatly reducing the non-radiative (material) loss. Closely related to this concept are high-contrast gratings (HCGs) and artificial dielectrics. In HCGs, Mie resonances are used to control the phase of transmitted or reflected light at a surface. HCGs have been used to achieve surfaces with near-unity reflection for applications such as mirrors in vertical-cavity surface-emitting lasers[86], quarter waveplates[87], and optical elements with spatial phase variation such as lenses[88], [89] and spiral phase plates[90]. However, one of the drawbacks of this approach is that it is difficult to achieve full 2π phase control while preserving near-unity

reflectance with a single layer grating, an issue that becomes more restrictive as the index of the resonator is reduced. In artificial dielectrics[91]–[93], high index dielectric structures are patterned with deep sub-wavelength spacing to achieve a gradient index surface along the surface. High diffraction efficiency can be realized with such surfaces, however, due to the lack of strong resonances and thus low index contrast, the thickness of the surface must be greater than the free-space wavelength to acquire a 0 to 2π phase shift. This results in the need to fabricate structures with relatively high aspect ratios which can be challenging.

In this chapter, we demonstrate a broadband dielectric meta-reflectarray linear polarization convertor by utilizing structured silicon (Si) cut-wire resonators placed above a silver ground plane. The meta-reflectarray utilizes Mie resonances in the Si resonators and multiple reflections from the silver mirror. The multiple reflections relax the required phase delay upon a single pass through the resonator layer, mitigating the tradeoff between phase control and efficiency present in single layer HCGs. This allows the meta-reflectarray to serve as a half-waveplate with near-unity reflectance and over 98% polarization conversion efficiency across a 200 nm bandwidth. Furthermore, by varying the resonator dimensions, broadband 2π phase control of the reflected cross-polarized light can be achieved while maintaining high conversion efficiency, opening the door to ultra-compact lenses and phase plates at optical wavelengths.

3.2 Broadband Linear Polarization Conversion

A schematic of the polarization converter is illustrated in Fig. 3.1(a). It is composed of an array of Si cut-wires and a silver ground plane, with a low index PMMA

spacer in between. Device fabrication began with depositing a 380-nm-thick amorphous Si (n=3.7) thin film on quartz. The cut-wires were then created using electron beam lithography and reactive-ion etching. PMMA (n=1.48) was then spin-coated onto the sample and planarized to serve as the low index dielectric spacer and a silver film was deposited on top, serving as the reflective mirror. The SEM image of the fabricated sample is shown in Fig. 3.1(b).
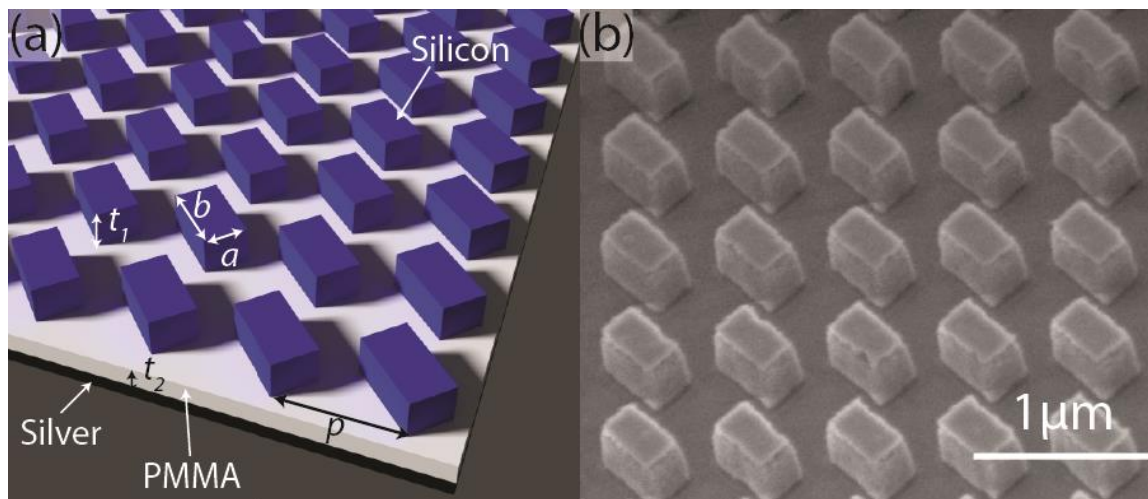
Figure 3.1. (a) Schematic of the meta-reflectarray with a unit cell period of p = 650 nm, a = 250 nm, b= 500 nm, t1 = 380 nm and t2 = 200 nm. In the fabricated sample the resonators are embedded in PMMA and a quartz wafer caps the resonators. (b) SEM image of the sample before spin-coating PMMA and depositing the silver film.
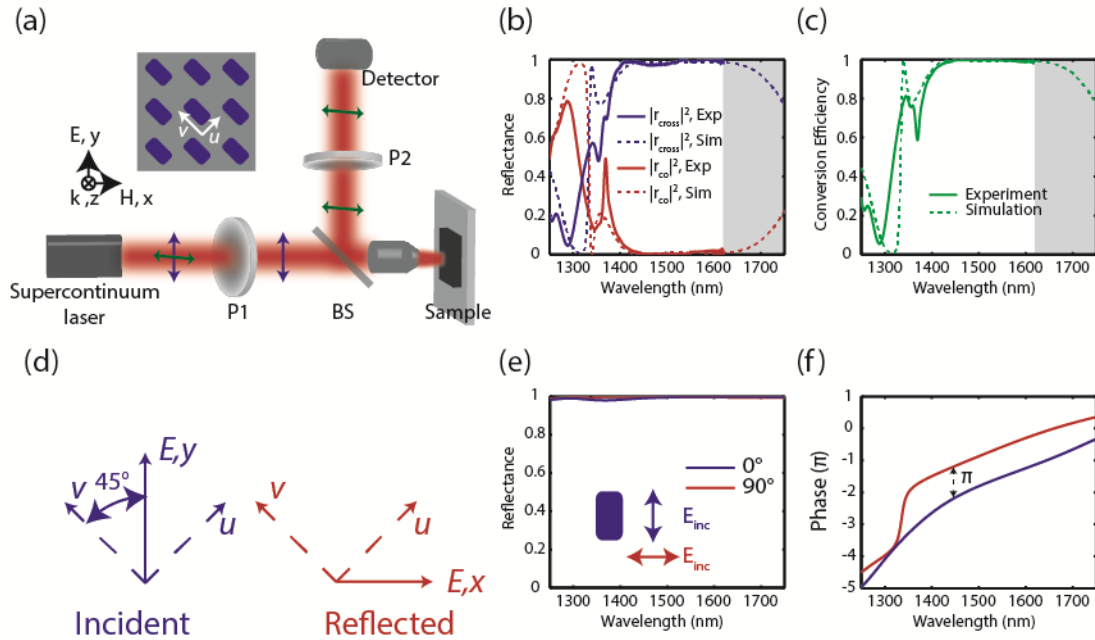
Figure 3.2. (a) Schematic of the polarization conversion measurement set-up. (b) Measured and simulated reflectance for co- and cross-polarized light. (c) Polarization conversion efficiency of the device. The shaded regions indicate the wavelength range where experimental measurements were not possible due to low detector quantum efficiency (d) Schematic of the decomposition of linearly polarized incident and reflected light. (e)-f) Reflectance and phase for x and y polarized light demonstrating near-unity reflection and a broadband π phase shift.

To experimentally characterize the performance of the polarization converter, we used a supercontinuum light source (Fianium SC400), incident normal to the sample surface with the polarization along the *x*-axis, which is tilted 45° with respect to the Si cut-wire axis. Two linear polarizers were employed in front and after the sample to measure the reflectance of the same polarization state as that of the incident wave, $|r_{co}|^2$, and that of the perpendicular polarization $|r_{cross}|^2$, as illustrated in Fig. 3.2(a). All reflectance measurements were normalized to the reflectance measured from a silver mirror. Figure 3.2(b) shows the measured reflectance for both polarizations and the

40

corresponding polarization conversion rate (PCR), defined as $\left.|r_{cross}|^2\middle/\left(|r_{cross}|^2+|r_{co}|^2\right)\right.$, is shown in Fig. 3.2(c). The experimental measurements demonstration that the PCR remains above 98% from 1420 nm to 1620 nm, and the cross-polarized reflection remains above 97% over this bandwidth, in good agreement with the simulation. Measurements beyond 1620 nm were not possible (shaded region in Figs 3.2b-c) due to the low quantum efficiency of the spectrometer's indium gallium arsenide detector and reduced light source intensity at long wavelengths. However, the numerical simulation predicts that 90% PCR extends out to 1720 nm and given the good agreement with theory, we expect the experimentally achievable efficiency to also be preserved over this range.

To better understand the response of the meta-reflectarray, the incident light, which is linearly polarized along the x-direction, can be decomposed into two perpendicular components, u and v which correspond the short and long axis of the resonator, respectively (Fig. 3.2d). The numerically simulated reflection amplitude and phase for a resonator array illuminated with polarization along these axes are shown in Figs. 3.2(e),(f). It can be observed that the reflection amplitudes in both polarizations are close to unity while the relative phase retardation is roughly π throughout the wavelength range where the linear polarization conversion occurs, leading to a 90° polarization rotation when light is incident with polarization along the x or y-axis of the sample.

The high conversion efficiency can also be understood by modeling the field evolution upon multiple reflections within the low-index spacer layer, resulting in constructive and destructive interference of the cross and co-polarized light, respectively[73], as is shown in Fig. 3.3.
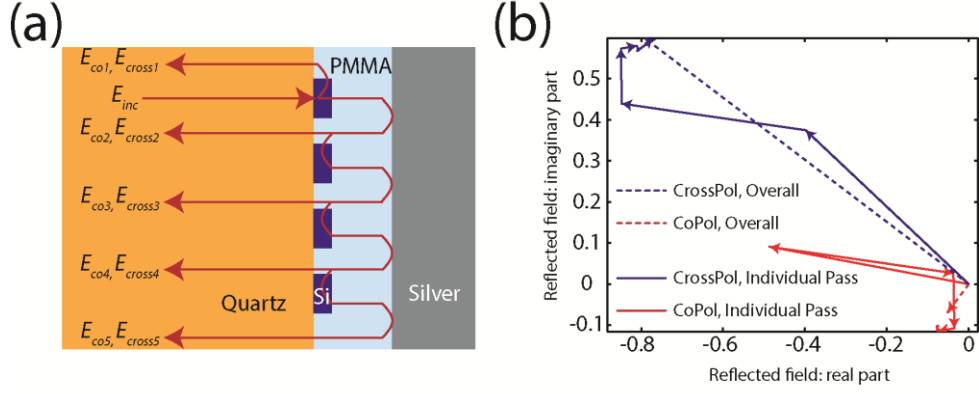
Figure 3.3. (a) Schematic of the multiple reflections. (b) Comparison between the calculated reflected field from multiple reflections and the simulated overall reflected field.

In this model, the resonator array, the PMMA spacer, and the metal ground plane are each treated as an individual layer. For the resonator layer, light incident onto the top surface can couple into the resonators and then radiate back to the environment with the amplitude and phase being modified differently for co- and cross-polarized fields. The layer of resonators can then be regarded as an effective layer and the light being re-radiated can be treated as being reflected or transmitted. The complex reflectivity and transmissivity from the resonator layer is obtained from FEFD simulations from an array of resonators embedded in PMMA without the metal ground plane. The reflectivity and transmissivity are expressed as r_r and t_ρ where $\rho=0$ for co-polarized fields and $\rho = 1$ for cross-polarized fields. Based on the multiple reflection model, the reflected field, $\vec{E}_{\rho',j}$ (j represents the jth pass), from each individual pass is given by

$$\vec{E}_{\rho',j=1} = \vec{E}_{inc}\, r_{\rho=\rho'}$$

$$\vec{E}_{\rho'=0,j=2} = \vec{E}_{inc}\,(t_0^2 + t_1^2)\exp(i2k_0 n_0 d)\,r_m$$

$$\vec{E}_{\rho'=1,j=2} = \vec{E}_{inc}\, t_1 t_0 \exp(i2k_0 n_0 d)\,r_m$$

$$\vec{E}_{\rho'=0,j,(j\geq3)} = \vec{E}_{inc}\Big(t_0^2 \sum_{\substack{l=0 \\ (l=even)}}^{j-2} C_{j-2}^l r_0^{j-2-l} r_1^l + t_1^2 \sum_{\substack{l=0 \\ (l=even)}}^{j-2} C_{j-2}^l r_0^{j-2-l} r_1^l + t_1 t_0 \sum_{\substack{l=1 \\ (l=odd)}}^{j-2} C_{j-2}^l r_0^{j-2-l} r_1^l \Big)\exp(i2k_0 n_0 d)\,r_m^{j-1}$$

$$\vec{E}_{\rho'=1,j,(j\geq3)} = \vec{E}_{inc}\Big(t_0^2 \sum_{\substack{l=1 \\ (l=odd)}}^{j-2} C_{j-2}^l r_0^{j-2-l} r_1^l + t_1^2 \sum_{\substack{l=1 \\ (l=odd)}}^{j-2} C_{j-2}^l r_0^{j-2-l} r_1^l + t_1 t_0 \sum_{\substack{l=0 \\ (l=even)}}^{j-2} C_{j-2}^l r_0^{j-2-l} r_1^l \Big)\exp(i2k_0 n_0 d)\,r_m^{j-1}$$

$$(3.1)$$

where $\vec{E}_{inc}$ is the incident electric field, k_0 is the free space wave number, n_0 is the refractive index of PMMA, d is the spacer thickness, l is an integer number smaller than $(j-2)$ and represents the number of times that the polarization is rotated upon reflection at the bottom surface of resonator layer in the jth pass. As a field being cross-polarized twice will return to a co-polarized field, the requirement for the jth path, $\vec{E}_{\rho',j}$ to be co-polarized is that $\rho=1$ appears an even number of times in the equations. The same is true for cross-polarized field where $\rho=1$ can only appear an odd number of times. The overall reflection for both co- and cross-polarization is the sum of individual passes $\vec{E}_{\rho'} = \sum_{j} \vec{E}_{\rho',j}$.

The simulated overall reflected field and the calculated sum of the reflected field of each pass are plotted in Figure B.3(b). The result from the FEFD simulation and the calculation shows good agreement in both co- and cross-polarization, which corroborates the theory.

3.3 Broadband Optical Vortex Generation

More interestingly, by properly engineering the cut-wire geometry, a 0 to 2π phase shift can be achieved for the cross-polarized reflected light with near-unity efficiency.

This is in contrast to plasmonic V-shaped antenna based metasurfaces, where the majority of scattered light remains in the ordinary component (co-polarized), resulting in low signal-to-noise ratio (SNR)[23]. The 2-dimensional colormap of the numerically simulated reflectance, $|r_{cross}|^2$, and phase, φ_{cross}, of the meta-reflectarray with varying Si cut-wire dimensions at a fixed wavelength of 1550 nm, are plotted in Figs. 3.4(a),(b). These simulations were performed using a finite-element frequency-domain solver (CST Microwave Studio) with periodic boundary conditions. It can be observed that there is a region of high reflectance in which four antenna dimensions were chosen (circles in Fig. 3.4a,b) to provide an incremental phase shift of $\pi/4$ for cross-polarized reflected light. By simply rotating the structures by 90°, the additional π phase shift can be attained for realizing full 2π coverage while maintaining near-unity efficiency.

An additional feature of this reflectarray is that it can maintain high efficiency over a wavelength range of ~100 nm within the telecommunications band as demonstrated by the simulated reflection amplitude and phase for the eight resonators as a function of the incident wavelength between 1500 nm and 1600 nm (Fig. 3.4d-e). Within this range, the cross-polarized reflectance remains above 75% with the greatest drop occurring for resonators 1 and 5 at long wavelengths. However, despite this drop, the average reflectance is 93.6% across this bandwidth. The phase gradient is calculated by taking resonator 1 as a reference at each wavelength and setting its phase advance to zero. Across the l00 nm bandwidth it can be seen that the phase gradient across the resonators remains linear, ensuring the designed phase profile is maintained.
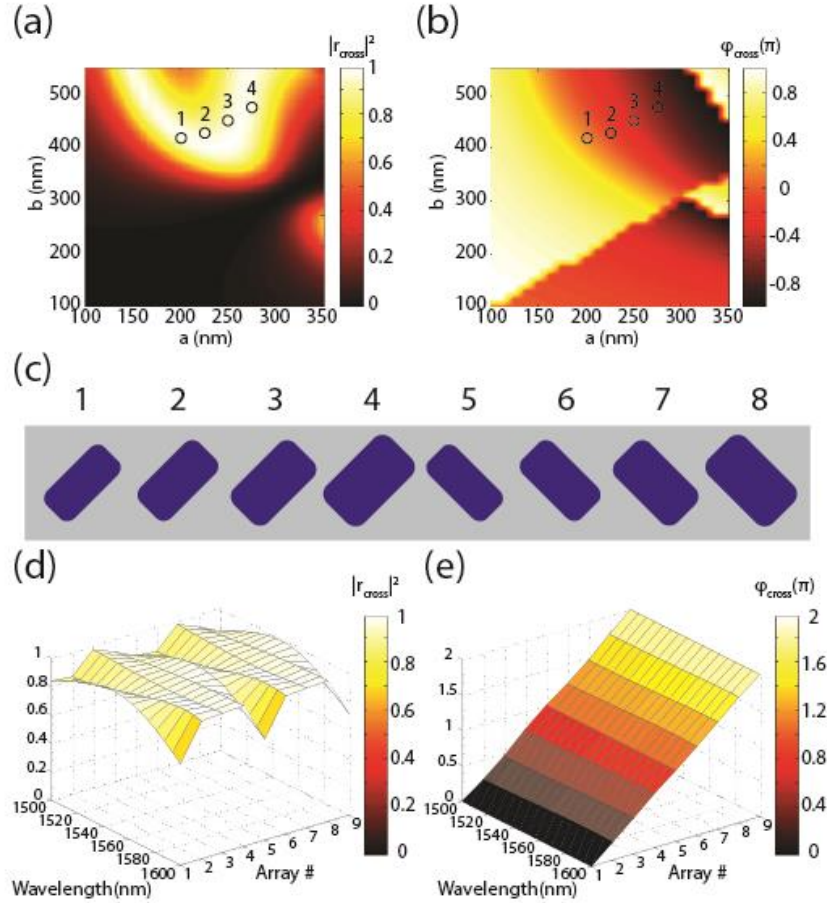
Figure 3.4. Simulated cross-polarized reflection (a) magnitude and (b) phase for resonators with varying geometry at a fixed wavelength of 1550 nm. The unit cell period is set as 650 nm and the PMMA spacer thickness is set to 150 nm. (c) Schematic of eight resonators that provide a phase shift from 0 to 2π. The dimension of resonators 1-4 are 1) a=200nm, b=425nm; 2) a=225nm, b=435nm; 3) a=250nm, b=450nm; 4) a=275nm, b=475nm. Resonators 5-8 are simply rotated by 90° with respect to resonators 1-4. Simulated cross-polarized reflection (d) amplitude and (e) phase for arrays of resonators 1-8 as a function of the incident wavelength. The phase delay of array 1 is set to 0 for each wavelength to serve as a reference.

In order to validate the performance of a variable phase meta-reflectarray, we fabricated a sample with a spiral phase profile ranging from 0 to 2π with a phase increment of $\pi/4$ along the azimuthal direction (shown in Fig. 3.5a-b). The design is based on the 8 Si cut-wire resonators modeled in Fig. 3. This particular phase profile

leads to the generation of a Laguerre-Gaussian beam with a theoretical cross-polarized reflectance that is above 94.5% for each section of the reflectarray at the center wavelength of 1550 nm. The Laguerre-Gaussian beam has a helical wavefront with a phase singularity in the center characterized by an azimuthally dependent phase term, $\exp(il\phi)$, where l represents the topological charge, which was chosen as $l = 1$, and ϕ is the azimuthal angle[94]. This optical vortex beam carries orbital angular momentum, making it a platform for investigating fundamental physical phenomenon such as spin-orbit interaction in photonic systems[77], [78], and such beams have various applications in optomechanics[95] and information processing[96]–[99].

The evolution of the vortex beam as a function of incident wavelength was measured by illuminating the sample with a linearly polarized and collimated tunable continuous wave diode laser. A linear polarizer oriented 90° with respect to the illumination polarization was placed in front of the camera to filter out any co-polarized light. Images of the reflected cross-polarized beam are shown in Figs. 3.5(c)-(e) and have the characteristic intensity minimum at the center which is a direct consequence of self-cancel-out associated with the corkscrew shaped beam. The reflected beam was also measured using a Michelson interferometer with the generated vortex beam and the co-propagating Gaussian beam in the sample and reference arm, respectively. The dislocated fringe and spiral shape phase patterns are clearly observable when the two beams are tilted and collinear with respect to each other, respectively, as illustrated in Figs. 3.5(f)-(k). In order to qualitatively gauge the conversion efficiency of the meta-reflectarray, the linear polarizer place before the camera was removed, resulting in the images shown in Figs. 3.5(l)-(m). It can be observed the spiral patterns remain largely unaffected, though

there is moderate noise in the center of the pattern which is due to the imperfections in

the cut-wire arrays leading to increased co-polarized reflection.
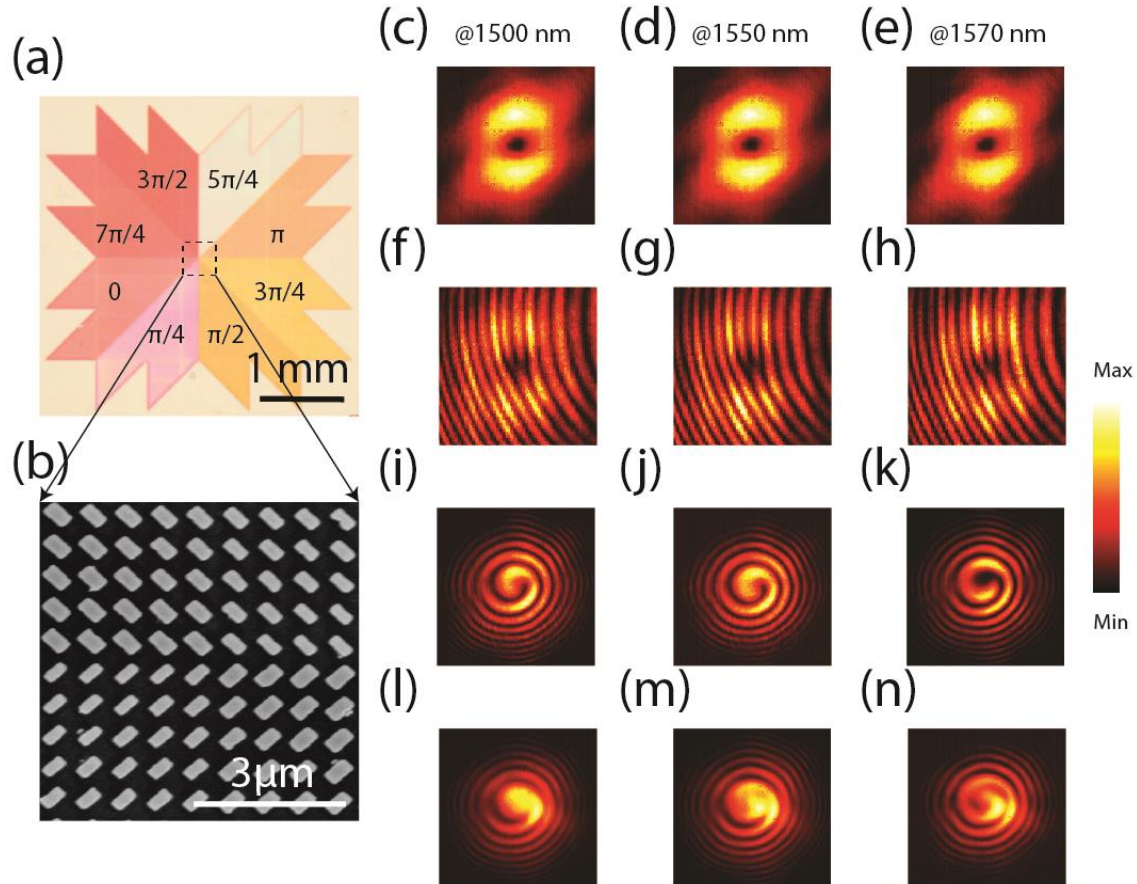
Figure 3.5. (a) Optical microscope image of the fabricated spiral phase plate composed of eight sections of Si cut-wires, providing an incremental phase shift of $\pi/4$. (b) SEM image showing the cut-wires at the center of the reflectarray. (c-e) Experimentally measured intensity profiles of the generated vortex beam with topological charge l=1. The wavelengths of incident light are (c) 1500 nm, (d) 1550 nm, and (e) 1570 nm. (f-h) Interference pattern of the vortex beam and the co-propagating Gaussian beam when the beam axes are tilted with respect to one another. (i-k) Interference pattern of a vortex beam and a Gaussian beam which have collinear propagation. In (c-k) a linear polarizer is placed in front of the camera to filter out co-polarized light. (l-m) Interference pattern of the vortex beam and the Gaussian beam in the absence of the linear polarizer.

Lastly, one important aspect that remains to be explored is the role of coupling

between the resonators in the array. This has important ramifications for using this type of meta-reflectarray for realizing short focal length lenses, in which dissimilar resonators are placed adjacent to one another. To explore the role of coupling, we modeled a surface in which the 8 resonators from Fig. 3.4, each with a unit cell size of 650 nm x 650 nm, were placed adjacent to one another forming a linear phase gradient over a supercell with length S = 5.2 μm. Based on the generalized Snell's law[23], the surface should exhibit an anomalous reflection peak at an angle of $\theta_r = \sin^{-1}[(\lambda_0/nS) + \sin(\theta_i)]$, where n is the background index, equal to the index of quartz / PMMA (n = 1.5) in our case, and θ_i is the incident angle. Numerical simulations were performed to verify the meta-reflectarray performance by illuminating the array at normal incidence (θ_i = 0°) with a Gaussian beam with a waist size of 7 μm and wavelength of 1550 nm. The cross-polarized reflected field is plotted in Fig. 3.6(a) and demonstrates a well-defined phase front while the far-field scattered intensity was collected for both co- and cross-polarized reflection and is plotted as a function of scattered angle in Fig. 3.6(b). The peak cross-polarized scattering angle matches well with the theoretical angle of θ_r = 11.5° (dashed line) and the diffraction efficiency of the +1 diffraction order is 83% with the major source of inefficiency arising from light remaining in the 0th order co-polarized beam. The slight reduction in conversion efficiency, compared to the spatially homogenous arrays, indicates that coupling between resonators plays a role in the response and must be taken into account when designing sharp phase gradients, for applications such as lensing, when dissimilar resonators are placed next to each another.
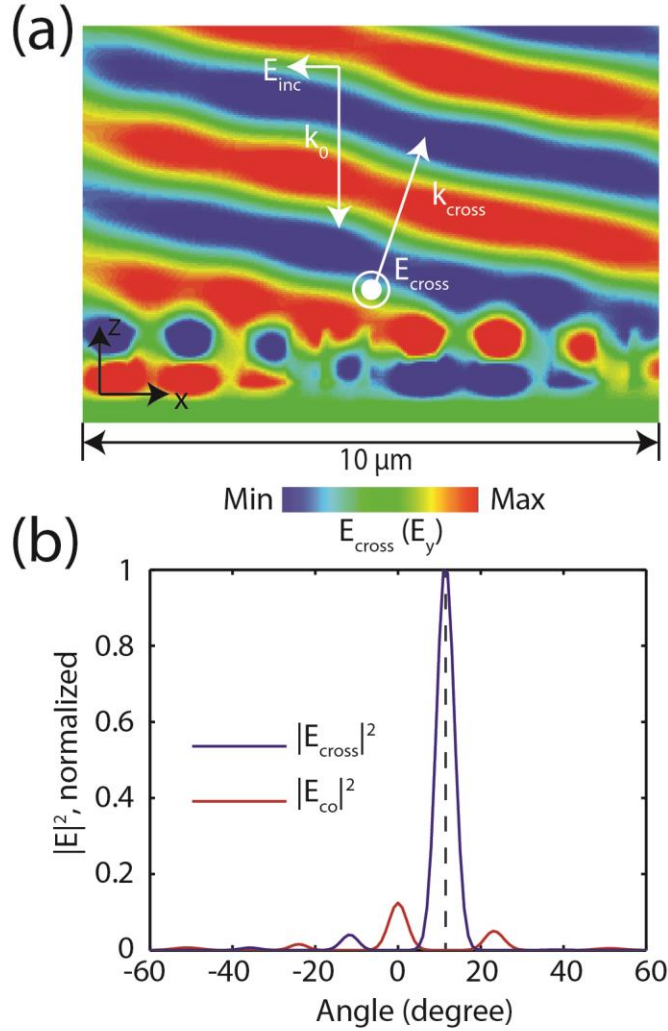
Figure 3.6. (a) Electric field plot of the meta-reflectarray illumined with a normally incident x-polarized Gaussian beam with a wavelength of 1550 nm and waist of 7 μm. The metasurface is composed of the 8 Si cut-wire resonators from Fig. 3 with a unit cell period of 650 nm. (b) Far-field scattered light as a function of angle for both co- and cross-polarizations. The dotted line corresponds to the solution of the generalize Snell's law and matches well with the full-wave simulation.

3.4 Conclusions

To summarize chapter 3, we have experimentally demonstrated broadband linear polarization conversion and optical vortex beam generator by employing a meta-reflectarray based on dielectric antennae. Replacing plasmonic antennae with their dielectric counterparts allows loss to be reduced and bandwidth to be increased due to

lower dispersion. The tradeoff is that dielectric based metasurfaces will invariably have a slightly larger unit cell size at optical frequencies due to the lack of high index materials which will limit applications requiring off-normal incidence or large in-plane wavevector. However, as shown here, this is not a significant limitation for polarization control or in realizing reflective phase plates for complex beam formation and lensing.

Chapter 4 2D Dielectric Metasurface — Analogue of Electromagnetically Induced Transparency

4.1 Introduction

In addition to controlling the wavefront of light, 2D dielectric metasurfaces can also be used to dramatically modify the far-field spectroscopic features of light. One possibility is to use the dielectric metasurface to mimic electromagnetically induced transparency (EIT), creating ultra-sharp resonances in its transmission spectrum for application such as bio-sensing and active light modulation.

EIT is a concept originally observed in atomic physics and arises due to quantum interference resulting in a narrowband transparency window for light propagating through an originally opaque medium[100]. This concept was later extended to classical optical systems using plasmonic metamaterials[101]–[109], among others[110], [111], allowing experimental implementation with incoherent light and operation at room temperature. The transparent and highly dispersive nature of EIT offers a potential solution to the long-standing issue of loss in metamaterials as well as the creation of ultra-high quality factor (Q-factor) resonances, which are critical for realizing low-loss slow light devices[101], [109], [112], [113], optical sensors[114], [115] and enhancing nonlinear interactions[116].

The classical analogue of EIT in plasmonic metamaterials relies on a Fano-type interference[117], [118] between a broadband "bright" mode resonator, that is accessible from free space, and a narrowband "dark" mode resonator which is less-accessible, or inaccessible, from free-space. If these two resonances are brought in close proximity in

both the spatial and frequency domains, they can interfere resulting in an extremely narrow reflection or transmission window. Due to the low radiative loss of the dark mode, the Fano resonance can be extremely sharp, resulting in complete transmission, analogous to EIT[101], [103], [108], [109], [112], [113], [119]–[121], or complete reflection[114], from the sample across a very narrow bandwidth. However, the main limitation of metal-based Fano-resonant systems is the large non-radiative loss due to Drude damping, which limits the achievable Q-factor[118] to less than ~10.

High-refractive-index dielectric particles offer a potential solution to the issue of material (non-radiative) loss. For instance, dielectric Fano-resonant structures based on oligomer antennae[46], silicon nanostripe[123], and asymmetric cut-wire metamaterials[124], [125] have been demonstrated with Q-factors up to 127.

In this chapter, we describe the development of silicon (Si)-based metasurfaces possessing sharp EIT-like resonances with a record high Q-factor of 483 in the near-infrared regime. The high-Q resonance is accomplished by employing Fano-resonant unit cells in which both radiative and non-radiative damping are minimized through coherent interaction among the resonators combined with the reduction of absorption loss. Combining the narrow resonance linewidth with strong near-field confinement, we demonstrate an optical refractive index sensor with a figure of merit (*FOM)* of 103. In addition, we demonstrate unit cell designs consisting of double-gap split-ring resonators that possess narrow feed-gaps in which the electric field can be further enhanced in the surrounding medium, allowing interaction with emitters such as quantum dots.

52

4.2 Design and Characterization

The schematic of the designed dielectric metasurface is shown in Fig. 4.1(a). The structure is formed from a periodic lattice made of a rectangular bar resonator and a ring resonator, both formed from Si. The rectangular bar resonator serves as an electric dipole antenna which couples strongly to free space excitation with the incident E-field oriented along the x-axis. The collective oscillations of the bar resonators form the "bright" mode resonance. The ring supports a magnetic dipole mode wherein the electric field is directed along the azimuthal direction, rotating around the ring's axis. The magnetic dipole mode in the ring cannot be directly excited by light at normal incidence as the magnetic arm of the incident wave is perpendicular to the dipole axis; however, it can couple to the bright mode bar resonator. Furthermore, the ring resonators interact through near-field coupling, resulting in collective oscillation of the resonators and suppression of radiative loss, forming the "dark" mode of the system. The interference between the collective bright and dark modes form a typical 3-level Fano-resonant system[118], as illustrated in Fig. 4.1(b). The response of the dielectric metasurface is similar to the collective modes found in asymmetric double-gap split-ring resonators in which the asymmetry in the rings yields a finite electric dipole moment that can couple the out-of-plane magnetic dipole mode to free space[126]–[131]. In our case, coupling to free space is provided by the bright mode resonators which are placed in close proximity to the symmetric dark mode resonators. Numerical simulations of the structure were carried out using a commercially-available software (CST Microwave Studio) using the finite-element frequency-domain (FEFD) solver. The simulated transmittance, reflectance and absorption spectra of the designed structure are shown in Fig. 4.1(c), where a distinct EIT-like peak can be observed at a

wavelength of 1376 nm. In these simulations the resonators are sitting on a quartz substrate and embedded in a medium with a refractive index of $n = 1.44$, matching the experiments described below. We have also used the dielectric function of Si as determined using ellipsometry and assumed an infinitely large array, resulting in a Q-factor that reaches 1176, roughly 2 orders of magnitude higher than any previously reported Fano-resonant plasmonic metamaterial[118]. Furthermore, the peak of the transparency window approaches unity, demonstrating the potential to realize highly dispersive, yet lossless, "slow light" devices.

Figure 4.1. (a) Diagram of the metasurface. The geometrical parameters are: = 150 nm, = 720 nm, = 110 nm, = 225 nm, = 70 nm, = 80 nm, = 110nm,   = 750 nm and = 750 nm. (b) Schematic of interference between the bright and dark mode resonators. (c) Simulated transmittance (blue curve), reflectance (red curve), and absorption (green curve) spectra of the metasurface. (d) Oblique scanning electron microscope image of the fabricated metasurface. (e) Enlarged image of a single unit cell. (f) Experimentally measured transmittance, reflectance, and absorption spectra of the metasurface.

The designed structure was fabricated by starting with a 110-nm-thick poly-crystalline Si (refractive index $n = 3.7$) thin film deposited on a quartz (SiO_2) ($n = 1.48$) wafer. The structure was patterned using electron beam lithography for mask formation followed by reactive-ion etching. A SEM image of a fabricated sample is shown in Fig. 4.1(d),(e). Before optical measurements, the resonator array was immersed in a refractive index matching oil ($n = 1.44$) within a polydimethylsiloxane (PDMS) flow cell. (See Methods for details). The experimentally measured transmittance, reflectance and absorption spectra, plotted in Fig. 4.1(f), were acquired by illuminating the sample with normal-incident white light with the electric field oriented along the long axis of the bar resonator. A peak transmittance of 82% was observed at a wavelength of 1371 nm with a Q-factor of 483, as determined by fitting the dark mode resonance to a Fano line shape (see Appendix C1 for details). The shape of the measured spectra have good agreement with the simulation, though the Q-factor and peak transmittance are reduced. This is most likely due to imperfections within the fabricated sample which introduce scattering loss and break coherence among the resonators. The role of coherence will be further addressed below. Furthermore, additional loss in the Si arising from surface states created during reactive ion etching leads to slightly increased absorption in the array compared to theory. Nonetheless, this structure has the highest experimentally achieved Q-factor among all plasmonic or dielectric optical metamaterials/metasurfaces reported to date. It should also be noted that the use of index-matching oil is not needed to achieve such high Q-factors.

4.3 Theoretical Treatment

The response of the metasurface can be qualitatively understood by applying the widely used coupled harmonic oscillator model[132], [133], described by the following equations,

$$\dot{x}_1 - j\left(\omega_0 + j\gamma_1\right)x_1 + j\kappa x_2 = gE_0 e^{j\omega t},$$
$$\dot{x}_2 - j\left(\omega_0 + \delta + j\gamma_2\right)x_2 + j\kappa x_1 = 0,$$

(4.1)

where x_1 and x_2 represent the amplitude of the collective modes supported by oscillators 1 (bright mode) and 2 (dark mode), respectively. γ_1 and γ_2 are the damping rates, given by $\gamma = \gamma_R + \gamma_{NR}$ where γ_R and γ_{NR} are the radiative and non-radiative decay rates, respectively. ω_0 is the central resonant frequency of oscillator 1, δ is the detuning of resonance frequency of oscillator 1 and 2, and g is the bright mode dipole coupling strength to the incident electric field E_0. κ is the coupling coefficient between oscillators 1 and 2 and given the close proximity of the resonators, it should be considered an effective coupling coefficient that takes into account interaction between the bright mode atom and its 2 nearest neighbors.

Of particular interest is the value of γ_2 which reflects the damping of the collective dark mode and plays a large role in dictating the linewidth of the EIT-like resonance. The radiative damping term, γ_{R2}, is minimized due to the collective oscillations of the array, mediated by near-field coupling between the unit cells. One consequence of utilizing collective modes is that the value of γ_{R2} is inversely proportional to the size of the array due to the fact that the discontinuity at the edges of the array allows for light leakage to free space[134], [135]. While collective modes have

been utilized in past demonstrations of plasmonic EIT metamaterials to realize extremely small γ_{R2} values, the Q-factors have intrinsically been limited by the Ohmic loss in the metal. By replacing the resonator constituents with lossless dielectrics, the non-radiative damping term γ_{NR2} can also be minimized, resulting in the large increase in the Q-factor and peak transmittance.

Equally important is the role of the coupling coefficient, κ, in realizing a high Q-factor resonance for this system. It has previously been shown that the slope of dispersion is inversely proportional to κ^2. In the limit of $\gamma_2 \rightarrow 0$, reduction of κ will result in a monotonic increase of the Q-factor until $\kappa = 0$ is reached, at which point the Fano resonance will vanish, leaving only the bright mode resonance. In our system, the magnetic field from the bright mode resonator is inducing the dark mode resonance, as illustrated in Fig. 4.2(a). Thus, as the spacing between the resonators (g_1) is increased the coupling coefficient decreases, resulting in an increase in the Q-factor (Fig. 4.2c,d) and strong magnetic and electric field localization (Fig. 4.2b). At a spacing of $g_1 = 74$ nm, the Q-factor reaches a value of ~30,000 which is indicative of the fact that both radiative and non-radiative losses in the system are minimal, resulting in a situation wherein $\gamma_2 \sim 0$. However, losses in the Si primarily arising from surface states created during etching will ultimately limit the Q-factor, as has been demonstrated in microcavities[136]. Such losses are not included in these calculations. It is also important to realize that the bright mode resonator is also interacting with the dark mode resonator in the adjacent unit cell (D2), inducing a magnetic field that is 180° out of phase with the excitation from the bright mode resonator within its own unit cell. Therefore, when the gap between the bright

mode resonator and adjacent dark mode resonators are equal ($g_1 = 75$ nm, $\Delta = g_2 - g_1 = 0$) the fields destructively interfere and κ goes to zero, resulting in elimination of the Fano resonance, as can be observed in Fig. 4.2(b) and in the magnetic and electric field profiles in Fig. 4.2(b).
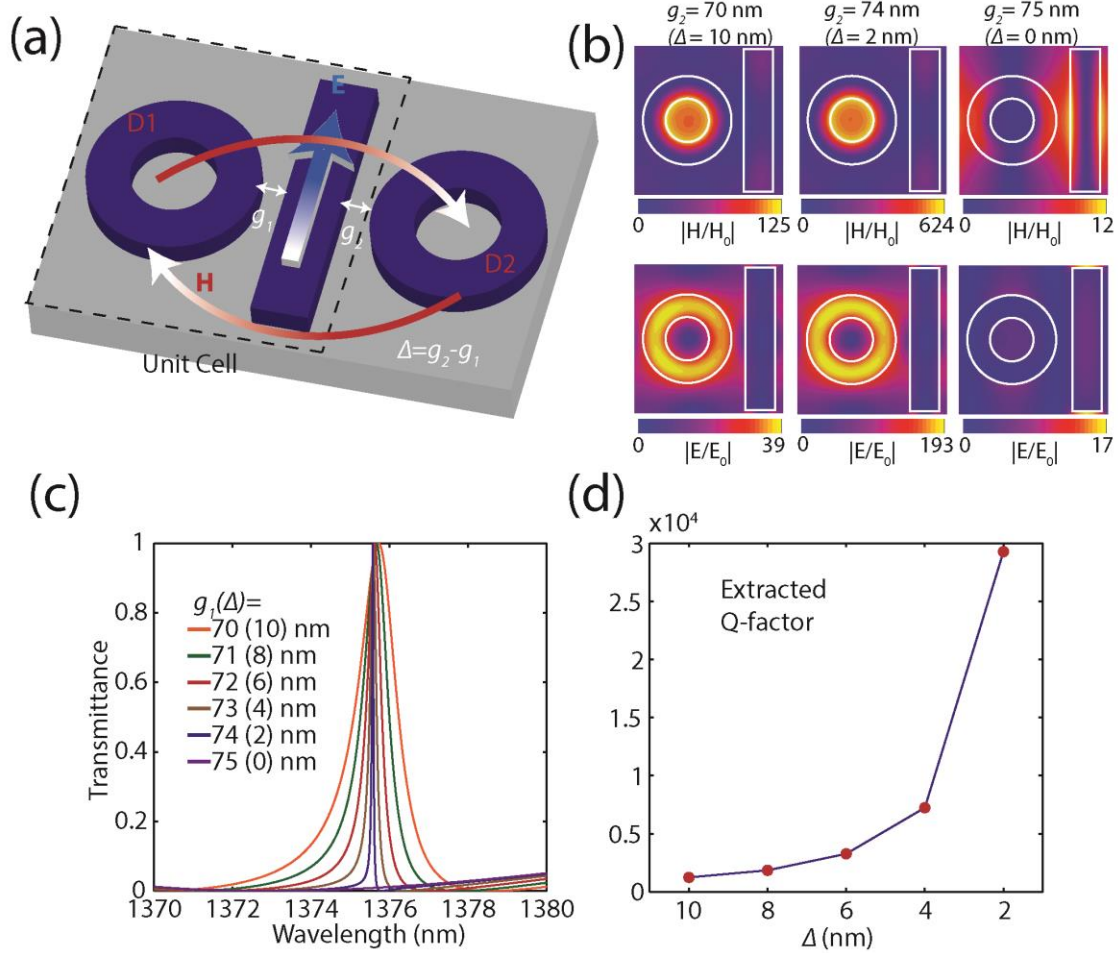
Figure 4.2. (a) Schematic showing the coupling of the bright mode resonator to the neighboring dark mode resonator. Here, we schematically provide the fields arising due to the bright mode resonance. (b) Simulated magnetic and electric field amplitudes as a function of resonator spacing. (c) Transmittance curve for the metasurface with varying values of g_1 obtained through FEFD simulation. $\Delta = g_2 - g_1$ is used to track the difference in spacing between the bright mode resonator and the adjacent dark mode resonators. (d) The extracted Q-factors of the EIT resonance as a function of Δ.
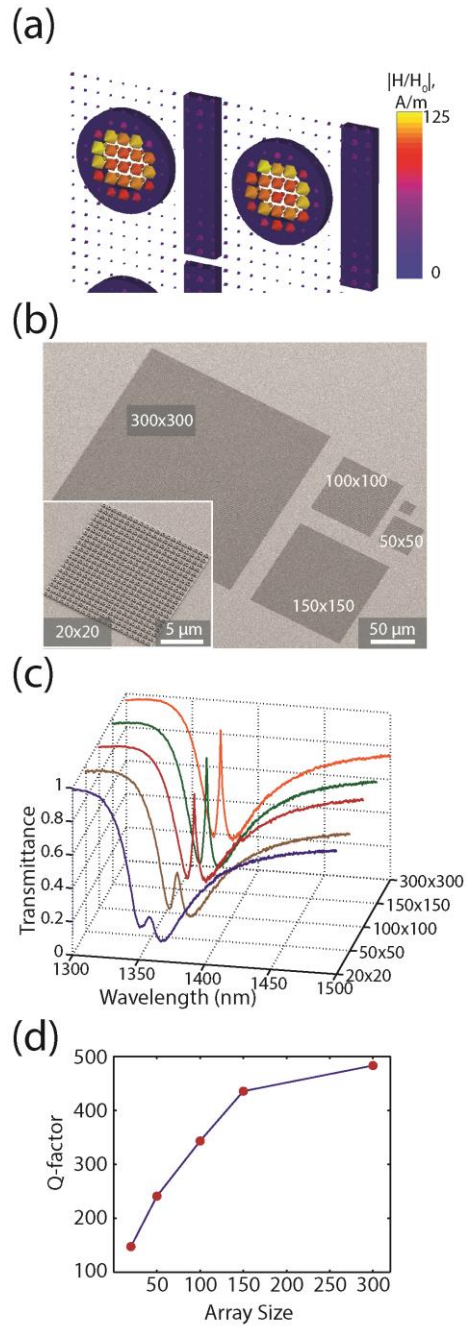
Figure 4.3. (a) Vector plot of the magnetic field showing the coherent excitation of the magnetic dipoles within the dark mode resonators. (b) Scanning electron microscope images of the dielectric metasurface with different array sizes. The inset shows the magnified view of a 20 by 20 array. (c) Transmittance spectra of arrays with different sizes. d, The extracted Q-factors of the metasurface as a function of array size.

At the transmission peak the energy in the array is concentrated in the collective dark mode with the magnetic dipoles in each of the split-rings oscillating coherently as shown in Fig. 4.3(a). The array size thus becomes an important factor in the overall Q-factor of the metasurface due to the fact that lattice perturbations at the array's edge break the coherence[134], [135], leading to strong scattering of light into free-space and broadening of the resonance peak. To characterize this effect, we fabricated arrays of five different sizes, consisting of 400 to 90,000 unit cells (SEM image of the test samples are shown in Fig. 4.3b). In the measurement, we used a 5x objective for illumination and a 50x objective for collection with an aperture in the conjugate image plane on the transmission side to confine the collection area to 15 μm x 15 μm. The measured spectra are shown in Fig. 4.3(c) and we observe that the Q-factor increases with increasing array size, saturating as we approach 90,000 unit cells. The saturation of the Q-factor indicates the limit imposed by both incoherent radiative loss arising from inhomogeneities and non-radiative loss arising due to finite absorption in the Si. As expected, the required unit cell number needed to achieve spectral convergence is larger than that reported in coherent plasmonic metamaterials due to the reduction in the non-radiative component.

Photonic crystal cavities possessing higher Q-factors have been reported[137], though they lack the spatial homogeneity present in the metasurface outlined here. Diffractive guided mode structures can also exhibit extremely high Q-factors[138], though in our case we have the additional freedom of engineering the local field enhancement through modification of the dark mode resonators. For instance, this can be done by placing symmetric feed-gaps in the resonator forming a double-gap split-ring, as shown in Fig. 4.4(a). In this case, the azimuthally oriented field located in the gap is

60

enhanced by a factor of $\varepsilon_d / \varepsilon_s$ (Fig. 4b), where ε_d and ε_s are the permittivities of the resonator and surrounding medium, respectively. For the design depicted in Fig. 4.4, this results in an electric field enhancement of 44 in the gap region. Having the advantages of both a sharp spectral response and a strongly enhanced field in the surrounding substance allows the metasurface to serve as an ideal platform for enhancing interaction with the surrounding medium. To investigate the response of such structures, samples were made using the same processes as described above and measured in $n = 1.44$ index matching oil. An SEM image of the sample is shown in Fig. 4.4(c). The simulated and experimentally measured transmittance curves are shown in Fig. 4.4(d) and result in theoretical and experimentally measured Q-factors of 374 and 129, respectively. The lower theoretical Q-factor, compared with the ring geometry, is due to the fact that the electric fields are not equal the two arms of the split-ring due to the asymmetry of the unit cell. This results in radiation loss to free space as the electric dipole moments do not fully cancel one another. The decrease in the experimental Q-factor, compared to theory, is attributed to more imperfections in the sample arising from the inclusion of the gaps, ultimately resulting in increased scattering from the structure.
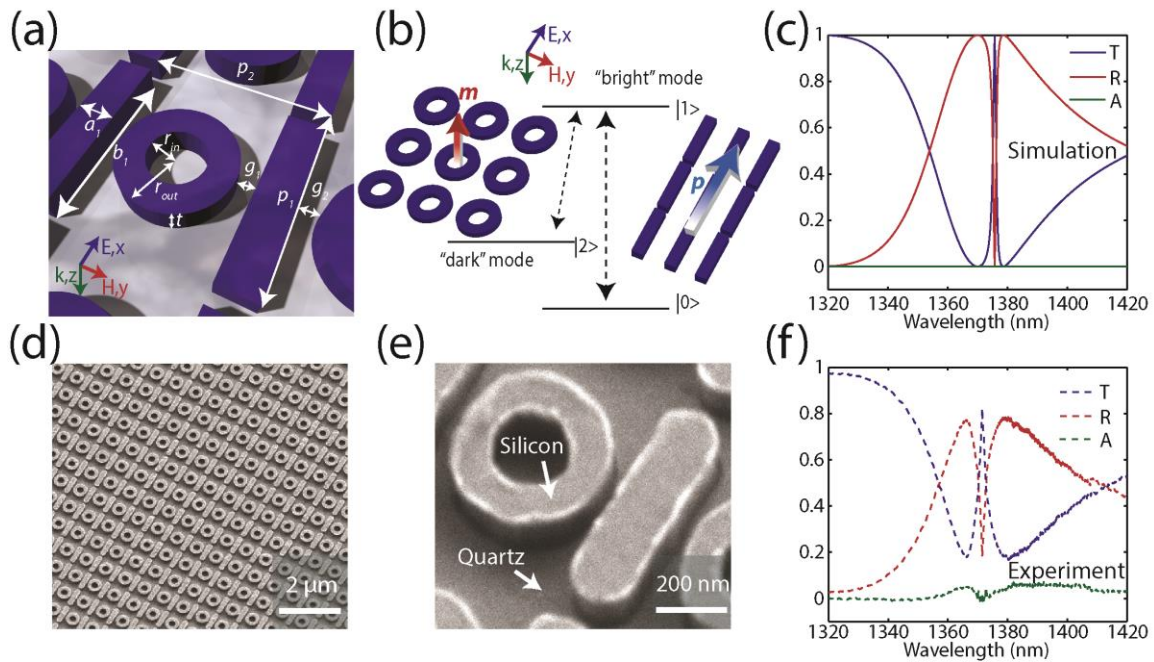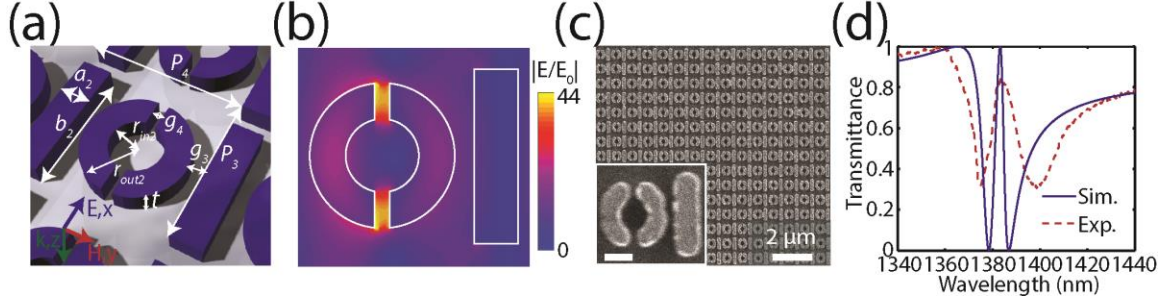
Figure 4.4. (a) Diagram of the metasurface. The geometrical parameters are: $a_2 = 150$ nm, $b_2 = 600$ nm, $r_{in2} = 120$ nm, $r_{out2} = 250$ nm, $g_3 = 70$ nm, $g_4 = 50$ nm, $t = 110$ nm, $p_3 = 750$ nm and $p_4 = 800$ nm. (b) Simulated electric field amplitude distribution. (c) Scanning electron microscope image of the fabricated metasurface. The inset shows a single unit cell (scale bar of 200 nm). (d) Simulated (blue solid line) and measured (red dashed line) transmittance spectrum of the metasurface.

4.4 Refractive Index Sensing

Due to their narrow linewidths, one interesting application of these metasurfaces is optical sensing. Optically resonant sensors are characterized by both the linewidth of the resonance ($\Delta\lambda$) as well as the shift in the resonance per refractive index unit change (S). These two values comprise the *FOM* which is given by $FOM = S/\Delta\lambda$ [139]. The highest demonstrated *FOMs* for Fano-resonant localized surface plasmon resonance (LSPR) sensors are on the order of 20[114], [140], [141]. Here, we examine the *FOM* of the ring resonator metasurfaces and to further increase the sensitivity of our metasurface to local index changes, we etched a 100-nm-tall quartz post below the Si resonators such that the field overlap in the surrounding dielectric can be further promoted, as illustrated in Fig. 4.5(a). The transmittance spectra of the metasurface when immersed in oil with different refractive indices, from 1.40 to 1.44, are presented in Fig. 4.5(b), and it can be seen that a substantial movement in the peak position is realized despite the small index change. A linear fit of the shift in the resonance peak (Fig. 4.5c) leads to a sensitivity of

$S = 289$ nm RIU^{-1}, which is comparable, but slightly lower, than the best Fano-resonant plasmonic sensors. The slight decrease in sensitivity is due to the fact that the index contrast, and corresponding field enhancement, at the dielectric metasurface-oil interface is still lower than that found in plasmonic structures. However, when combining the sensitivity with an average resonance peak linewidth $\Delta\lambda$ of only 2.8 nm, we arrive at an *FOM* of 103, which far exceeds the current record for Fano-resonant LSPR sensors. With further optimization of fabrication and more stringent control of the resonator coupling, *FOMs* on the order of 1000 should be within reach.
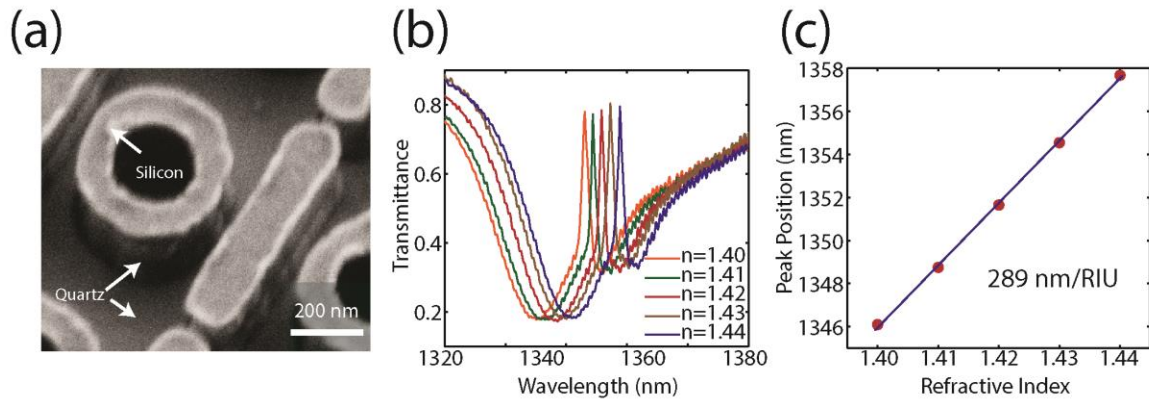
Figure 4.5. (a) SEM image of the sample with the quartz substrate etched by 100 nm. (b) Measured transmittance spectra of the EIT metasurface when immersed in oil with refractive index ranging from 1.40 to 1.44. (c) The red circles show the experimentally measured resonance peak position as a function of the background refractive index. The blue curve is a linear fit to the measured data, which was used to determine the sensitivity as 289 nm RIU^{-1}.

Furthermore, by introducing two feed-gaps in the dark mode ring resonator, we can greatly enhance the local electric field intensity in the vicinity of the resonator, and therefore increase the field overlap with the surrounding substance. Here, we also provide the performance of the double-gap split-ring metasurface as a sensor (Fig. 4.7). To further

increase the sensitivity of our metasurface to local index changes, we again etched a 100-nm-tall quartz post below the Si resonators, as illustrated in the SEM images in Figure 4.7(a). Compared with the ring-resonator metasurface, the double-gap split-ring sample shows a greater sensitivity to local refractive index change due to the increased modal overlap with the surrounding environment. By measuring the transmittance of the sample in different index matching liquids and extracting the shift of EIT resonance peak, we acquired a sensitivity S of 379 nm/RIU. However, when combining this with an average experimentally measured resonance linewidth of 10.3 nm, we arrived at a sensing FOM of 37, which is lower than the ring-resonator sample. The reason for the lower FOM is obviously the broader resonance linewidth. As we have also stated in the main text, the lower theoretical Q-factor, compared with the ring geometry, is due to the fact that the electric fields are not equal in the two arms of the split-ring due to the asymmetry of the unit cell. This results in radiation loss to free space as the electric dipole moments do not fully cancel one another. The decrease in the experimental Q-factor, compared to theory, is attributed to more imperfections in the sample arising from the inclusion of the gaps, resulting in increased scattering from the structure.
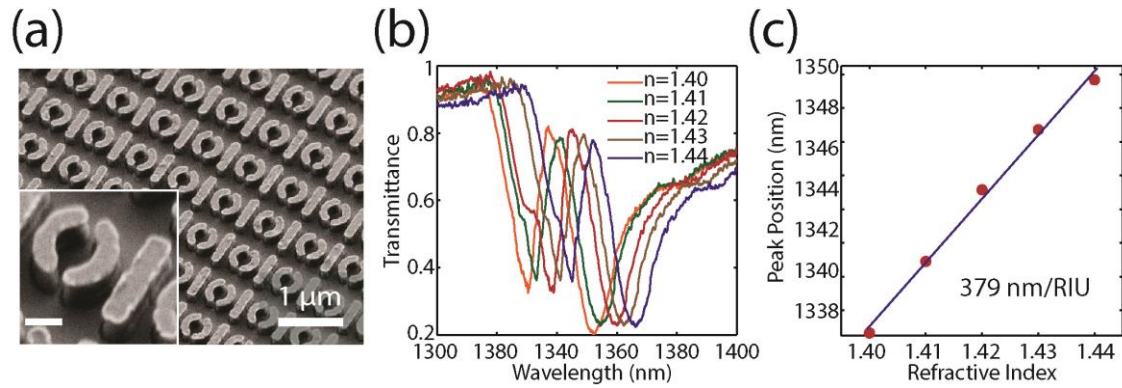
Figure 4.6. (a) SEM image of the double-gap split-ring sample with the quartz substrate etched by 100 nm. The inset is an enlarged image of a single unit cell (scale bar of 200 nm). (b) Measured transmittance spectra of the double-gap split-ring metasurface when immersed in oil with refractive index ranging from 1.40 to 1.44. (c) The red circles show the experimentally measured resonance peak position as a function of the background refractive index. The blue curve is a linear fit to the measured data, which was used to determine sensitivity of the structure as 379 nm/RIU.

4.5 Conclusion

In conclusion, dielectric metasurfaces can be used to significantly improve upon the performance of their plasmonic counterparts in mimicking electromagnetically induced transparency due to their greatly reduced absorption loss, resulting in sensing *FOMs* that far exceed previously demonstrated LSPR sensors. With proper design, such metasurfaces can also confine the optical field to nanoscale regions, opening the possibility of using such metasurfaces for a wide range of applications including bio/chemical sensing, enhancing emission rates, optical modulation, and low-loss slow light devices.

Chapter 5 2D Dielectric Metasurface — Enhanced Nonlinearity

5.1 Introduction

Following Chapter 4, we further investigate the nonlinear optical properties of the Fano-resonant Si metasurface. Nonlinear optics forms the basis for a number of useful processes including light generation in parametric up- and down-conversion tunable lasers[142], generation of entangled photons for quantum optics[150], and the nonlinear Kerr effect for ultrafast all-optical light modulation[33], [143], [144]. However, the nonlinear optical response of materials is intrinsically weak and thus a long interaction length and / or high intensity is needed for efficient nonlinear light interaction. When dealing with bulk crystals, the common method to boost nonlinear conversion is to employ phase-matching between the fundamental and generated waves[142]. However, phase matching still requires a relatively long sample interaction length which is problematic for compact integrated devices.

A different approach is to employ resonance-induced electromagnetic field enhancement. When employed in nanoscale films, this approach does not require phase matching and takes advantage of the fact that the *n*-th order harmonic generation is proportional to the integration of induced electric dipoles over the volume of a nanostructure unit cell,

$$\mathbf{p}^{(n)} \propto \int_V \chi^{(n)}(\mathbf{r}) \left[\mathbf{E}_{loc}(\mathbf{r},\omega) \right]^n dV \tag{5.1}$$

where $\chi^{(n)}$ is the intrinsic *n*-th order nonlinear susceptibility of the material, $\mathbf{E}_{loc}(\mathbf{r},\omega)$ is the local electric field, and V is the volume of a unit cell. As an example, localized

surface plasmon resonances can be utilized to substantially enhance the $\mathbf{E}_{\mathrm{loc}}(\mathbf{r},\omega)$ by efficiently funneling light from the far-field to a deep sub-wavelength scale. However, since the field maxima in plasmonic structures occurs at the boundary of the metal/dielectric interface, the intrinsic nonlinearity of the metal cannot be efficiently exploited. One way to mitigate this issue is to place nonlinear materials in the vicinity of the plasmonic "hot-spots"[32], [151], [152]; however, the small modal volume of plasmonic resonances will still limit the overall generation efficiency. Furthermore, plasmonic nanostructures generally suffer from a low damage threshold due to large optical absorption and the low melting temperature of metals compared to dielectrics. As an alternative, low-loss dielectric structures (silicon nanodisks[153], for example) exhibiting Mie resonances have recently been studied for enhancing third harmonic generation (THG); however, achieving intense near-field enhancements, and therefore high THG efficiencies, has remained challenging due to the leaky nature of the optical modes[83], [84], [154]. On-chip photonic structures such as ring-resonators and slow light waveguides have also been proposed for THG due to their ability to achieve large quality factors (Q-factor) and / or long photon residence times[155], [156]. However, the conversion efficiencies of such devices are limited due to two-photon absorption (TPA)[149] of the fundamental wave within silicon (Si), a result of the long optical path length of the bus waveguides.

In this chapter, we demonstrate a Fano-resonant[157], [158] Si-based metasurface possessing large third-order nonlinearity for use in THG. The enhanced nonlinearity is due to a high Q-factor Fano resonance that in turn strongly enhances the local electric field within Si, thus resulting in large effective $\chi^{(3)}$. Unlike ring resonators and other chip-

based devices, there is no bus waveguide and thus TPA is greatly reduced while the volumetric nature of the modes allows better overlap with the $\chi^{(3)}$ material compared to plasmonic implementations. This results in a metasurface with a THG enhancement of more than 5 orders of magnitude and a conversion efficiency of on the order of 10^{-6}, which is the highest value reported to date in micro or nanostructured films at comparable pump energies[145], [159]. Furthermore, by combining the nonlinear Kerr effect with the high Q-factor resonance, we experimentally demonstrate how the metasurface can be used for all-optical modulation.

5.2 Linear Optical Properties

The Fano-resonant metasurface is illustrated in Fig. 5.1(a),(b) and consists of a periodic lattice of coupled rectangular bar and disk resonators formed from Si. The rectangular bar resonator supports a "bright" electric dipole resonance that is excited when the incident electric field is along the *x*-axis. The disk supports a "dark" magnetic dipole resonance in which the electric field is directed along the azimuthal direction, rotating around the disk's axis. The out-of-plane magnetic dipole in the disk cannot be directly excited by normal incident light, but can instead be excited through near-field interaction with the bright mode bar resonator. The interference between the collective "bright" and "dark" modes forms a typical 3-level Fano-resonant system, as illustrated in Fig. 5.1(c). The geometry of the nonlinear Si-based Fano-resonant metasurface is similar to the linear one presented in Chapter 4. However, here we modified the "dark" mode resonator from a *ring-* to *disk*-shape to further promote light interaction with the nonlinear material (Si).

Polycrystalline silicon (Poly-Si) was chosen as the resonator material due to its large linear refractive index (n~3.7) and large intrinsic third-order susceptibility and nonlinear index ($\chi_{Si}^{(3)} \sim 2.0 \times 10^{-14}\,\mathrm{m^2 \cdot V^{-2}}$, $n_{2(Si)} \sim 2.7 \times 10^{-18}\,\mathrm{m^2 \cdot W^{-1}}$) in the near-infrared band[163]. In order to fabricate the structures, a 120 nm thick poly-Si layer was first deposited on a quartz substrate using low-pressure chemical vapor deposition (LPCVD). The resonators were then defined using electron beam lithography (EBL) followed by reactive-ion etching (RIE) (see Methods for further details). A scanning electron microscope (SEM) image of the fabricated sample is shown in Fig. 5.1(d). The experimentally measured transmittance, plotted in Fig. 5.1(e), was acquired by illuminating the sample with normal-incident white light with the electric field oriented along the long axis of the bar resonator. Numerical simulations of the structure were also carried out using a commercially-available software (CST Microwave Studio) using the finite-integration frequency-domain (FIFD) solver (see Methods for further details). A sharp peak in the transmittance curve is observed at a wavelength of 1348 nm with an experimental Q-factor of 466, as determined by fitting the dark mode resonance to a Fano line shape. The measured spectrum line-shape agrees well with the simulation, though the Q-factor and peak transmittance are reduced, which is expected due to imperfections with the fabricated sample and additional material loss in the Si arising from surface states created during RIE.
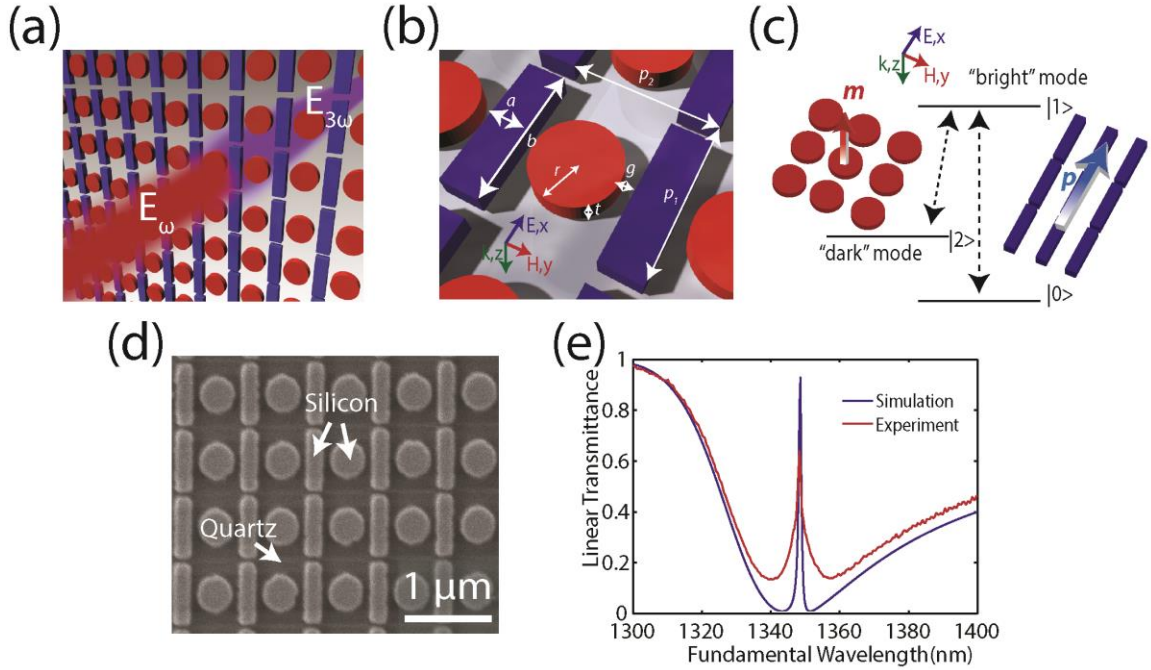
Figure 5.1. (a) Schematic of three photon up-conversion with the Fano-resonant silicon metasurface. The blue bar resonators represent the "bright" mode, and the red disk resonators represent the "dark" mode. (b) Diagram of one unit cell of the metasurface. The geometrical parameters are: a = 200 nm, b = 700 nm, r = 210 nm, g = 60 nm, t = 120nm, p_1 = 750 nm and p_2 = 750 nm. (c) Schematic of the Fano interference between the bright and dark mode resonators. (d) An SEM image of the fabricated metasurface. (e) Simulated (blue) and experimentally measured (red) transmittance spectra of the metasurface.

5.3 Enhanced Third Harmonic Generation and Nonlinear Kerr Effect

Accompanying the narrow transmittance curve, the metasurface also possesses a large electric field enhancement within the disk resonator, as shown in Fig. 5.2(a). The field enhancement is on the same order as state-of-the-art nonlinear plasmonic devices[32], [152]; however, in contrast to plasmonic structures, the field enhancement occurs within the volume of the dark mode resonator with excellent modal overlap with the $\chi^{(3)}$ material (Si). The metasurface possesses the advantages of waveguide-based devices such as a large Q-factor and good modal overlap with the active material while

70

greatly reducing parasitic losses such as TPA and direct THG absorption in the bus waveguides.

In order to quantitatively determine the nonlinear enhancement, we first compare the THG intensity from the metasurface with an un-patterned Si film with the same thickness. In the THG intensity measurement, we use an optical parametric oscillator (OPO) centered at 1350 nm as the pump, and focus the laser beam to a spot with an area of ~225 um^2 on the metasurface. The THG signal generated in the forward direction is then collected by a high numerical aperture objective and sent to a grating spectrometer with a liquid-nitrogen-cooled charge-coupled device (CCD) camera for spectroscopic analysis (see Appendix D1 for details of the measurement set-up). The THG spectra of the metasurface and un-patterned Si film are shown in Fig. 5.2b,c and demonstrate an enhancement factor of 1.5×10^5. Further verifying the origin of the enhancement, the metasurface shows no significant enhancement when illuminated with the electric field orthogonal to the bar resonator, as is shown in Fig. 5.2b. By comparing the third harmonic signal from a Si-on-quartz film and a bare quartz substrate (Fig. 5.2c), we further excluded the effect of THG from the quartz substrate.
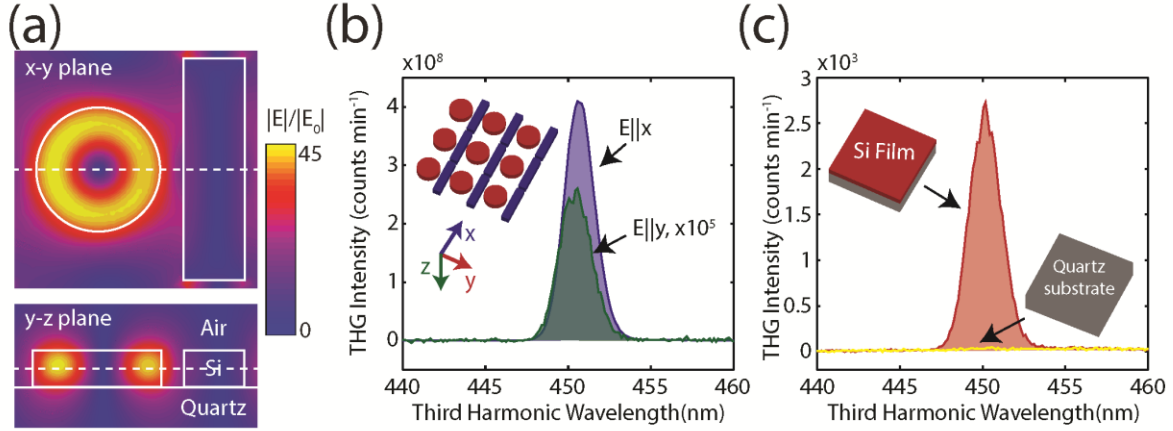
Figure 5.2. (a) Simulated electric field amplitude at the Fano resonance peak wavelength of 1350 nm in both the *x-y* and *y-z* plane. The choice of cut-plane is represented with the white dashed lines. (b) Third harmonic spectra of the metasurface with the incident electric field polarized along *x*-axis and *y*-axis, respectively. (c) Third harmonic spectra of an un-patterned Si film and a bare quartz substrate, respectively (average pump power of 25 mW, peak pump intensity of 1.6 GW cm^{-2}).

In addition to THG enhancement, the strong near-field enhancement in the metasurface can also substantially modify the refractive index of Si at the fundamental wavelength via the nonlinear Kerr effect. This index change in turn shifts the Fano resonance peak wavelength leading to all-optical modulation. Experimentally, this is manifest in the third harmonic peak wavelength deviating from $\lambda_0/3$ where λ_0 is the linear Fano resonance peak. This is illustrated in Fig. 5.3a which demonstrates that the THG peak deviates from the linear Fano resonance peak by 0.93 nm at peak pump intensity of 0.8 GW cm^{-2}. Further increasing the pump intensity to 1.6 GW cm^{-2} results in a 2.6 nm THG shift, demonstrating the expected intensity dependence. To better understand the origin of the peak shifts, the index change of the Si (Δn) can be calculated using:

$$\Delta n = n_{2(Si)} I_0 \frac{\int_{V_{Si}} |E|^2 / |E_0|^2 \, dV}{V_{Si}} \tag{5.2}$$

where I_0 is the peak pump intensity, $|E|^2 / |E_0|^2$ is the absolute field intensity enhancement factor, and V_{Si} is the volume of the Si resonator. As a first order approximation of the magnitude of this effect, numerical simulations were used to calculate the field intensities in the absence of any nonlinearities. Using equation 2, this yields a Δn of 0.0118 at 0.8 GW cm^{-2} peak pump intensity. Re-simulating the metasurface with the calculated Δn, we find the Fano resonance peak shifts by 3.5 nm for the fundamental wave (corresponding to a 1.17 nm THG shift), as is shown in Fig. 5.3b. While this is clearly a first order approximation, the general trend in the resonance shift is readily reproduced.

Combining the nonlinear Kerr effect with the narrow bandwidth of the linear transmittance spectrum, The Fano-resonant Si metasurface can serve as an ultra-thin all-optical modulator. In particular, we show the modulation of transmittance upon increasing the pump power in Fig. 5.3c. At 1348 nm (the linear Fano resonance peak), the transmittance gradually decreases with increasing pump power due to the fact that the Fano resonance peak red-shifts away from the pump wavelength. At 1352 nm, the transmittance shows a peak at ~1.6 GW cm^{-2} pump power as we pass through the resonance and gradually decreases as the resonance peak moves to 1352 nm with increasing pump power. At a pump wavelength of 1356 nm we begin considerably blue-shifted from the resonance and upon increasing pump power the transmittance shows a maximum at ~1.8 GW cm^{-2} resulting in a modulation depth $(T - T_0)/T_0$ of 36%, where T_0 is the linear transmittance of the sample. In these measurements, we focus the laser to a tight spot of ~225 um^2, which introduces a finite angle of incidence. As the Fano

73

resonance is relatively sensitive to the incident angle (see Appendix D2 for details), the contrast in transmittance is lower when compared with the measured linear transmittance spectra in which near-normal incidence white light is utilized.
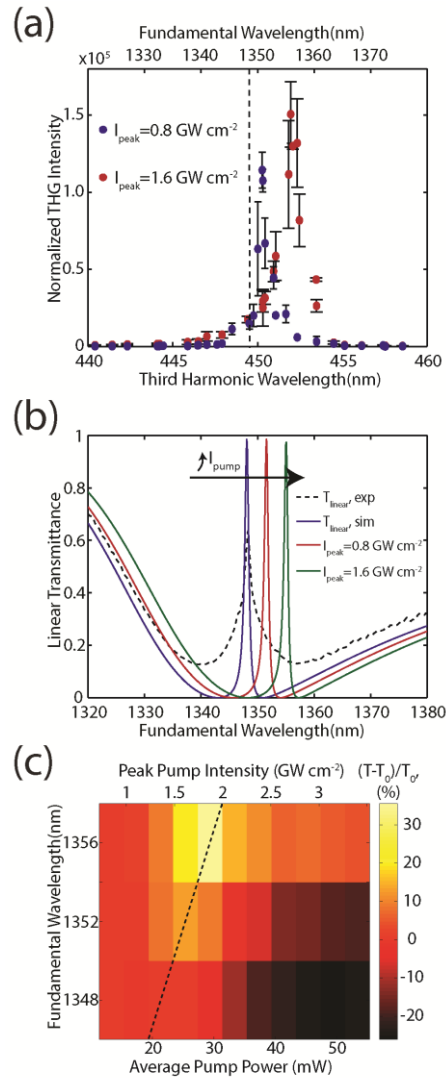
Figure 5.3. (a) The wavelength-dependent THG intensity of the metasurface when normalized to an un-patterned Si film of the same thickness. The blue points are data taken under 0.8 GW cm^{-2} peak pump intensity, and the red points are data taken under 1.6 GW cm^{-2} peak pump intensity. The black dash line indicates the linear Fano resonance peak. (b) Simulated transmittance of the metasurface under different pump intensity. The measured transmittance under low power white light illumination is also shown as the black dashed line for a reference. (c) The relative change in transmittance as a function of pump power at 1348 nm, 1352 nm and 1356 nm. The black dash line shows the shift of the transmittance peak with increasing pump power.

5.4 Absolute Third Harmonic Efficiency

The absolute THG efficiency for the Fano-resonant Si-based metasurface was characterized by simultaneously measuring the pump and THG beam power (see Appendix D1 for details of the measurement). Based on these measurements, a conversion efficiency of 1.18×10^{-6} with an average pump power of 50 mW and a peak pump intensity of 3.2 GW cm^{-2} was measured, as shown in Fig. 5.4a. These measurements were performed with a pump laser with a linewidth of ~15 nm, which is much greater than the linewidth of the Fano resonance (~2.9 nm). A photograph of the sample under 50 mW average pump power (Fig. 5.4b) clearly shows the third harmonic blue light emission. However, to achieve higher conversion efficiency and reach the saturation threshold of the metasurface, a pump laser with larger peak intensity is required. To achieve this, we used the signal output of an optical parametric amplifier (OPA) as the pump and repeated the absolute THG efficiency measurement (see Appendix D1 for details of the measurement). With an OPA as the pump, we measured a conversion efficiency of 7.2×10^{-6} with a plateau in the conversion efficiency occurring at 300 GW cm^{-2}. The relatively low conversion efficiency at the large pump fluence is most likely due to the Fourier-transform-limited bandwidth of the OPA signal (~60 nm). Namely, the large bandwidth of the laser results in inefficient coupling of the pump beam to the resonant mode of the metasurface, which has a linewidth of only ~2.9 nm. To further increase the conversion efficiency, a chirped pulse with the maximum of the pulse centered at the Fano resonance peak wavelength could be used. Nevertheless, the THG saturation intensity demonstrated here is still orders of magnitude higher than previously

reported nanoscale nonlinear photonic devices[145], [159]. While the THG of many on-chip nonlinear photonic devices such as ring resonators and slow-light waveguides[155], [156] suffer from saturation due to TPA of the fundamental wave, here the THG is only moderately affected by TPA due to the sub-wavelength thickness of the metasurface.
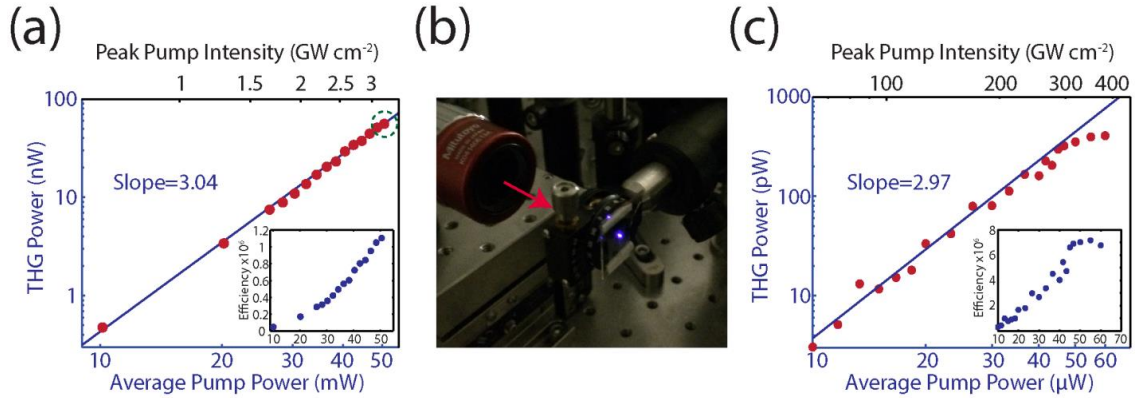
Figure 5.4. (a) Log-log plot of the third harmonic power as a function of the pump power and the peak pump intensity with OPO. The red circles indicate the measured data, and the blue line is a numerical fit to the data with a third-order power function. The green circle denotes the pump power at which the photograph in panel b was taken. The inset shows the extracted absolute THG efficiency as a function of the pump power. (b) A photograph taken under ambient room light showing blue light emission from the sample for an incident wavelength at 1350 nm (average pump power of 50 mW, peak pump intensity of 3.2 GW cm^{-2}). (c) Log-log plot of the third harmonic power as a function of the pump power and the peak pump intensity with OPA. The inset shows the extracted absolute THG efficiency as a function of the pump power.

5.5 Conclusion

To summarize, utilizing the large near-field enhancements in a Fano-resonant Si-based metasurface, we have demonstrated highly efficient visible (blue) THG and all-optical nonlinear modulation. Such a platform can also be applied for other nonlinear processes such as four-wave mixing[34], Raman amplification[164], and may even be extended to Si-based coherent lasing[165]. By combining the Kerr shift with the narrow

bandwidth of the linear transmittance spectrum the dielectric metasurface potentially opens a new route towards the realization of ultra-compact optical devices such as saturable absorbers and modulators.

Chapter 6 Metamaterial Perfect Absorber-based Quantum Well Infrared Photodetector

6.1 Introduction

Metamaterials have been demonstrated as an extremely versatile platform for controlling light matter interaction, showing capability in manipulating light emission, light propagation and light detection, as illustrated in the previous chapters of this dissertation. However, most metamaterials and metasurfaces to date are passive/quasi-passive devices. There has been a constant drive in the metamaterial research community to integrate metamaterials with active materials which change properties upon external stimuli in order to realize dynamically switchable meta-devices.

When high speed switching is not the prime objective, metamaterials can be tuned using microelectromechanical (MEMS) actuators that reposition parts of the metamolecules, along with other candidates such as chalcogenide glasses and liquid crystals [166]. To achieve high speed operation, people have already demonstrated dynamic tuning of a metamataerial's response at terahertz frequency by injection or optical generation of free carriers in a gallium arsenide or silicon substrate[167]. "Phase-change" materials are also promising for fast optical switching. In particular, the metal-insulator phase transition of vanadium dioxide can lead to a dramatic change in the dielectric and plasmonic properties[168]. Recently, it has also been found that a substantial change in the dielectric properties of a nanometer-thick layer can be achieved in conducting oxides through the injection of free carriers. By utilizing the inter- and intra-band transition, one can also achieve large modulation of the dielectric function of

graphene, in particular at IR and terahertz frequencies[169]. Combining such active materials with metamaterials, one can manipulate the resonant transmission or absorption of a hybrid meta-device, and therefore realizing controllable light propagation or detection. Other than the options listed above, scientists have recently found that metamaterials can interact with intersubband transitions in semiconductor quantum wells (QWs) such that a hybrid device with dynamic response tunability can be manufactured[170]–[172].

In this chapter, we focus on how one can integrate metamaterials with the active QWs to achieve enhanced photodetection in the long-wave infrared band ($\lambda \cong 10\mu m$). Here, we design a quantum well infrared photodetector (QWIP) that possesses near-unity absorption for normal-incident mid-infrared light. The perfect absorption is achieved by spectrally overlapping the magnetic-dipole resonances of a patterned *dielectric* QW stack with the electric-dipole resonances of patterned *metallic* strips to achieve impedance matching to free space at the frequency of the intersubband dipole transition of the quantum well. This dielectric and metal hybrid structure utilizes a surface plasmon resonance in the metallic strips to further promote light confinement within the QW as otherwise light tends to leak out into the high index substrate. The near-unity optical absorption in the active region of the QW, when combined with efficient photon-carrier generation and transport, can lead to greatly boosted photo-responsivity of the QWIP.
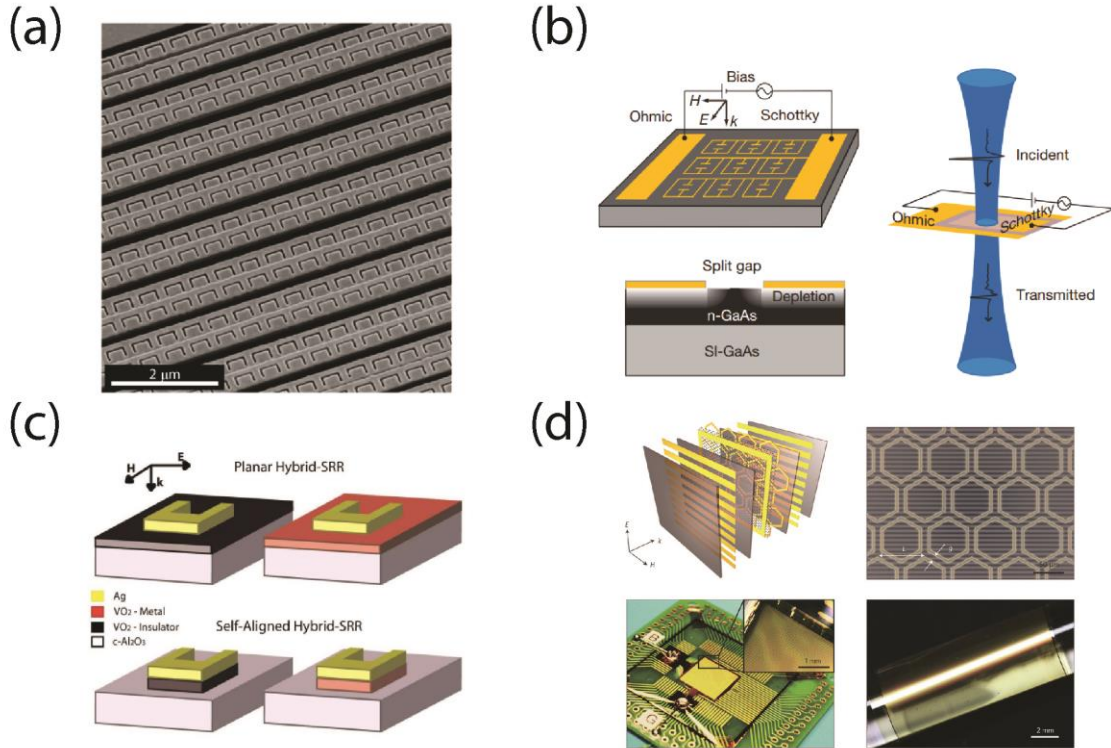
Figure 6.1. (a) An SEM image of a thermally controlled reconfigurable photonic metamaterial[166]. (b) Experimental design of an active THz metamaterial device based on carrier injection into the GaAs substrate[167]. (c) Hybrid split-ring resonator metamaterials based on vanadium dioxide[168]. (d) Schematic rendering of a gate-controlled active graphene metamaterial composed of a SLG deposited on a layer of hexagonal metallic meta-atoms[169].

6.2 Background

6.2.1 Intersubband Transitions & Quantum Well Infrared Photodetectors

For conventional photodetectors interband optical absorption is utilized and corresponds to photo-excited carriers transiting across the band gap E_g (Fig. 6.2a). In a detector structure these generated photocarriers can be collected through an external bias or a p-n junction, thereby producing a photocurrent. By controlling the E_g, the spectrum of the absorption and hence the wavelength dependence of the detector response can be modified. In the long-wavelength infrared region where $\lambda \cong 10 \mu m$, the required band gap

is $E_g \cong 0.1 eV$. Small-band-gap materials, such as mercury cadmium telluride (MCT), can manufactured, but are also more difficult to grow, process, and fabricate compared to larger-band-gap semiconductors[173]. To overcome this issue, the use of intersubband (intraband) transition involving the transition within the same band has been proposed. In order to create these subbands, QWs are used.

The QW is typically formed from narrow band-gap semiconductors (such as gallium arsenide, GaAs) sandwiched between two layers of a material with wider band-gap (such as aluminum gallium arsenide, AlGaAs), as is shown in Fig. 6.2(b). Such a structure can be grown by molecular beam epitaxy (MBE) or metal-organic chemical vapor deposition (MOCVD) with precise thickness control down to an atomic layer. The solution to the band structure of a QW is similar to the well-known "particle in a box" problem in quantum mechanics, which can be solved by the time-dependent Schrodinger equation. The solved eigen-values determine the allowed states of the particle. As an approximation, for the infinitely-high barriers and parabolic bands, the energy levels in the QW are given by,

$$E_j = \left(\frac{\hbar^2 \pi^2}{2m^* L_w^2} \right) j^2 \tag{6.1}$$

where L_w is the width of the well, m^* is the effective mass of the carrier in the quantum well, and j is an integer. Therefore, the intersubband energy between the ground and the first excited state is,

$$\left(E_2 - E_1 \right) = \frac{3\hbar^2 \pi^2}{2m^* L_w^2} \tag{6.2}$$

A typical QWIP utilizes the photo-excitation of the electron between the ground

and the first excited state ($E_1 \rightarrow E_2$ in Fig. 6.2b). However, in order to create these states within the conduction band these QWs must be doped because $hv < E_g$ and thus the incident photon energy is not sufficient to create photocarriers.

The growth of semiconductor QWs is relatively mature and is low-cost. In addition, the quantum well parameters can be designed to vary the intersubband optical spectrum at will whereas the band-gap of a typical semiconductor photodetector utilizing interband transition is fixed
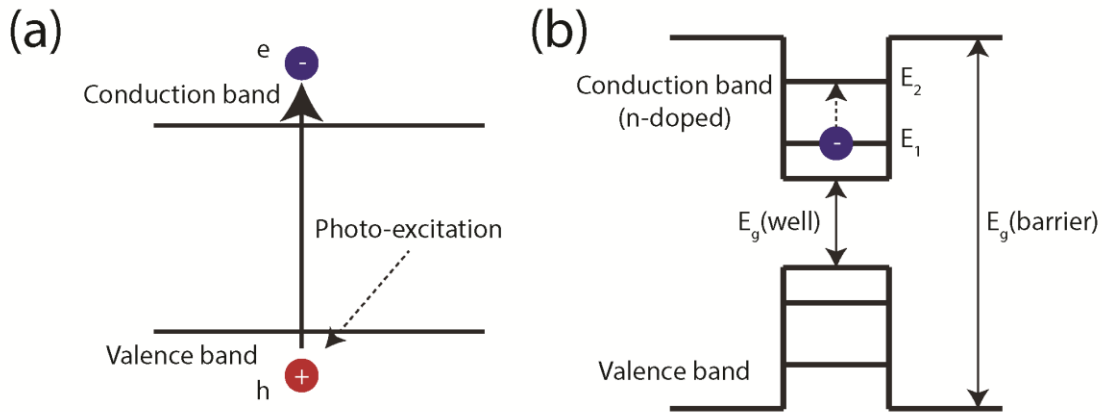
Figure 6.2. (a) Band diagram of interband transition occurring in a conventional intrinsic infrared photodetector. (b) Band structure of a QW. Intersubband transition between electron levels E_1 and E_2 is schematically shown.

.

6.2.2 Optical Coupling Method for Quantum Well Infrared Photodetectors

One major challenge associated with using QWs for infrared photodetection is that QWIPs do not absorb normal incident light because the light polarization must have an electric field component normal to the growth direction of the well to be absorbed by the confined carriers. When the incoming light contains no polarization element along the

growth direction the matrix element of the interaction vanishes. As a consequence, an alternative light coupling scheme is required.
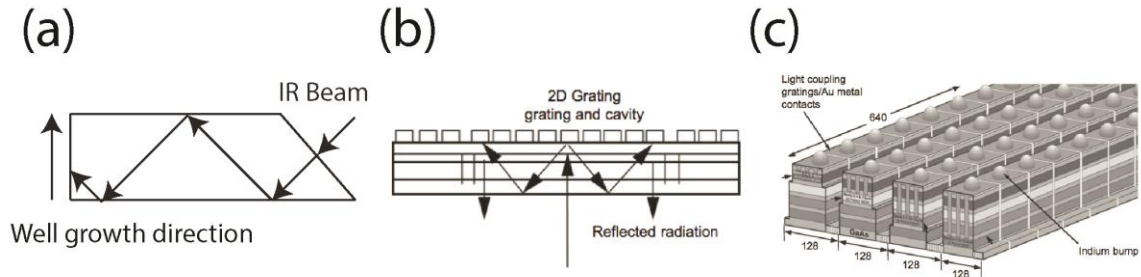
Figure 6.3. (a) Conventional 45 degree wedge waveguide coupling. (b) Schematic diagram of 2-D periodic gratings. (c) Layer diagram of a four-band QWIP device and the deep groove periodic grating structure. Figure adapted from ref.[174].

The most commonly adapted approach is to illuminate the QWIP through a 45° polished facet[174]. However, this illumination scheme limits the configuration of detectors to linear arrays and single elements. For applications such as imaging, it is necessary to couple light uniformly to a two-dimensional (2D) array of these detectors.

Alternatively, several monolithic grating structures such as linear and 2D periodic gratings have been proposed and demonstrated for efficient light coupling to QWIPs and to enable QWIP-based imaging. These gratings deflect the incoming light away from the direction normal to the surface and scatter light into orders with a parallel wave-vector that is an integer multiple of the reciprocal lattice-vector of the gratings. However, the diffraction efficiency and thus the absorption in the QW region is typically less than 10%[175].

6.3 Design of a Metamaterial Perfect Absorber with Integrated Quantum Wells

6.3.1   One-dimensional Polarization-sensitive Design
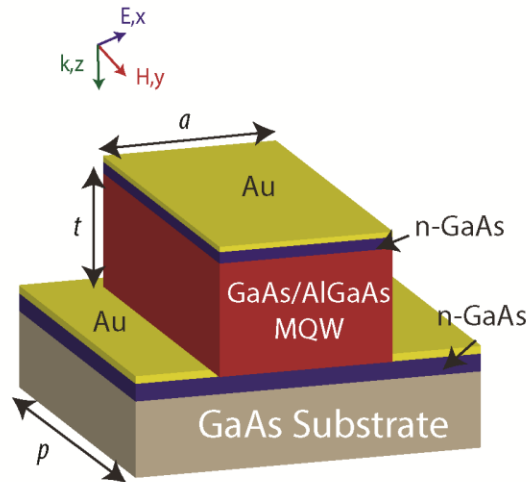
Figure 6.4. 3D view of the quantum well-integrated metamaterial perfect absorber. The top and bottom Au layers have a thickness of 50 nm. The other geometric parameters are p=3500 nm, a=1500 nm, t=1000 nm.

To start, we first examine a 1D perfect absorber design which is sensitive to the polarization of the incoming light. The device schematic of the quantum well-integrated metamaterial perfect absorber is shown in Fig. 6.4 The structure is composed of a top Au layer, a top n-doped GaAs contact layer, an active QW layer, a bottom Au layer and a bottom n-doped GaAs contact layer sitting on an intrinsic GaAs substrate.
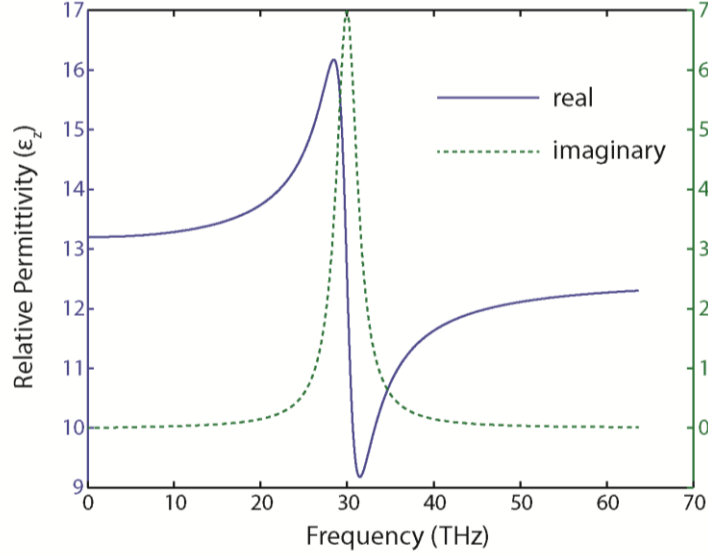
Figure 6.5. The real and imaginary permittivity of the GaAs quantum well along the z-(quantum well growth)-direction.

In order to calculate the optical response of the QW-integrated metamaterial perfect absorber, the frequency dependent permittivity tensor of the composite materials needs to be obtained. The gold permittivity is described using a Drude model with an angular plasma frequency of $2\pi \times 2060 \times 10^{12}$ rad/s and a damping rate of $2\pi \times 10.9 \times 10^{12}$ 1/s. By only considering the transition between the two lowest subbands, the permittivity tensor for a gallium GaAs/AlGaAs quantum well grown in the [001] direction is,

$$\varepsilon_{GaAs}^{QW}(\omega) = \begin{pmatrix} \varepsilon_{GaAs}^{b}(\omega) & 0 & 0 \\ 0 & \varepsilon_{GaAs}^{b}(\omega) & 0 \\ 0 & 0 & \varepsilon_{GaAs}^{b}(\omega) \end{pmatrix} + \begin{pmatrix} 0 & 0 & 0 \\ 0 & 0 & 0 \\ 0 & 0 & 1 \end{pmatrix} \chi_0(\omega) \tag{6.3}$$

where

$$\chi_0(\omega) = -\frac{Ne^2}{\varepsilon_0 \hbar} \frac{|z_{21}|^2}{(\omega - \omega_{21} + i\gamma_{21}/2)} \tag{6.4}$$

where $\varepsilon_{GaAs}^{b}(\omega) = 10.7$ is the permittivity of bulk GaAs crystal, $N=1.2 \times 10^{18}$ 1/cm^3 is the

electron doping density, $z_{21} = 0.67$ is the dipole strength, $\omega_{21} = 30\,\text{THz}$ is the dipole transition energy, and $\gamma_{21} = 3\,\text{THz}$ is the damping rate. The real and imaginary part of ε_z of the QW are plotted in Fig. 6.5. Note that the intersubband transition only occurs along the quantum well growth direction, which leads to a strongly anisotropic behavior of the effective QW permittivity.
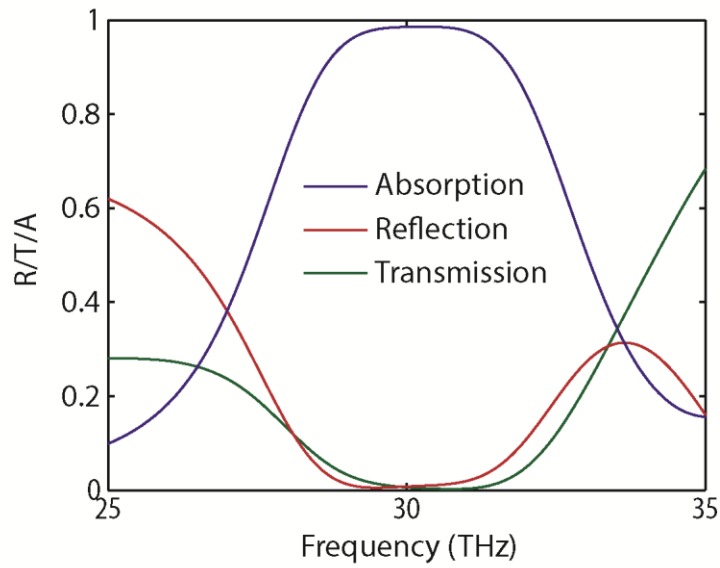
Figure 6.6. Transmission, reflection and absorption spectra of the structure from full wave simulation under normal plane wave illumination.

When the structure is illuminated with electric field along the *x*-direction, localized surface plasmon resonance (electric dipole resonance) can be excited at both the top and the bottom Au layer with anti-parallel current flow, as can be observed in Fig. 6.7(a). In addition, a magnetic dipole resonance, similar to the one in the zero index metamaterial, is excited in the cavity formed in the dielectric QW layer, as is shown in Fig. 6.7(b). By carefully designing the resonator length *a*, quantum well height *t,* and the

periodicity *p*, the electric and magnetic dipole resonances can be spectrally overlapped,

leading to near-unity absorption as calculated using full-wave simulation and shown in

Fig. 6.6. The full-width-at-half-maximum (FWHM) of the absorption peak is 5.5 THz,

well beyond the FWHM of the intersubband transition. Furthermore, we calculated the

power loss density of the structure at 30 THz, and find that over 95% of the light

absorption occurs in the active QW layer. This architecture also enables one-step

lithography, dry-etching and metal evaporation, greatly simplifying the conventional

metamaterial perfect absorber fabrication, which typically requires a separate step for

defining the bottom Au reflector. This is especially important because that the active QW

layer can only be epitaxially grown on a GaAs substrate and cannot be growth directly on

an Au backplane.
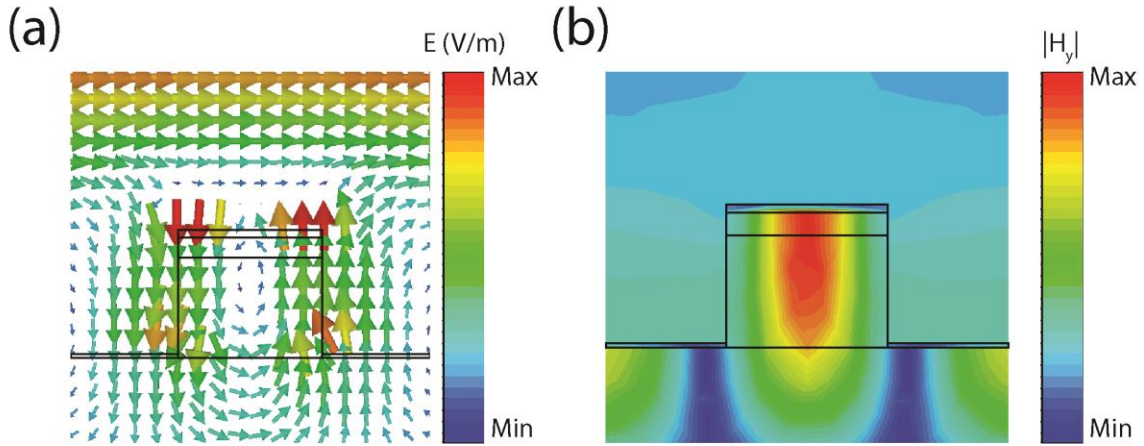
Figure 6.7. (a) Vector plot of the electric field from full wave simulation with the frequency of incident light at 30 THz. (b) Simulated magnetic and electric field amplitudes with the frequency of incident light at 30 THz.

6.3.2   Device Performance Versus Incident Angle

Another important metric of a photodetector is the light acceptance angle. In

contrast to previously demonstrated metal grating-based quantum well infrared photodetectors that utilize the excitation of *non-localized* propagation surface plasmon modes through grating coupling, our structure relies on spectrally overlapping the magnetic-dipole Mie resonances of a patterned QW stack with the *localized* surface plasmon resonances of patterned gold strips, therefore preserving a relatively angle-insensitive response.

It can be seen from Fig. 6.8(a) that for transverse electric- (TE-) polarized light where the electric-field is always parallel to the QW surface; the absorption is maintained above 80% for incident angles up to 60°. For transverse magnetic- (TM-) polarized light, the structure is more sensitive to the incident angle, as is shown in Fig. 6.8(b). This originates from the anisotropic absorption of the QWs.
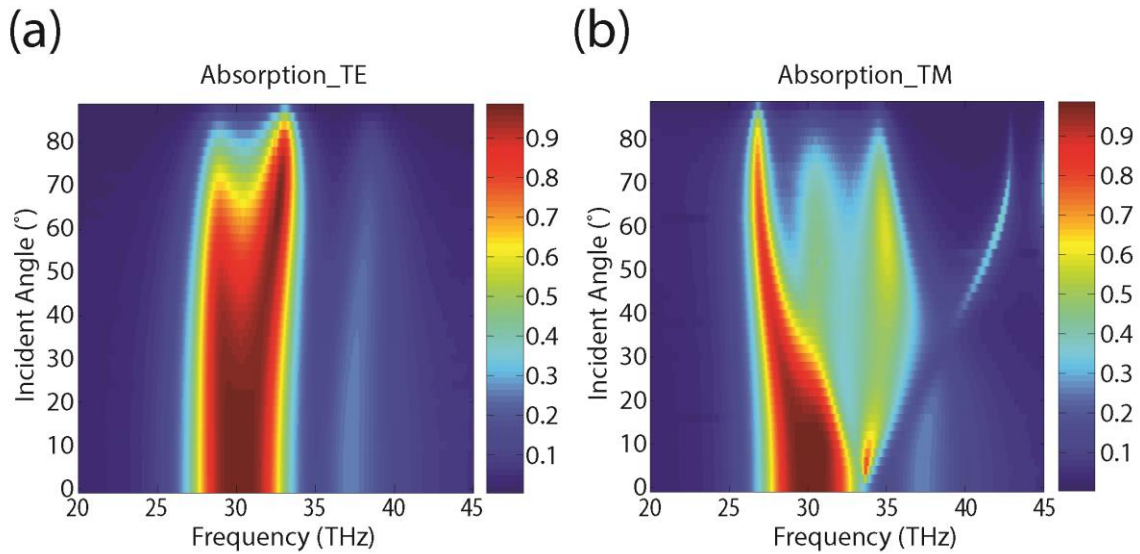
Figure 6.8. The simulated angular dispersions of the absorbance peak for TE(a) and TM configurations(b).

6.3.3 Two-dimensional Polarization-Insensitive Design

In order to achieve a polarization-independent photo-response, the 1D stripe resonators can be replaced by square resonators. However, to ensure electrical connection on the top side, thin-metallic bus-bars are also needed. The schematic of the polarization-independent design is shown in Fig. 6.9(a). The polarization-independent perfect absorber structures still maintain a near-unity absorption, as is illustrated in Fig. 6.9(b).
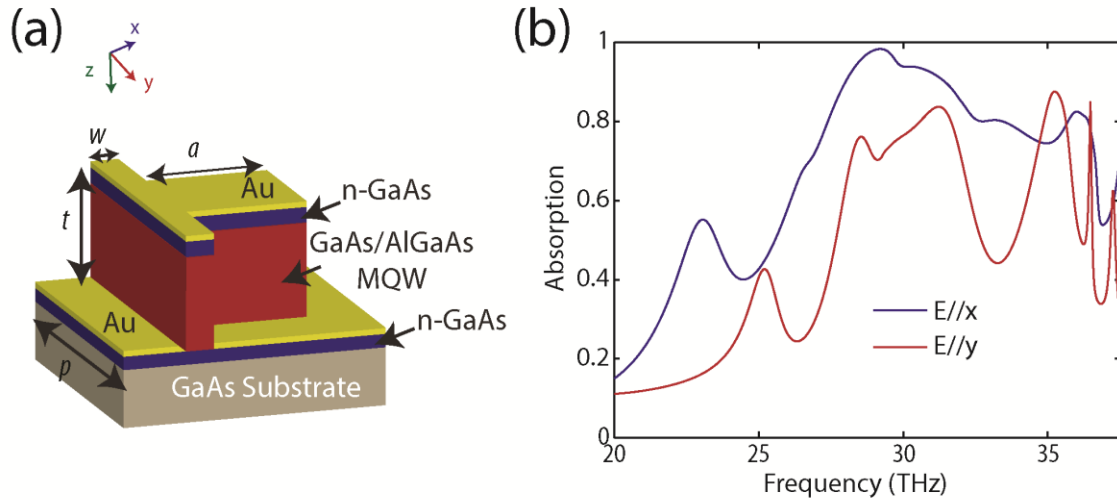
Figure 6.9. (a) 3D view of the quantum well-integrated metamaterial perfect absorber. The top and bottom Au layers have a thickness of 50 nm. The other geometric parameters are p=3500 nm, a=1500 nm, t=1800 nm, w=400 nm. (b) Simulated absorption spectra of the structure under normal plane wave illumination with electric field polarized along x-direction (blue) and y-direction (red), respectively.

6.3.4 Routes Towards Device Fabrication and Characterization

While the fabrication and testing of the structure is beyond the scope of this dissertation, the routes towards the experimental realization of the metamaterial perfect absorber-integrated QWIP are still presented here. The quantum well stack, including an n-doped GaAs conduction layer (bottom electrode), AlGaAs multiple quantum wells and

an n-doped GaAs buffer layer, can be grown using molecular beam epitaxy (MBE). The perfect absorber structure can be created through the combination of electron/photo-lithography, reactive-ion etching of the multiple quantum well stack, and metal deposition. The top electrical contact can be achieved through direct contact with the top metal film, while the bottom contact can be defined on top of the exposed n-doped GaAs conduction layer beneath the active QW layer. Both polarization-sensitive and insensitive devices can be fabricated as well as a multiple-pixel detector composed of perfect absorber-based device elements resonant at multiple wavelengths.

The optical absorption spectrum can be measured using a Fourier-transform infrared spectroscopy (FTIR) microscope system and the photo-responsivity, photocurrent spectrum, and dark current noise of the device can be measured using a tunable CO_2 laser as a light source.

6.4 Conclusion

This device architecture overcomes the issue of low photo-responsivity in conventional quantum well infrared photodetectors due to inefficient coupling and absorption of normal incident light. The designed quantum well infrared photodetector structure supports a perfect absorber-type resonant mode. The resonant mode has a large out-of-plane electric field component, overlapping with the out-of-plane dipole transition of the quantum well, allowing near-unity absorption in the active quantum well layer and therefore high photo-responsivity.

Compared to the current techniques of using a 45 degree wedge waveguide or periodic metallic gratings and roughened random reflectors, our approach preserves a

greatly boosted photo-responsivity and compact device architecture. Polarization-insensitive photodetection can also be realized through a two-dimensional perfect absorber design with a thin electrical bus-bar. With a pixelated perfect absorber design with different absorber geometries and intersubband transition frequencies, we envision multi-color and/or broadband photodetection can be realized.

Chapter 7 Conclusion and Outlook

The focus of this research has been to engineer the resonance properties of dielectric metamaterials and metasurfaces for a variety of applications including enhanced light emission, polarization and phase manipulation, bio-sensing, enhanced nonlinear interaction, and enhanced infrared photodetection. There were several impactful results obtained on this journey of probing the exotic behavior of resonant dielectrics. In this chapter, I will summarize these findings as well as outline several promising research directions in the metamaterial field.

7.1 Conclusion

In Chapter 2, I described the first experimental realization of an impedance-matched low-loss 3D zero-index metamaterial (ZIM) with all-dielectric components at optical frequency. A metamaterial exhibiting an effective refractive index of zero was designed and fabricated based on low-loss silicon (Si) resonators. The ZIM has a nearly isotropic response for transverse magnetic polarized light, which leads to its angular selectivity and the ability to enhance and direct the spontaneous emission of the embedded quantum dot emitters within the ZIM.

In Chapter 3, I transitioned the focus from bulk 3D dielectric metamaterials to the study of ultrathin 2D dielectric metasurfaces. I showed that engineered dielectric nano-antennas exhibiting Mie resonances can be used in place of plasmonic antennas to drastically modify the phase of light while maintaining near-unity efficiency. I experimentally demonstrated highly efficient linear polarization conversion with more

than 98% conversion efficiency over a 200 nm bandwidth in the short-wavelength infrared band. In addition, I demonstrated optical vortex beam generation using a silicon-based meta-reflectarray with azimuthally varied phase profile.

In Chapter 4, I studied of the dielectric metasurface analogue of electromagnetically induced transparency. Due to extremely low absorption loss and coherent interaction of neighboring meta-atoms, I realized Fano-type resonances with quality factors of 483. This is realized by forming a periodic array of coupled electric and magnetic dipole antennas and the associated minimization of the non-radiative decay of light. Combining the sharp resonance with strong field confinement in its surrounding medium, I show that such a device can be an ideal platform for bio-sensing, and experimentally demonstrated a refractive index sensor with a figure-of-merit of 103.

In Chapter 5, I further investigated nonlinear light-matter interaction in Fano-resonant dielectric metasurfaces. The metasurface results in strong near-field enhancement within the volume of the silicon resonator while minimizing two photon absorption, leading to greatly enhanced efficiency and increased saturation power for third harmonic generation. The enhanced nonlinearity, combined with a sharp linear transmittance spectrum, results in transmission modulation via the Kerr effect with a large modulation depth.

In Chapter 6, I presented a design for a quantum well infrared photodetector integrated with the concept of metamaterial perfect absorbers. By stringently overlapping the electric and magnetic resonances of a quantum well-metal hybrid, the structure can achieve near-unity light absorption in the quantum wells, leading to greatly enhanced quantum efficiency of a quantum well-based infrared photodetector. A practical

fabrication and optical/electrical characterization schematic has also been outlined.

7.2 Future Outlook of Metamaterials

During the past two decades, researchers have used metamaterials to obtain numerous unique optical properties not attainable from conventional optical components. However, a greater challenge remains regarding the realization of practical meta-"devices" with superior performance. Beyond reducing material loss, as outlined in this thesis, I believe there are many other attractive directions to pursue. Here I briefly list a few.

The first area of interest, I believe, is compact electrically-tunable 2D metasurfaces. Although active metamaterials allowing dynamic modulation of light flow have been one of the major directions in the metamaterial research community for many years, there are still significant issues such as the realization of low-voltage electrical modulation in a compact platform and the realization of "on/off"-style tuning instead of only minor spectral modification. To achieve low-voltage electrical modulation, the utilization of tunable intersubband transitions in quantum wells can be particularly interesting, as it allows dramatic modulation of the dipole transition energy with a low voltage bias when the quantum wells are asymmetrically coupled. To realize the "on/off"-style modulation, a better engineered far-field spectral response and near-field interaction of the optical field and the active material needs to be achieved.

Another interesting topic is to integrate the design concept of metamaterials with gain materials for greatly reducing the lasing threshold of solid state semiconductor lasers. I believe there is much to explore here as metamaterials may offer the ultimate

design freedom for engineering the Purcell factor and the local environment for emitters.

Finally, I believe another interesting route is to use metamaterials to enhance the performance of existing optoelectronic devices such as waveguides, CMOS imaging sensors, and photovoltaics, in which case a much more comprehensive evaluation involving the performance gain, system robustness, and cost has to be conducted.

Appendix A: Zero-index Metamaterial

A.1 Retrieval of the effective index from the Bloch modes

Retrieval of the permittivity and permeability was carried out by extracting the average field components from the TM Bloch modes at the boundary of the unit cell $(\bar{E}_x, \bar{D}_x, \bar{H}_y, \bar{B}_y, \bar{H}_z, \bar{B}_z)$. In the extraction of the permittivity and permeability, we ensure the continuity of the tangential and normal components of the average field at the unit cell boundary, ensuring that Maxwell's equations are satisfied. The constitutive equations for the average fields are then given by,

$$\begin{bmatrix} \bar{D}_x \\ \bar{B}_y \\ \bar{B}_z \end{bmatrix} = \begin{bmatrix} \varepsilon_0 * \varepsilon_x & A_{xy} & A_{xz} \\ A_{yx} & \mu_0 * \mu_y & A_{yz} \\ A_{zx} & A_{zy} & \mu_0 * \mu_z \end{bmatrix} \begin{bmatrix} \bar{E}_x \\ \bar{H}_y \\ \bar{H}_z \end{bmatrix} \tag{A.1}$$

The diagonal elements of the 3 x 3 parameter tensor define the permittivity (ε_x) and permeability (μ_y, μ_z) of the bulk structure along the x, y and z directions respectively.

A.2 Optical property retrieval from the Bloch modes and extended states

To ensure that an accurate retrieval of the material properties was acquired, we compared the retrieved wavevector, computed with the retrieved effective index, to the band structure calculated numerically using MIT Photonic Bands (MPB) in the range from Γ to X, as illustrated in Fig. A.1(a). The retrieved band structure has a very good agreement with the MPB band structure at smaller k_y, though it deviates at large k_y as spatial dispersion becomes apparent near the band edge. Only the transverse bands are considered in the calculation of the effective optical properties.

In order to properly assign a refractive index to a material for off-normal angles of

incidence, there must be only one propagating band at a particular frequency. To verify

that there is only one propagating band within the material, we simulated the extended

states of the crystal, shown in Fig. A.1(b). Within the frequency range from 215 THz to

225 THz, slightly above the zero-index point, there is a single band (TM4) throughout *k*-

space. Within this region, a refractive index may be assigned to the metamaterial, though

it may change slightly with the angle of incidence, as illustrated in the IFC plot shown in

Fig. 2.2(d).
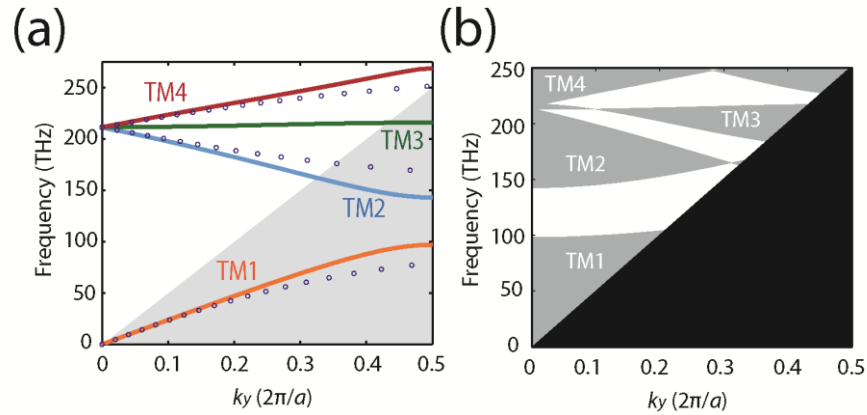
Figure A.1. (a) The solid lines represent the band structure of the square lattice calculated from MPB and the circles correspond to band diagram retrieved from effective index n_{eff} and the dispersion relation $k_y = n_{eff}\,\omega/c$. The mismatch of the two methods at the band edge is due to the fact that the effective medium approximation no longer holds in those regions. (b) Extended states of the crystal showing that only one band (TM4) is present between 215 THz and 225 THz, allowing an effective index to be assigned to this region.

A.3 Optical property retrieval from the Bloch modes and extended states

To further justify our claim that the proposed metamaterial structure can indeed be

homogenized as an effective medium and has an isotropic low index property for TM-

polarized light, we conducted numerical simulation with a Gaussian beam incident at the

ZIM from multiple angles. The wavelengths of the incident beams (1340nm and 1380nm)

are chosen such that they fall within the bandwidth where only one propagating band (TM4) exists.

The simulated electric field profiles with multiple angles of incidence and wavelengths are shown in Figs. A.2 (a)-(f). In all cases, we see no higher order diffraction taking place at the exit surface of the sample. The transmitted light from the material is plane wave like as shown in Figs. A.2 (a),(b),(d),(e) for normal and low angle incidence, while light transmission is clearly forbidden at even higher angles of incidence due to the conservation of parallel angular momentum (Figs. A.2c,f).

From the field plots in Fig. A.2(b), with 10° incidence at 1340 nm, the light refracts at an angle of ~ 43° with clearly longer effective wavelength inside the material. From simple calculation from Snell's law we find the corresponding n_{eff} agrees well with retrieved index of 0.254. The same phenomenon occurs with 5° incidence at 1380 nm where the refraction angle is ~ 46°, which corresponds to a n_{eff} of 0.121 and again matches our parameter retrieval result.

In Figs. A.2(g)-(i), we illustrated the refraction phenomenon at 1458 nm which is negative index region where calculated index is -0.121, i.e. the same absolute value of index for 1380 nm wavelength. With 0° angle of incidence the light transmits normally out of the material with plane wave profile. With 5° incidence we can clearly see the negative phase propagation inside the medium, finally light transmitting out of the exit surface at 5° from the normal. But contrary to the refraction phenomenon at 1380 nm, refraction is not forbidden at 30º angle of incidence for 1458 nm wavelength, due to coupling to the longitudinal band at higher angle.
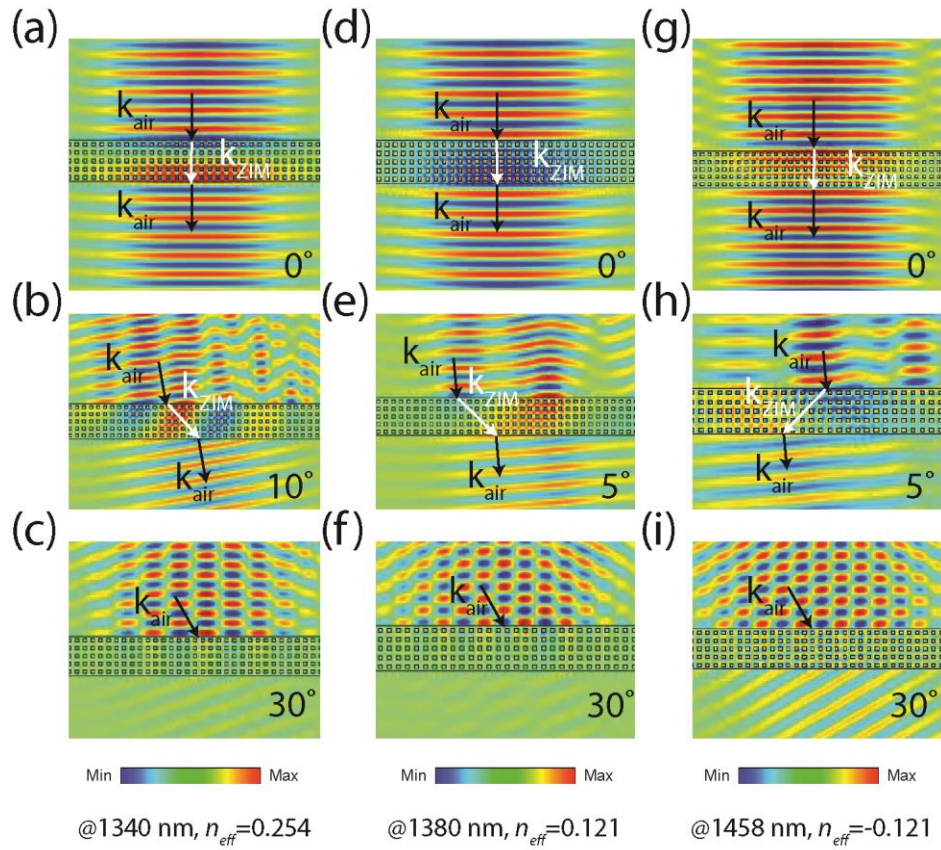
Figure A.2. (a)-(c), Light incidence at 0 °, 10 °, 30 ° respectively at wavelength of 1340 nm. (d)-(f), Light incidence at 0 °, 5 °, 20 ° respectively at wavelength of 1380 nm. (g)-(i), Light incidence at 0 °, 5 °, 20 ° respectively at wavelength of 1458 nm.

Appendix B: Meta-reflectarray

B.1 Fabrication of Meta-reflectarray

Amorphous silicon (Si) (n=3.7) was chosen as the resonator material due to its high index contrast. In order to incorporate the silver mirror while also using LPCVD for the Si layer, we reversed the conventional fabrication steps by first depositing silicon on quartz, followed by patterning the cut-wires and addition of the low index spacer and silver mirror. Amorphous Si was deposited on quartz using an LPCVD horizontal tube furnace. A quartz caged boat was used to contain the wafer to improve cross wafer uniformity. Deposition temperature was 550 °C and process pressure was 300 mTorr. Process gases were introduced into the tube furnace via mass flow controllers by flowing 50sccm's of 100% SiH_4.

The silicon cut-wire patterns were created by a sequential process of EBL, mask deposition, lift-off and RIE. In the EBL process, we coated a 10 nm chrome charge dissipation layer on top of PMMA resist to avoid surface charging, and the chrome layer was subject to chemical removal prior to the resist development. The total pattern size was ~1 mm x 1 mm for the polarization converter and 3 mm x 3 mm for the vortex beam generator, both patterns were written using a JEOL 9300FS 100kV EBL tool. We used a fluorine-based RIE recipe to etch the silicon with 80 W RF, 1200 W ICP power and C_4F_8, SF_6, O_2 and Ar gas flows.

PMMA was then spin-coated on the sample, followed by soft baking (180 degrees for 2 minutes) and reflowing at 300° C for 2 minutes to reach the desired thickness and flatness. In the last step, 150 nm of silver was thermally deposited on top of the sample,

serving as the ground plane mirror. The entire process is summarized in Figure B.1.
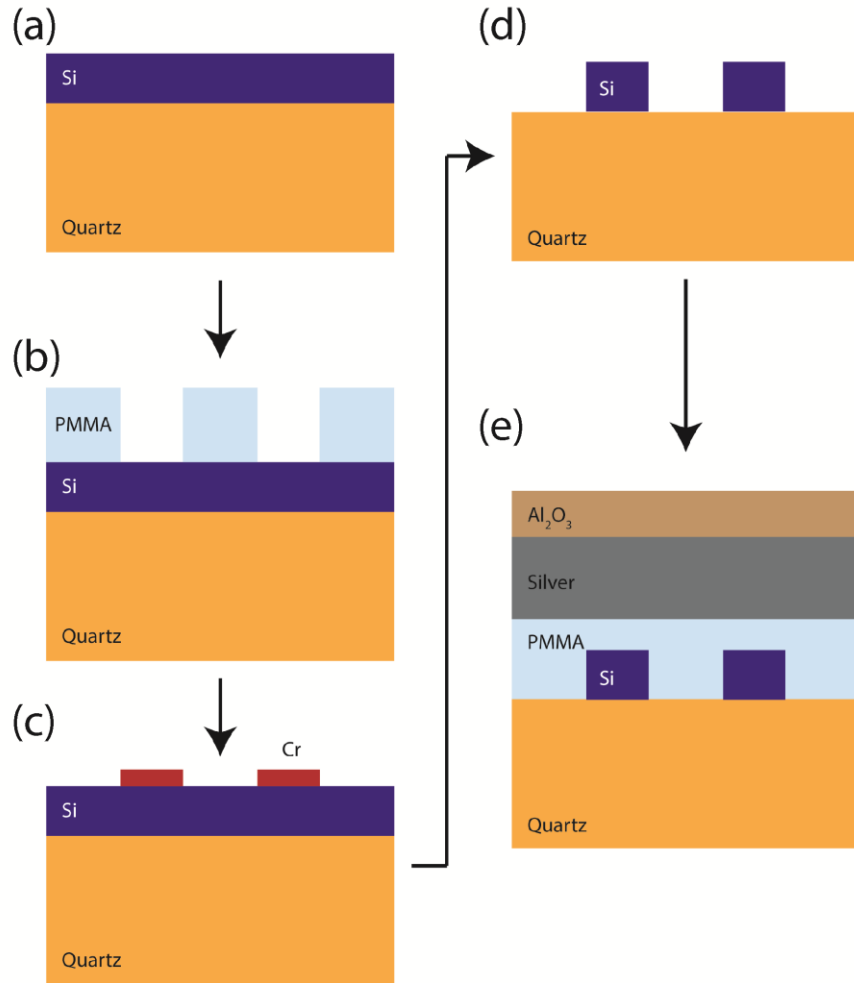
Figure B.1. (a) LPCVD silicon on quartz. (b) EBL patterning. (c) Etch mask deposition and lift-off. (d) RIE. (e) PMMA spinning and silver deposition.

B.2 Device Performance with Changing Incident Angle

Here we provide the angle-dependent response of the meta-reflectarray for both s- and p-polarized light as is shown in Fig. B.2. From the result, we find two interesting features. First of all, the bandwidth of the highly efficient polarization conversion gets

reduced with increased angle of incidence. More interestingly, extremely high Q-factor guided mode resonance can be excited. This phenomenon has been well explained in theory as the Fano-type interference of free space light and photonic crystal mode[138], and has been experimentally observed previously[176]. We agree with the reviewer that this may be a limiting factor for the waveplate operation in reflection mode. However, the extremely high Q resonant mode may open up new avenues for application such as sensing and enhanced light emission in cross-polarized or circularly polarized mode, which can be potentially very interesting.
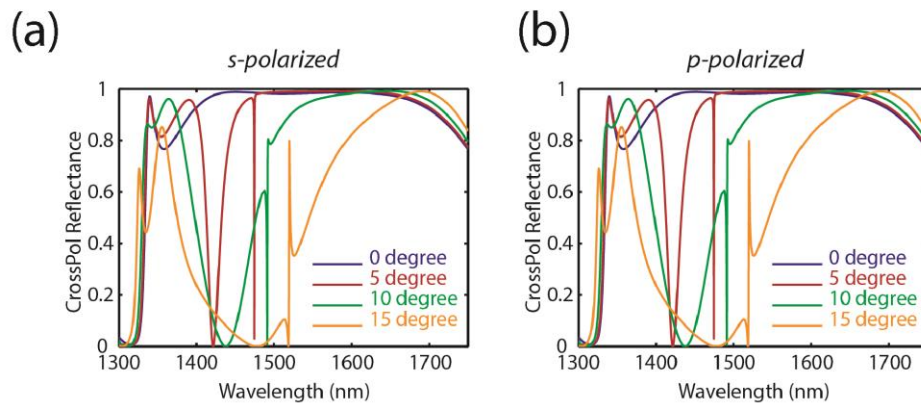
Figure B.2. Cross-polarization reflectance as a function of incident angles for (a) s- and (b) p-polarized light respectively.

Appendix C: Dielectric Metasurface Analogue of Electromagnetically Induced Transparency

C.1 Q-factor Extraction

We used a Fano model to extract the Q-factor of the EIT resonance from the dielectric metasurface. The experimentally measured transmittance T_{exp} was fitted to a Fano line shape given by $T_{Fano} = \left| a_1 + ja_2 + \dfrac{b}{\omega - \omega_0 + j\gamma} \right|^2$, where a_1, a_2 and b are constant real numbers; ω_0 is the central resonant frequency; γ is the overall damping rate of the resonance. The experimental Q-factor was then determined by $Q = \dfrac{\omega_0}{2\gamma}$. The fit was performed over the wavelength range from 1367 nm to 1380 nm as this model only encompasses the Fano line shape and does not include the fit to the background resonance provided by the bright mode. We used a fitting method identical to the one used in a recent demonstration of silicon-based chiral metasurface[25], therefore rendering the reported Q-factors in both cases comparable. The fit is shown in Fig. C.1
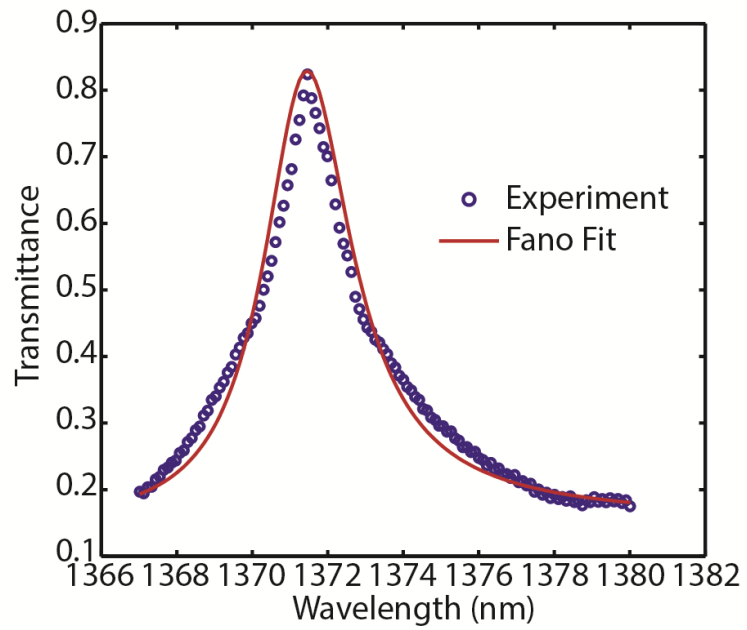
Figure C.1. Fano fit of the experimentally measured transmittance spectrum.

Appendix D: Nonlinear Dielectric Fano-resonant Metasurface

D.1 Measurement Set-up

D.1.1   Linear/Nonlinear Spectroscopy

The linear transmittance of the metasurface was measured using a custom-built free-space infrared microscope. A tungsten/halogen lamp was used as the light source and the metasurface array with a size of 300 μm x 300 μm was imaged using an infrared camera. To restrict the angle of incidence to near-normal, a low numerical aperture (NA) objective (Mitutoyo, 5x, 0.14 NA) was used to weakly focus the light on the metasurface, with the NA further cut down to 0.025 by an aperture at its back focal plane. The transmitted light was then collected by a high NA objective (Nikon Plan Apo Lambda, 60x, 0.95 NA) and coupled to an InGaAs-based grating spectrometer through a multimode fiber.

For the nonlinear spectroscopy measurement, a Ti-Sapphire laser oscillator (Coherent Chameleon) was coupled to an OPO (optical parametric oscillator, Coherent Mira) to provide a pump beam with a wavelength tunable from 1 μm to 1.6 μm (pulse duration ~250fs, repetition rate of 80 MHz). The laser was focused on the metasurface using a 0.14 NA objective with a beam size of ~225 um^2. The laser power was adjusted using the combination of a half waveplate and a linear polarizer. The transmitted fundamental and third harmonic waves were then collected by a high numerical aperture objective (Nikon Plan Apo Lambda, 60x, 0.95 NA), such that any diffracted THG was collected. The THG spectra from either the metasurface or an un-patterned Si film were then acquired using a grating spectrometer (Horiba iHR320). A short-pass filter

(Semrock, 790 nm blocking edge BrightLine®) was placed in front of the spectrometer to filter out the IR pump beam.
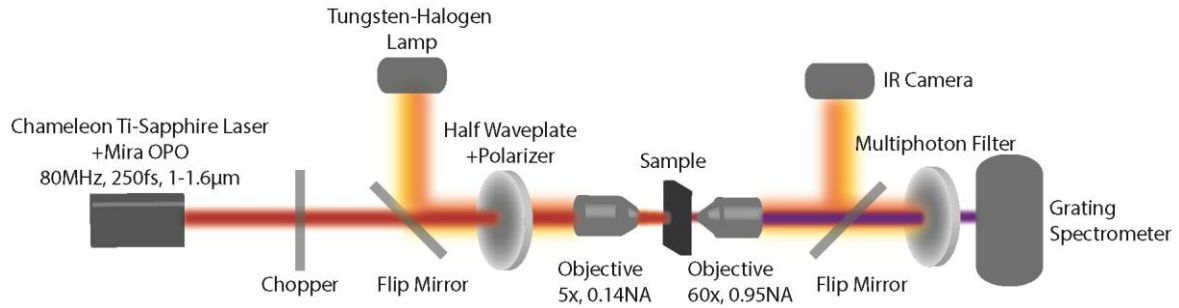
Figure D.1. Schematic of the linear/nonlinear spectroscopic measurement set-up for the investigation of the metasurface.

D.1.2   Absolute THG Efficiency-Measurement from OPO

For the absolute THG efficiency measurement using the OPO, we first applied a large pump intensity (3.2 GW cm^{-2}) on the metasurface, such that the THG signal (~50 nW) could be directly read from a silicon photodetector (Newport 818 series). The absolute THG power from the metasurface was estimated with an additional correction coefficient considering the transmittance of the 0.95 NA objective (84%) and the short-pass filter (95%).

This high power measurement was then used as a reference to calibrate a photo-multiplier tube (PMT) that was used for THG power measurements under relatively low pump intensity. The PMT was connected to a lock-in amplifier and a chopper for better signal-to-noise ratio.
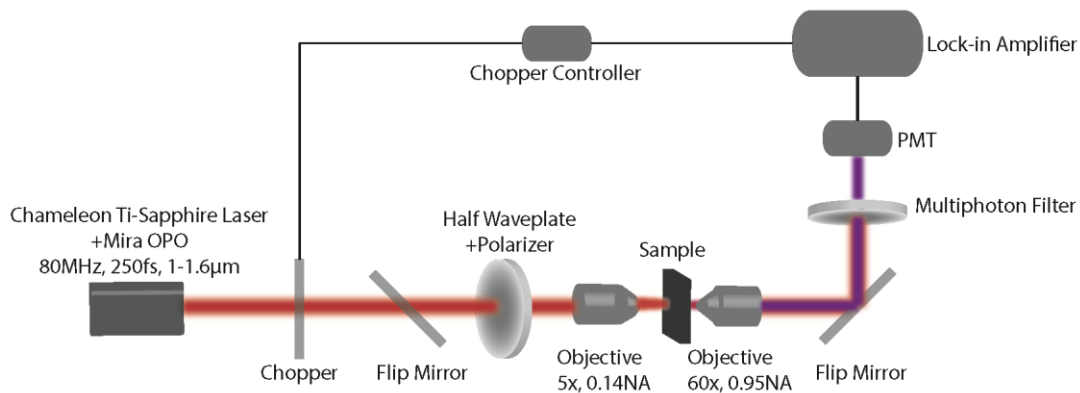
Figure D.2. Schematic of the absolute THG efficiency measurement set-up with OPO.

D.1.3   Absolute THG Efficiency-Measurement from OPA

The laser source for the 1 kHz THG measurements is based on a Ti:Sapphire oscillator (Micra, Coherent) with its output seeded a Ti:Sapphire Coherent Legend (USP-HE) amplifier, operating at 1 kHz repetition rate. The Legend amplifier provides pulses centered at 800 nm, with 40 fs duration and 2.2 mJ energy per pulse. The output of the Legend amplifier was used to generate tunable pulses (250-2500 nm) in an optical parametric amplifier (TOPAS, Coherent). To align the laser wavelength with the Fano resonance of the metasurface, the TOPAS output signal was tuned to be centered at 1350 nm. Using a 0.14 NA microscope objective, the 1350 nm pump was focused on the sample to ~20 μm spot size. After the sample, the THG was collected in the forward direction using a second objective microscope (Nikon Plan Apo Lambda, 60x, 0.95 NA) and focused onto the slit entrance of a spectrometer (Shamrock 303i, Andor) coupled with an EM-CCD (Newton, Andor). A short-pass filter (cut-off at 790 nm) was used to reject pump photons before detection. In order to control the pump fluence, a half wave-plate placed before the polarizer was used. For each pump power, THG signal was

collected for 25 seconds. In order to convert THG intensity into energy and overcome loses in the detection system; the power equivalence of each CCD count was determined by measuring the power of a laser beam before sending it to the detector.
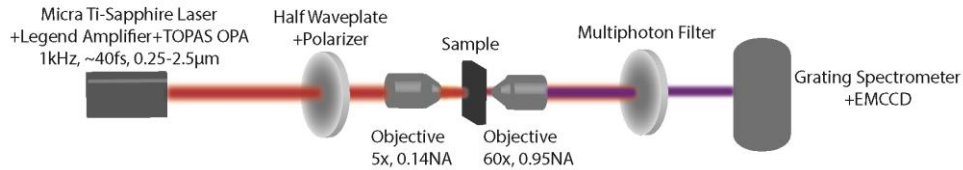
Figure D.3. Schematic of the absolute THG efficiency measurement set-up with OPA.

D.2 Device Performance versus Incident Angle

The simulated angle-dependent linear transmittance of the metasurface for both s- and p- polarized light is presented in Fig. D.4. The range of incident angles (0° to 8°) was chosen to match the numerical aperture of the objective lens on the illumination side.

It can be observed that the spectral response of the metasurface is strongly dependent on the incident angle and the dependence is drastically different for s- and p-polarized incident light. For s-polarized light, the excitation of the "bright" electric dipole resonance is unaltered as the incident electric field is parallel to the metasurface layer. However, the out-of-plane incident magnetic field leads to stronger coupling from free-space to the "dark" magnetic dipole leading to an increased radiative loss and reduced Q-factor. For p-polarized light, the incident electric field is gradually rotated out-of-plane, resulting in a frequency mismatch between the electric and magnetic dipole resonance leading to gradual damping of the Fano resonance.
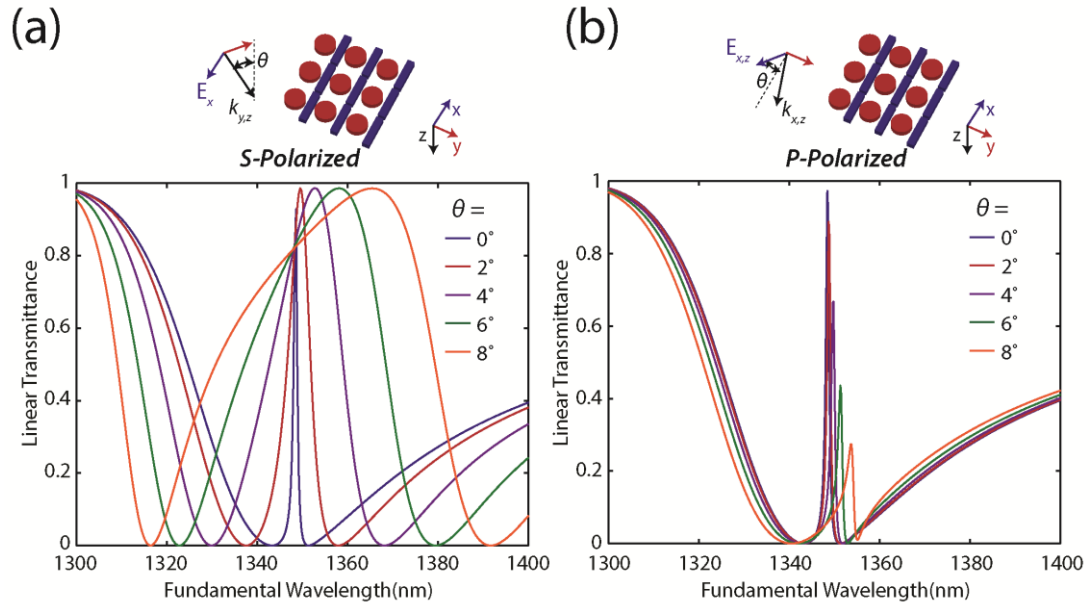
Figure D.4. Simulated Linear transmittance of the metasurface as a function of incident angle for (a) s- and (b) p-polarized light.

Bibliography

[1]   D. R. Smith, J. B. Pendry, and M. C. K. Wiltshire, "Metamaterials and negative refractive index.," *Science*, vol. 305, no. 5685, pp. 788–92, Aug. 2004.

[2]   V. M. Shalaev, W. Cai, U. K. Chettiar, H.-K. Yuan, A. K. Sarychev, V. P. Drachev, and A. V. Kildishev, "Negative index of refraction in optical metamaterials," *Opt. Lett.*, vol. 30, no. 24, p. 3356, 2005.

[3]   J. Valentine, S. Zhang, T. Zentgraf, E. Ulin-Avila, D. A. Genov, G. Bartal, and X. Zhang, "Three-dimensional optical metamaterial with a negative refractive index.," *Nature*, vol. 455, no. 7211, pp. 376–9, Sep. 2008.

[4]   N. Fang, H. Lee, C. Sun, and X. Zhang, "Sub-diffraction-limited optical imaging with a silver superlens.," *Science*, vol. 308, no. 5721, pp. 534–7, Apr. 2005.

[5]   Z. Jacob, L. V. Alekseyev, and E. Narimanov, "Optical Hyperlens: Far-field imaging beyond the diffraction limit," *Opt. Express*, vol. 14, no. 18, p. 8247, Sep. 2006.

[6]   Z. Liu, H. Lee, Y. Xiong, C. Sun, and X. Zhang, "Far-field optical hyperlens magnifying sub-diffraction-limited objects.," *Science*, vol. 315, no. 5819, p. 1686, Mar. 2007.

[7]   D. Schurig, J. J. Mock, B. J. Justice, S. A. Cummer, J. B. Pendry, A. F. Starr, and D. R. Smith, "Metamaterial electromagnetic cloak at microwave frequencies.," *Science*, vol. 314, no. 5801, pp. 977–80, Nov. 2006.

[8]   R. Liu, C. Ji, J. J. Mock, J. Y. Chin, T. J. Cui, and D. R. Smith, "Broadband ground-plane cloak.," *Science*, vol. 323, no. 5912, pp. 366–9, Jan. 2009.

[9]   J. Valentine, J. Li, T. Zentgraf, G. Bartal, and X. Zhang, "An optical cloak made of dielectrics.," *Nat. Mater.*, vol. 8, no. 7, pp. 568–71, Jul. 2009.

[10]   T. Ergin, N. Stenger, P. Brenner, J. B. Pendry, and M. Wegener, "Three-dimensional invisibility cloak at optical wavelengths.," *Science*, vol. 328, no. 5976, pp. 337–9, Apr. 2010.

[11]   V. G. Veselago, "The electrodynamics of substances with simultaneously negative values of ε and μ," *Physics-Uspekhi*, vol. 10, no. 4, pp. 509–514, Apr. 1968.

[12]   J. B. Pendry, A. J. Holden, D. J. Robbins, and W. J. Stewart, "Low frequency plasmons in thin-wire structures," *J. Phys. Condens. Matter*, vol. 10, no. 22, pp. 4785–4809, Jun. 1998.

[13] J. B. Pendry, A. J. Holden, D. J. Robbins, and W. J. Stewart, "Magnetism from conductors and enhanced nonlinear phenomena," *IEEE Trans. Microw. Theory Tech.*, vol. 47, no. 11, pp. 2075–2084, 1999.

[14] D. Smith, W. Padilla, D. Vier, S. Nemat-Nasser, and S. Schultz, "Composite Medium with Simultaneously Negative Permeability and Permittivity," *Phys. Rev. Lett.*, vol. 84, no. 18, pp. 4184–4187, May 2000.

[15] J. B. Pendry, A. J. Holden, D. J. Robbins, and W. J. Stewart, "Magnetism from conductors and enhanced nonlinear phenomena," *IEEE Trans. Microw. Theory Tech.*, vol. 47, no. 11, pp. 2075–2084, 1999.

[16] N. Katsarakis, G. Konstantinidis, A. Kostopoulos, R. S. Penciu, T. F. Gundogdu, M. Kafesaki, E. N. Economou, T. Koschny, and C. M. Soukoulis, "Magnetic response of split-ring resonators in the far-infrared frequency regime," *Opt. Lett.*, vol. 30, no. 11, p. 1348, Jun. 2005.

[17] G. Dolling, C. Enkrich, M. Wegener, J. F. Zhou, C. M. Soukoulis, and S. Linden, "Cut-wire pairs and plate pairs as magnetic atoms for optical metamaterials," *Opt. Lett.*, vol. 30, no. 23, p. 3198, 2005.

[18] C. M. Soukoulis and M. Wegener, "Past achievements and future challenges in the development of three-dimensional photonic metamaterials," *Nat. Photonics*, vol. 5, pp. 523–530, Jul. 2011.

[19] D. Schurig, J. J. Mock, B. J. Justice, S. A. Cummer, J. B. Pendry, A. F. Starr, and D. R. Smith, "Metamaterial electromagnetic cloak at microwave frequencies.," *Science*, vol. 314, no. 5801, pp. 977–80, Nov. 2006.

[20] D. Liang, J. Gu, J. Han, Y. Yang, S. Zhang, and W. Zhang, "Robust large dimension terahertz cloaking.," *Adv. Mater.*, vol. 24, no. 7, pp. 916–921, Feb. 2012.

[21] E. Plum, V. A. Fedotov, and N. I. Zheludev, "Optical activity in extrinsically chiral metamaterial," *Appl. Phys. Lett.*, vol. 93, no. 19, p. 191911, Nov. 2008.

[22] C. Wu, N. Arju, G. Kelp, J. A. Fan, J. Dominguez, E. Gonzales, E. Tutuc, I. Brener, and G. Shvets, "Spectrally selective chiral silicon metasurfaces based on infrared Fano resonances," *Nat. Commun.*, vol. 5, May 2014.

[23] N. Yu, P. Genevet, M. a. Kats, F. Aieta, J.-P. Tetienne, F. Capasso, and Z. Gaburro, "Light Propagation with Phase Discontinuities: Generalized Laws of Reflection and Refraction," *Science (80-.).*, vol. 334, no. 6054, pp. 333–337, Sep. 2011.

[24] N. Yu, F. Aieta, P. Genevet, M. a Kats, Z. Gaburro, and F. Capasso, "A broadband, background-free quarter-wave plate based on plasmonic metasurfaces.," *Nano Lett.*, vol. 12, no. 12, pp. 6328–6333, Dec. 2012.

[25] L. Huang, X. Chen, H. Mühlenbernd, H. Zhang, S. Chen, B. Bai, Q. Tan, G. Jin, K.-W. Cheah, C.-W. Qiu, J. Li, T. Zentgraf, and S. Zhang, "Three-dimensional optical holography using a plasmonic metasurface," *Nat. Commun.*, vol. 4, Nov. 2013.

[26] X. Yin, Z. Ye, J. Rho, Y. Wang, and X. Zhang, "Photonic spin Hall effect at metasurfaces.," *Science*, vol. 339, no. 6126, pp. 1405–7, Mar. 2013.

[27] N. Meinzer, W. L. Barnes, and I. R. Hooper, "Plasmonic meta-atoms and metasurfaces," *Nat. Photonics*, vol. 8, no. 12, pp. 889–898, Nov. 2014.

[28] J. A. Fan, C. Wu, K. Bao, J. Bao, R. Bardhan, N. J. Halas, V. N. Manoharan, P. Nordlander, G. Shvets, and F. Capasso, "Self-assembled plasmonic nanoparticle clusters.," *Science*, vol. 328, no. 5982, pp. 1135–8, May 2010.

[29] N. Liu, L. Langguth, T. Weiss, J. Kästel, M. Fleischhauer, T. Pfau, and H. Giessen, "Plasmonic analogue of electromagnetically induced transparency at the Drude damping limit.," *Nat. Mater.*, vol. 8, no. 9, pp. 758–62, Sep. 2009.

[30] B. Luk'yanchuk, N. I. Zheludev, S. A. Maier, N. J. Halas, P. Nordlander, H. Giessen, and C. T. Chong, "The Fano resonance in plasmonic nanostructures and metamaterials.," *Nat. Mater.*, vol. 9, no. 9, pp. 707–15, Sep. 2010.

[31] M. W. Klein, C. Enkrich, M. Wegener, and S. Linden, "Second-harmonic generation from magnetic metamaterials.," *Science (80-.).*, vol. 313, no. 5786, pp. 502–4, Jul. 2006.

[32] H. Aouani, M. Rahmani, M. Navarro-Cía, and S. a Maier, "Third-harmonic-upconversion enhancement from a single semiconductor nanoparticle coupled to a plasmonic antenna.," *Nat. Nanotechnol.*, vol. 9, no. 4, pp. 290–4, Apr. 2014.

[33] M. Ren, B. Jia, J.-Y. Ou, E. Plum, J. Zhang, K. F. MacDonald, A. E. Nikolaenko, J. Xu, M. Gu, and N. I. Zheludev, "Nanostructured plasmonic medium for terahertz bandwidth all-optical switching.," *Adv. Mater.*, vol. 23, no. 46, pp. 5540–4, Dec. 2011.

[34] H. Suchowski, K. O'Brien, Z. J. Wong, A. Salandrino, X. Yin, and X. Zhang, "Phase mismatch-free nonlinear propagation in optical zero-index materials.," *Science (80-.).*, vol. 342, no. 6163, pp. 1223–6, Dec. 2013.

[35] D. R. Smith, J. B. Pendry, and M. C. K. Wiltshire, "Metamaterials and negative refractive index.," *Science*, vol. 305, no. 5685, pp. 788–92, Aug. 2004.

[36] V. M. Shalaev, W. Cai, U. K. Chettiar, H.-K. Yuan, A. K. Sarychev, V. P. Drachev, and A. V. Kildishev, "Negative index of refraction in optical metamaterials," *Opt. Lett.*, vol. 30, no. 24, p. 3356, 2005.

[37] S. Xiao, V. P. Drachev, A. V Kildishev, X. Ni, U. K. Chettiar, H.-K. Yuan, and V. M. Shalaev, "Loss-free and active optical negative-index metamaterials.," *Nature*, vol. 466, no. 7307, pp. 735–8, Aug. 2010.

[38] J. Zhou, T. Koschny, M. Kafesaki, E. Economou, J. Pendry, and C. Soukoulis, "Saturation of the Magnetic Response of Split-Ring Resonators at Optical Frequencies," *Phys. Rev. Lett.*, vol. 95, no. 22, p. 223902, Nov. 2005.

[39] L. Lewin, "The electrical constants of a material loaded with spherical particles," *Proc. Inst. Elec. Eng., Part 3*, vol. 94, pp. 65–68, 1947.

[40] Q. Zhao, J. Zhou, F. Zhang, and D. Lippens, "Mie resonance-based dielectric metamaterials," *Mater. Today*, vol. 12, no. 12, pp. 60–69, Dec. 2009.

[41] S. O'Brien and J. B. Pendry, "Photonic band-gap effects and magnetic activity in dielectric composites," *Journal of Physics: Condensed Matter*, vol. 14, no. 15. pp. 4035–4044, 2002.

[42] L. Peng, L. Ran, H. Chen, H. Zhang, J. Kong, and T. Grzegorczyk, "Experimental Observation of Left-Handed Behavior in an Array of Standard Dielectric Resonators," *Phys. Rev. Lett.*, vol. 98, no. 15, p. 157403, Apr. 2007.

[43] B.-I. Popa and S. Cummer, "Compact Dielectric Particles as a Building Block for Low-Loss Magnetic Metamaterials," *Phys. Rev. Lett.*, vol. 100, no. 20, p. 207401, May 2008.

[44] J. Ginn, I. Brener, D. Peters, J. Wendt, J. Stevens, P. Hines, L. Basilio, L. Warne, J. Ihlefeld, P. Clem, and M. Sinclair, "Realizing Optical Magnetism from Dielectric Metamaterials," *Phys. Rev. Lett.*, vol. 108, no. 9, p. 097402, Feb. 2012.

[45] J. Ginn, I. Brener, D. Peters, J. Wendt, J. Stevens, P. Hines, L. Basilio, L. Warne, J. Ihlefeld, P. Clem, and M. Sinclair, "Realizing Optical Magnetism from Dielectric Metamaterials," *Phys. Rev. Lett.*, vol. 108, no. 9, Feb. 2012.

[46] A. E. Miroshnichenko and Y. S. Kivshar, "Fano resonances in all-dielectric oligomers.," *Nano Lett.*, vol. 12, no. 12, pp. 6459–63, Dec. 2012.

[47] S. Enoch, G. Tayeb, P. Sabouroux, N. Guérin, and P. Vincent, "A Metamaterial for Directive Emission," *Phys. Rev. Lett.*, vol. 89, no. 21, Nov. 2002.

[48] R. Ziolkowski, "Propagation in and scattering from a matched metamaterial having a zero index of refraction," *Phys. Rev. E*, vol. 70, no. 4, p. 046608, Oct. 2004.

[49] A. Alù, M. Silveirinha, A. Salandrino, and N. Engheta, "Epsilon-near-zero metamaterials and electromagnetic sources: Tailoring the radiation phase pattern," *Phys. Rev. B*, vol. 75, no. 15, p. 155410, Apr. 2007.

[50] M. Silveirinha and N. Engheta, "Tunneling of Electromagnetic Energy through Subwavelength Channels and Bends using ε-Near-Zero Materials," *Phys. Rev. Lett.*, vol. 97, no. 15, Oct. 2006.

[51] J. Bravo-Abad, J. D. Joannopoulos, and M. Soljačić, "Enabling single-mode behavior over large areas with photonic Dirac cones.," *Proc. Natl. Acad. Sci. U. S. A.*, vol. 109, no. 25, pp. 9761–5, Jun. 2012.

[52] J. Hao, W. Yan, and M. Qiu, "Super-reflection and cloaking based on zero index metamaterial," *Appl. Phys. Lett.*, vol. 96, no. 10, p. 101109, Mar. 2010.

[53] R. Liu, Q. Cheng, T. Hand, J. Mock, T. Cui, S. Cummer, and D. Smith, "Experimental Demonstration of Electromagnetic Tunneling Through an Epsilon-Near-Zero Metamaterial at Microwave Frequencies," *Phys. Rev. Lett.*, vol. 100, no. 2, Jan. 2008.

[54] D. Adams, S. Inampudi, T. Ribaudo, D. Slocum, S. Vangala, N. Kuhta, W. Goodhue, V. Podolskiy, and D. Wasserman, "Funneling Light through a Subwavelength Aperture with Epsilon-Near-Zero Materials," *Phys. Rev. Lett.*, vol. 107, no. 13, p. 133901, Sep. 2011.

[55] E. Vesseur, T. Coenen, H. Caglayan, N. Engheta, and A. Polman, "Experimental Verification of n=0 Structures for Visible Light," *Phys. Rev. Lett.*, vol. 110, no. 1, p. 013902, Jan. 2013.

[56] L. Lewin, "The electrical constants of a material loaded with spherical particles," *Proc. Inst. Elec. Eng., Part 3*, vol. 94, pp. 65–68, 1947.

[57] Q. Zhao, L. Kang, B. Du, H. Zhao, Q. Xie, X. Huang, B. Li, J. Zhou, and L. Li, "Experimental Demonstration of Isotropic Negative Permeability in a Three-Dimensional Dielectric Composite," *Phys. Rev. Lett.*, vol. 101, no. 2, p. 027402, Jul. 2008.

[58] A. I. Kuznetsov, A. E. Miroshnichenko, Y. H. Fu, J. Zhang, and B. Luk'yanchuk, "Magnetic light.," *Sci. Rep.*, vol. 2, p. 492, Jan. 2012.

[59] L. Shi, T. U. Tuzer, R. Fenollosa, and F. Meseguer, "A New Dielectric Metamaterial Building Block with a Strong Magnetic Response in the Sub-1.5-Micrometer Region: Silicon Colloid Nanocavities.," *Adv. Mater.*, vol. 24, no. 44, pp. 5934–5938, Aug. 2012.

[60] X. Huang, Y. Lai, Z. H. Hang, H. Zheng, and C. T. Chan, "Dirac cones induced by accidental degeneracy in photonic crystals and zero-refractive-index materials.," *Nat. Mater.*, vol. 10, no. 8, pp. 582–586, Aug. 2011.

[61] K. S. Novoselov, A. K. Geim, S. V Morozov, D. Jiang, M. I. Katsnelson, I. V Grigorieva, S. V Dubonos, and A. A. Firsov, "Two-dimensional gas of massless Dirac fermions in graphene.," *Nature*, vol. 438, no. 7065, pp. 197–200, Nov. 2005.

[62] I. Tsukerman, "Effective parameters of metamaterials: a rigorous homogenization theory via Whitney interpolation," *J. Opt. Soc. Am. B*, vol. 28, no. 3, p. 577, Feb. 2011.

[63] Y. Wu, J. Li, Z.-Q. Zhang, and C. Chan, "Effective medium theory for magnetodielectric composites: Beyond the long-wavelength limit," *Phys. Rev. B*, vol. 74, no. 8, Aug. 2006.

[64] X. Chen, T. Grzegorczyk, and B. Wu, "Robust method to retrieve the constitutive effective parameters of metamaterials," *Phys. Rev. E*, vol. 70, no. 1, p. 016608, Jul. 2004.

[65] D. R. Smith, D. C. Vier, T. Koschny, and C. M. Soukoulis, "Electromagnetic parameter retrieval from inhomogeneous metamaterials," *Phys. Rev. E*, vol. 71, no. 3, p. 036617, Mar. 2005.

[66] M. Born and E. Wolf, *Principle of optics*, 7th ed. Cambridge University Press, 1999.

[67] J. Huang and J. A. Encinar, *Reflectarray Antennas*. John Wiley & Sons, 2007.

[68] D. Berry, R. Malech, and W. Kennedy, "The reflectarray antenna," *IEEE Trans. Antennas Propag.*, vol. 11, no. 6, pp. 645–651, Nov. 1963.

[69] L. Huang, X. Chen, H. Mühlenbernd, G. Li, B. Bai, Q. Tan, G. Jin, T. Zentgraf, and S. Zhang, "Dispersionless phase discontinuities for controlling light propagation.," *Nano Lett.*, vol. 12, no. 11, pp. 5750–5755, Nov. 2012.

[70] X. Ni, N. K. Emani, A. V Kildishev, A. Boltasseva, and V. M. Shalaev, "Broadband light bending with plasmonic nanoantennas.," *Science (80-.).*, vol. 335, no. 6067, p. 427, Jan. 2012.

[71] S. Sun, K.-Y. Yang, C.-M. Wang, T.-K. Juan, W. T. Chen, C. Y. Liao, Q. He, S. Xiao, W.-T. Kung, G.-Y. Guo, L. Zhou, and D. P. Tsai, "High-efficiency broadband anomalous reflection by gradient meta-surfaces.," *Nano Lett.*, vol. 12, no. 12, pp. 6223–6229, Dec. 2012.

[72] S. Sun, Q. He, S. Xiao, Q. Xu, X. Li, and L. Zhou, "Gradient-index meta-surfaces as a bridge linking propagating waves and surface waves.," *Nat. Mater.*, vol. 11, no. 5, pp. 426–431, May 2012.

[73] N. K. Grady, J. E. Heyes, D. R. Chowdhury, Y. Zeng, M. T. Reiten, A. K. Azad, A. J. Taylor, D. a R. Dalvit, and H.-T. Chen, "Terahertz metamaterials for linear polarization conversion and anomalous refraction.," *Science (80-.).*, vol. 340, no. 6138, pp. 1304–1307, Jun. 2013.

[74] F. Aieta, P. Genevet, M. A. Kats, N. Yu, R. Blanchard, Z. Gaburro, and F. Capasso, "Aberration-Free Ultrathin Flat Lenses and Axicons at Telecom Wavelengths Based on Plasmonic Metasurfaces.," *Nano Lett.*, vol. 12, no. 9, pp. 4932–4936, 2012.

[75] X. Ni, S. Ishii, A. V Kildishev, and V. M. Shalaev, "Ultra-thin, planar, Babinet-inverted plasmonic metalenses," *Light Sci. Appl.*, vol. 2, no. 4, p. e72, Apr. 2013.

[76] A. Pors, M. G. Nielsen, R. L. Eriksen, and S. I. Bozhevolnyi, "Broadband Focusing Flat Mirrors Based on Plasmonic Gradient Metasurfaces.," *Nano Lett.*, vol. 13, no. 2, pp. 829–834, 2013.

[77] X. Yin, Z. Ye, J. Rho, Y. Wang, and X. Zhang, "Photonic spin Hall effect at metasurfaces.," *Science (80-.).*, vol. 339, no. 6126, pp. 1405–1407, Mar. 2013.

[78] G. Li, M. Kang, S. Chen, S. Zhang, E. Y.-B. Pun, K. W. Cheah, and J. Li, "Spin-enabled plasmonic metasurfaces for manipulating orbital angular momentum of light.," *Nano Lett.*, vol. 13, no. 9, pp. 4148–4151, Oct. 2013.

[79] C. Pfeiffer and A. Grbic, "Metamaterial huygens' surfaces: tailoring wave fronts with reflectionless sheets.," *Phys. Rev. Lett.*, vol. 110, no. 19, p. 197401, 2013.

[80] F. Monticone, N. M. Estakhri, and A. Alù, "Full Control of Nanoscale Optical Transmission with a Composite Metascreen," *Phys. Rev. Lett.*, vol. 110, no. 20, p. 203903, May 2013.

[81] Y. Zhao and A. Alù, "Tailoring the dispersion of plasmonic nanorods to realize broadband optical meta-waveplates.," *Nano Lett.*, vol. 13, no. 3, pp. 1086–91, Mar. 2013.

[82] A. Pors, O. Albrektsen, I. P. Radko, and S. I. Bozhevolnyi, "Gap plasmon-based metasurfaces for total control of reflected light.," *Sci. Rep.*, vol. 3, p. 2155, Jan. 2013.

[83] Q. Zhao, J. Zhou, F. Zhang, and D. Lippens, "Mie resonance-based dielectric metamaterials," *Mater. Today*, vol. 12, no. 12, pp. 60–69, Dec. 2009.

[84] P. Moitra, Y. Yang, Z. Anderson, I. I. Kravchenko, D. P. Briggs, and J. Valentine, "Realization of an all-dielectric zero-index optical metamaterial," *Nat. Photonics*, vol. 7, no. 10, pp. 791–795, Aug. 2013.

[85] I. Staude, A. E. Miroshnichenko, M. Decker, N. T. Fofang, S. Liu, E. Gonzales, J. Dominguez, T. S. Luk, D. N. Neshev, I. Brener, and Y. Kivshar, "Tailoring directional scattering through magnetic and electric resonances in subwavelength silicon nanodisks," *ACS Nano*, vol. 7, no. 9, pp. 7824–7832, 2013.

[86] M. C. Y. Huang, Y. Zhou, and C. J. Chang-Hasnain, "A surface-emitting laser incorporating a high-index-contrast subwavelength grating," *Nat. Photonics*, vol. 1, no. 2, pp. 119–122, Feb. 2007.

[87] M. Mutlu, A. E. Akosman, G. Kurt, M. Gokkavas, and E. Ozbay, "Experimental realization of a high-contrast grating based broadband quarter-wave plate.," *Opt. Express*, vol. 20, no. 25, pp. 27966–27973, Dec. 2012.

[88] F. Lu, F. G. Sedgwick, V. Karagodsky, C. Chase, and C. J. Chang-Hasnain, "Planar high-numerical-aperture low-loss focusing reflectors and lenses using subwavelength high contrast gratings.," *Opt. Express*, vol. 18, no. 12, pp. 12606–12614, Jun. 2010.

[89] D. Fattal, J. Li, Z. Peng, M. Fiorentino, and R. G. Beausoleil, "Flat dielectric grating reflectors with focusing abilities," *Nat. Photonics*, vol. 4, no. 7, pp. 466–470, 2010.

[90] G. Biener, A. Niv, V. Kleiner, and E. Hasman, "Formation of helical beams by use of Pancharatnam-Berry phase optical elements," *Opt. Lett.*, vol. 27, no. 21, pp. 1875–1877, Nov. 2002.

[91] P. Lalanne, S. Astilean, and P. Chavel, "Blazed binary subwavelength gratings with efficiencies larger echelette gratings than those of conventional echelette gratings," *Opt. Lett.*, vol. 23, no. 14, pp. 1081–1083, 1998.

[92] P. Lalanne, S. Astilean, P. Chavel, E. Cambril, and H. Launois, "Design and fabrication of blazed binary diffractive elements with sampling periods smaller than the structural cutoff," *J. Opt. Soc. Am. A*, vol. 16, no. 5, p. 1143, 1999.

[93] C. Sauvan, P. Lalanne, and M.-S. L. Lee, "Broadband blazing with artificial dielectrics," *Opt. Lett.*, vol. 29, no. 14, p. 1593, 2004.

[94] L. Allen, M. Beijersbergen, R. Spreeuw, and J. Woerdman, "Orbital angular momentum of light and the transformation of Laguerre-Gaussian laser modes," *Phys. Rev. A*, vol. 45, no. 11, pp. 8185–8189, Jun. 1992.

[95] P. Galajda and P. Ormos, "Complex micromachines produced and driven by light," *Appl. Phys. Lett.*, vol. 78, no. 2, pp. 249–251, Jan. 2001.

[96] G. Molina-Terriza, J. P. Torres, and L. Torner, "Twisted photons," *Nat. Phys.*, vol. 3, no. 5, pp. 305–310, May 2007.

[97] J. Verbeeck, H. Tian, and P. Schattschneider, "Production and application of electron vortex beams.," *Nature*, vol. 467, no. 7313, pp. 301–304, Sep. 2010.

[98] P. Genevet, N. Yu, F. Aieta, J. Lin, M. a. Kats, R. Blanchard, M. O. Scully, Z. Gaburro, and F. Capasso, "Ultra-thin plasmonic optical vortex plate based on phase discontinuities," *Appl. Phys. Lett.*, vol. 100, no. 1, p. 013101, 2012.

[99] X. Cai, J. Wang, M. J. Strain, B. Johnson-Morris, J. Zhu, M. Sorel, J. L. O'Brien, M. G. Thompson, and S. Yu, "Integrated compact optical vortex beam emitters.," *Science (80-.).*, vol. 338, no. 6105, pp. 363–366, Oct. 2012.

[100] S. E. Harris, "Electromagnetically Induced Transparency," *Phys. Today*, vol. 50, no. 7, p. 36, Jan. 1997.

[101] S. Zhang, D. a. Genov, Y. Wang, M. Liu, and X. Zhang, "Plasmon-Induced Transparency in Metamaterials," *Phys. Rev. Lett.*, vol. 101, no. 4, p. 047401, Jul. 2008.

[102] N. Papasimakis, V. Fedotov, N. Zheludev, and S. Prosvirnin, "Metamaterial Analog of Electromagnetically Induced Transparency," *Phys. Rev. Lett.*, vol. 101, no. 25, p. 253903, Dec. 2008.

[103] N. Verellen, Y. Sonnefraud, H. Sobhani, F. Hao, V. V Moshchalkov, P. Van Dorpe, P. Nordlander, and S. a Maier, "Fano resonances in individual coherent plasmonic nanocavities.," *Nano Lett.*, vol. 9, no. 4, pp. 1663–7, Apr. 2009.

[104] R. Singh, C. Rockstuhl, F. Lederer, and W. Zhang, "Coupling between a dark and a bright eigenmode in a terahertz metamaterial," *Phys. Rev. B*, vol. 79, no. 8, p. 085111, Feb. 2009.

[105] P. Tassin, L. Zhang, T. Koschny, E. Economou, and C. Soukoulis, "Low-Loss Metamaterials Based on Classical Electromagnetically Induced Transparency," *Phys. Rev. Lett.*, vol. 102, no. 5, p. 053901, Feb. 2009.

[106] N. Liu, L. Langguth, T. Weiss, J. Kästel, M. Fleischhauer, T. Pfau, and H. Giessen, "Plasmonic analogue of electromagnetically induced transparency at the Drude damping limit.," *Nat. Mater.*, vol. 8, no. 9, pp. 758–762, Sep. 2009.

[107] N. Liu, M. Hentschel, T. Weiss, A. P. Alivisatos, and H. Giessen, "Three-dimensional plasmon rulers.," *Science (80-.).*, vol. 332, no. 6036, pp. 1407–1410, Jun. 2011.

[108] X. Liu, J. Gu, R. Singh, Y. Ma, J. Zhu, Z. Tian, M. He, J. Han, and W. Zhang, "Electromagnetically induced transparency in terahertz plasmonic metamaterials via dual excitation pathways of the dark mode," *Appl. Phys. Lett.*, vol. 100, no. 13, p. 131101, 2012.

[109] J. Gu, R. Singh, X. Liu, X. Zhang, Y. Ma, S. Zhang, S. a Maier, Z. Tian, A. K. Azad, H.-T. Chen, A. J. Taylor, J. Han, and W. Zhang, "Active control of electromagnetically induced transparency analogue in terahertz metamaterials.," *Nat. Commun.*, vol. 3, p. 1151, Jan. 2012.

[110] Q. Xu, S. Sandhu, M. Povinelli, J. Shakya, S. Fan, and M. Lipson, "Experimental Realization of an On-Chip All-Optical Analogue to Electromagnetically Induced Transparency," *Phys. Rev. Lett.*, vol. 96, no. 12, p. 123901, Mar. 2006.

[111] X. Yang, M. Yu, D.-L. Kwong, and C. Wong, "All-Optical Analog to Electromagnetically Induced Transparency in Multiple Coupled Photonic Crystal Cavities," *Phys. Rev. Lett.*, vol. 102, no. 17, p. 173902, Apr. 2009.

[112] N. Papasimakis, V. Fedotov, N. Zheludev, and S. Prosvirnin, "Metamaterial Analog of Electromagnetically Induced Transparency," *Phys. Rev. Lett.*, vol. 101, no. 25, p. 253903, Dec. 2008.

[113] P. Tassin, L. Zhang, T. Koschny, E. Economou, and C. Soukoulis, "Low-Loss Metamaterials Based on Classical Electromagnetically Induced Transparency," *Phys. Rev. Lett.*, vol. 102, no. 5, p. 053901, Feb. 2009.

[114] N. Liu, T. Weiss, M. Mesch, L. Langguth, U. Eigenthaler, M. Hirscher, C. Sönnichsen, and H. Giessen, "Planar metamaterial analogue of electromagnetically induced transparency for plasmonic sensing.," *Nano Lett.*, vol. 10, no. 4, pp. 1103–7, Apr. 2010.

[115] Z.-G. Dong, H. Liu, J.-X. Cao, T. Li, S.-M. Wang, S.-N. Zhu, and X. Zhang, "Enhanced sensing performance by the plasmonic analog of electromagnetically induced transparency in active metamaterials," *Appl. Phys. Lett.*, vol. 97, no. 11, p. 114101, Sep. 2010.

[116] Y. Sun, Y. Tong, C. Xue, Y. Ding, Y. Li, H. Jiang, and H. Chen, "Electromagnetic diode based on nonlinear electromagnetically induced transparency in metamaterials," *Appl. Phys. Lett.*, vol. 103, no. 9, p. 091904, Aug. 2013.

[117] U. Fano, "Effects of Configuration Interaction on Intensities and Phase Shifts," *Phys. Rev.*, vol. 124, no. 6, pp. 1866–1878, Dec. 1961.

[118] B. Luk'yanchuk, N. I. Zheludev, S. a Maier, N. J. Halas, P. Nordlander, H. Giessen, and C. T. Chong, "The Fano resonance in plasmonic nanostructures and metamaterials.," *Nat. Mater.*, vol. 9, no. 9, pp. 707–15, Sep. 2010.

[119] R. Singh, C. Rockstuhl, F. Lederer, and W. Zhang, "Coupling between a dark and a bright eigenmode in a terahertz metamaterial," *Phys. Rev. B*, vol. 79, no. 8, p. 085111, Feb. 2009.

[120] N. Liu, L. Langguth, T. Weiss, J. Kästel, M. Fleischhauer, T. Pfau, and H. Giessen, "Plasmonic analogue of electromagnetically induced transparency at the Drude damping limit.," *Nat. Mater.*, vol. 8, no. 9, pp. 758–762, Sep. 2009.

[121] N. Liu, M. Hentschel, T. Weiss, A. P. Alivisatos, and H. Giessen, "Three-dimensional plasmon rulers.," *Science (80-.).*, vol. 332, no. 6036, pp. 1407–1410, Jun. 2011.

[122] Y. Yang, W. Wang, P. Moitra, I. I. Kravchenko, D. P. Briggs, and J. Valentine, "Dielectric meta-reflectarray for broadband linear polarization conversion and optical vortex generation.," *Nano Lett.*, vol. 14, no. 3, pp. 1394–1399, Mar. 2014.

[123] P. Fan, Z. Yu, S. Fan, and M. L. Brongersma, "Optical Fano resonance of an individual semiconductor nanostructure.," *Nat. Mater.*, vol. 13, no. 5, pp. 471–475, May 2014.

[124] C. Wu, N. Arju, G. Kelp, J. A. Fan, J. Dominguez, E. Gonzales, E. Tutuc, I. Brener, and G. Shvets, "Spectrally selective chiral silicon metasurfaces based on infrared Fano resonances," *Nat. Commun.*, vol. 5, May 2014.

[125] J. Zhang, K. F. MacDonald, and N. I. Zheludev, "Near-infrared trapped mode magnetic resonance in an all-dielectric metamaterial.," *Opt. Express*, vol. 21, no. 22, pp. 26721–26728, Nov. 2013.

[126] V. a. Fedotov, N. Papasimakis, E. Plum, a. Bitzer, M. Walther, P. Kuo, D. P. Tsai, and N. I. Zheludev, "Spectral Collapse in Ensembles of Metamolecules," *Phys. Rev. Lett.*, vol. 104, no. 22, p. 223901, Jun. 2010.

[127] S. D. Jenkins and J. Ruostekoski, "Metamaterial Transparency Induced by Cooperative Electromagnetic Interactions," *Phys. Rev. Lett.*, vol. 111, no. 14, p. 147401, Sep. 2013.

[128] T. S. Kao, S. D. Jenkins, J. Ruostekoski, and N. I. Zheludev, "Coherent Control of Nanoscale Light Localization in Metamaterial: Creating and Positioning Isolated Subwavelength Energy Hot Spots," *Phys. Rev. Lett.*, vol. 106, no. 8, p. 085501, Feb. 2011.

[129] S. D. Jenkins and J. Ruostekoski, "Theoretical formalism for collective electromagnetic response of discrete metamaterial systems," *Phys. Rev. B*, vol. 86, no. 8, p. 085116, Aug. 2012.

[130] G. Adamo, J. Y. Ou, J. K. So, S. D. Jenkins, F. De Angelis, K. F. MacDonald, E. Di Fabrizio, J. Ruostekoski, and N. I. Zheludev, "Electron-Beam-Driven Collective-Mode Metamaterial Light Source," *Phys. Rev. Lett.*, vol. 109, no. 21, p. 217401, Nov. 2012.

[131] M. M. Burns, J.-M. Fournier, and J. A. Golovchenko, "Optical binding," *Phys. Rev. Lett.*, vol. 63, no. 12, pp. 1233–1236, Sep. 1989.

[132] H. A. Haus, *Waves and Fields in Optoelectronics*. New Jersey: Prentice Hall, 1983.

[133] S. Fan, W. Suh, and J. D. Joannopoulos, "Temporal coupled-mode theory for the Fano resonance in optical resonators," *J. Opt. Soc. Am. A*, vol. 20, no. 3, p. 569, 2003.

[134] V. a. Fedotov, N. Papasimakis, E. Plum, a. Bitzer, M. Walther, P. Kuo, D. P. Tsai, and N. I. Zheludev, "Spectral Collapse in Ensembles of Metamolecules," *Phys. Rev. Lett.*, vol. 104, no. 22, p. 223901, Jun. 2010.

[135] S. D. Jenkins and J. Ruostekoski, "Metamaterial Transparency Induced by Cooperative Electromagnetic Interactions," *Phys. Rev. Lett.*, vol. 111, no. 14, p. 147401, Sep. 2013.

[136] K. J. Vahala, "Optical microcavities.," *Nature*, vol. 424, no. 6950, pp. 839–846, Aug. 2003.

[137] Y. Akahane, T. Asano, B.-S. Song, and S. Noda, "High-Q photonic nanocavity in a two-dimensional photonic crystal.," *Nature*, vol. 425, no. 6961, pp. 944–947, Oct. 2003.

[138] S. Fan and J. Joannopoulos, "Analysis of guided resonances in photonic crystal slabs," *Phys. Rev. B*, vol. 65, no. 23, p. 235112, Jun. 2002.

[139] J. N. Anker, W. P. Hall, O. Lyandres, N. C. Shah, J. Zhao, and R. P. Van Duyne, "Biosensing with plasmonic nanosensors.," *Nat. Mater.*, vol. 7, no. 6, pp. 442–453, Jun. 2008.

[140] S. Zhang, K. Bao, N. J. Halas, H. Xu, and P. Nordlander, "Substrate-induced Fano resonances of a plasmonic nanocube: a route to increased-sensitivity localized surface plasmon resonance sensors revealed.," *Nano Lett.*, vol. 11, no. 4, pp. 1657–1663, Apr. 2011.

[141] J. N. Anker, W. P. Hall, O. Lyandres, N. C. Shah, J. Zhao, and R. P. Van Duyne, "Biosensing with plasmonic nanosensors.," *Nat. Mater.*, vol. 7, no. 6, pp. 442–453, Jun. 2008.

[142] R. Boyd, *Nonlinear Optics*. Academic Press, 1992.

[143] V. R. Almeida, C. A. Barrios, R. R. Panepucci, and M. Lipson, "All-optical control of light on a silicon chip.," *Nature*, vol. 431, no. 7012, pp. 1081–4, Oct. 2004.

[144] M. Abb, P. Albella, J. Aizpurua, and O. L. Muskens, "All-optical control of a single plasmonic nanoantenna-ITO hybrid.," *Nano Lett.*, vol. 11, no. 6, pp. 2457–63, Jun. 2011.

[145] M. Kauranen and A. V Zayats, "Nonlinear plasmonics," *Nat. Photonics*, vol. 6, no. October, pp. 737–748, 2012.

[146] B. Metzger, T. Schumacher, M. Hentschel, and M. Lippitz, "Third Harmonic Mechanism in Complex Plasmonic Fano Structures," *ACS Photonics*, vol. 1, pp. 471–476, 2014.

[147] J. B. Lassiter, X. Chen, X. Liu, T. B. Hoang, S. Oh, M. H. Mikkelsen, and D. R. Smith, "Third-Harmonic Generation Enhancement by Film-Coupled Plasmonic Stripe Resonators," *ACS Photonics*, vol. 1, pp. 1212–1217, 2014.

[148] J. Lee, M. Tymchenko, C. Argyropoulos, P.-Y. Chen, F. Lu, F. Demmerle, G. Boehm, M.-C. Amann, A. Alù, and M. A. Belkin, "Giant nonlinear response from plasmonic metasurfaces coupled to intersubband transitions.," *Nature*, vol. 511, no. 7507, pp. 65–9, Jul. 2014.

[149] D. McMorrow, W. T. Lotshaw, J. S. Melinger, S. Buchner, and R. L. Pease, "Subbandgap laser-induced single event effects: carrier generation via two-photon absorption," *IEEE Trans. Nucl. Sci.*, vol. 49, no. 6, pp. 3002–3008, Dec. 2002.

[150] M. T. Rakher, L. Ma, O. Slattery, X. Tang, and K. Srinivasan, "Quantum transduction of telecommunications-band single photons from a quantum dot by frequency upconversion," *Nat. Photonics*, vol. 4, no. 11, pp. 786–791, Oct. 2010.

[151] W. Fan, S. Zhang, N. Panoiu, A. Abdenour, S. Krishna, R. M. Osgood, K. J. Malloy, and S. R. J. Brueck, "Second Harmonic Generation from a Nanopatterned Isotropic Nonlinear Material," *Nano Lett.*, vol. 6, pp. 1027–1030, 2006.

[152] B. Metzger, M. Hentschel, T. Schumacher, M. Lippitz, X. Ye, C. B. Murray, B. Knabe, K. Buse, and H. Giessen, "Doubling the efficiency of third harmonic generation by positioning ITO nanocrystals into the hot-spot of plasmonic gap-antennas," *Nano Lett.*, vol. 14, pp. 2867–2872, 2014.

[153] M. R. Shcherbakov, D. N. Neshev, B. Hopkins, A. S. Shorokhov, I. Staude, E. V Melik-gaykazyan, M. Decker, A. A. Ezhov, A. E. Miroshnichenko, I. Brener, A. A. Fedyanin, and Y. S. Kivshar, "Enhanced third-harmonic generation in silicon nanoparticles driven by magnetic response," *Nano Lett.*, vol. 14, no. 11, pp. 6488–6492, 2014.

[154] T. G. Habteyes, I. Staude, K. E. Chong, J. Dominguez, M. Decker, A. Miroshnichenko, Y. Kivshar, and I. Brener, "Near-Field Mapping of Optical

Modes on All-Dielectric Silicon Nanodisks," *ACS Photonics*, vol. 1, no. 9, pp. 794–798, Sep. 2014.

[155] B. Corcoran, C. Monat, C. Grillet, D. J. Moss, B. J. Eggleton, T. P. White, L. O. Faolain, and T. F. Krauss, "Green light emission in silicon through slow-light enhanced third-harmonic generation in photonic- crystal waveguides," *Nat. Photonics*, vol. 3, no. April, pp. 206–210, 2009.

[156] J. S. Levy, M. A. Foster, A. L. Gaeta, and M. Lipson, "Harmonic generation in silicon nitride ring resonators," *Opt. Express*, vol. 19, no. 12, pp. 4881–4887, 2011.

[157] U. Fano, "Effects of Configuration Interaction on Intensities and Phase Shifts," *Phys. Rev.*, vol. 124, no. 6, pp. 1866–1878, Dec. 1961.

[158] A. E. Miroshnichenko, S. Flach, and Y. S. Kivshar, "Fano resonances in nanoscale structures," *Rev. Mod. Phys.*, vol. 82, no. 3, pp. 2257–2298, Aug. 2010.

[159] J. Leuthold, C. Koos, and W. Freude, "Nonlinear silicon photonics," *Nat. Photonics*, vol. 4, no. 8, pp. 535–544, Jul. 2010.

[160] V. a. Fedotov, N. Papasimakis, E. Plum, a. Bitzer, M. Walther, P. Kuo, D. P. Tsai, and N. I. Zheludev, "Spectral Collapse in Ensembles of Metamolecules," *Phys. Rev. Lett.*, vol. 104, no. 22, p. 223901, Jun. 2010.

[161] A. O. Pinchuk and G. C. Schatz, "Collective surface plasmon resonance coupling in silver nanoshell arrays," *Appl. Phys. B*, vol. 93, no. 1, pp. 31–38, Aug. 2008.

[162] Y. Yang, I. I. Kravchenko, D. P. Briggs, and J. Valentine, "All-dielectric metasurface analogue of electromagnetically induced transparency," *Nat. Commun.*, vol. 5, p. 5753, Dec. 2014.

[163] R. Boyd, "Nonlinear Optical Materials," in *Encyclopedia of Materials: Science and Technology*, 2001, pp. 6237–6244.

[164] V. Raghunathan, D. Borlaug, R. R. Rice, and B. Jalali, "Demonstration of a Mid-infrared silicon Raman amplifier," *Opt. Express*, vol. 15, no. 22, p. 14355, 2007.

[165] H. Rong, R. Jones, A. Liu, O. Cohen, D. Hak, A. Fang, and M. Paniccia, "A continuous-wave Raman silicon laser.," *Nature*, vol. 433, no. 7027, pp. 725–8, Feb. 2005.

[166] J. Y. Ou, E. Plum, L. Jiang, and N. I. Zheludev, "Reconfigurable photonic metamaterials.," *Nano Lett.*, vol. 11, no. 5, pp. 2142–4, May 2011.

[167] H.-T. Chen, W. J. Padilla, J. M. O. Zide, A. C. Gossard, A. J. Taylor, and R. D. Averitt, "Active terahertz metamaterial devices.," *Nature*, vol. 444, no. 7119, pp. 597–600, Nov. 2006.

[168] M. J. Dicken, K. Aydin, I. M. Pryce, L. A. Sweatlock, E. M. Boyd, S. Walavalkar, J. Ma, and H. A. Atwater, "Frequency tunable near-infrared metamaterials based on VO2 phase transition.," *Opt. Express*, vol. 17, no. 20, pp. 18330–9, Sep. 2009.

[169] S. H. Lee, M. Choi, T.-T. Kim, S. Lee, M. Liu, X. Yin, H. K. Choi, S. S. Lee, C.-G. Choi, S.-Y. Choi, X. Zhang, and B. Min, "Switching terahertz waves with gate-controlled active graphene metamaterials.," *Nat. Mater.*, vol. 11, no. 11, pp. 936–41, Nov. 2012.

[170] A. Gabbay and I. Brener, "Theory and modeling of electrically tunable metamaterial devices using inter-subband transitions in semiconductor quantum wells.," *Opt. Express*, vol. 20, no. 6, pp. 6584–97, Mar. 2012.

[171] A. Benz, I. Montaño, J. F. Klem, and I. Brener, "Tunable metamaterials based on voltage controlled strong coupling," *Appl. Phys. Lett.*, vol. 103, no. 26, p. 263116, Dec. 2013.

[172] J. Lee, S. Jung, P.-Y. Chen, F. Lu, F. Demmerle, G. Boehm, M.-C. Amann, A. Alù, and M. A. Belkin, "Ultrafast Electrically Tunable Polaritonic Metasurfaces," *Adv. Opt. Mater.*, vol. 2, no. 11, pp. 1057–1063, Nov. 2014.

[173] M. Z. Tidrow, W. A. Beck, W. W. Clark III, H. K. Pollehn, J. W. Little, N. K. Dhar, R. P. Leavitt, S. W. Kennerly, D. W. Beekman, A. C. Goldberg, and W. R. Dyer, "Device physics and focal plane array applications of QWIP and MCT," in *Optoelectronics '99 - Integrated Optoelectronic Devices*, 1999, pp. 100–113.

[174] B. F. Levine, "Quantum-well infrared photodetectors," *J. Appl. Phys.*, vol. 74, no. 8, p. R1, Oct. 1993.

[175] T. R. Schimert, S. L. Barnes, A. J. Brouns, F. C. Case, P. Mitra, and L. T. Claiborne, "Enhanced quantum well infrared photodetector with novel multiple quantum well grating structure," *Appl. Phys. Lett.*, vol. 68, no. 20, p. 2846, May 1996.

[176] J. Lee, B. Zhen, S.-L. Chua, W. Qiu, J. D. Joannopoulos, M. Soljačić, and O. Shapira, "Observation and Differentiation of Unique High-Q Optical Resonances Near Zero Wave Vector in Macroscopic Photonic Crystal Slabs," *Phys. Rev. Lett.*, vol. 109, no. 6, p. 067401, Aug. 2012.